A STUDY OF FUSED DEPOSITION MODELING (FDM) 3-D PRINTING USING MECHANICAL TESTING AND THERMOGRAPHY

A Thesis

Submitted to the Faculty

of

Purdue University

by

Samuel Osekafore Attoye

In Partial Fulfillment of the

Requirements for the Degree

of

Master of Science in Mechanical Engineering

December 2018

Purdue University

Indianapolis, Indiana

THE PURDUE UNIVERSITY GRADUATE SCHOOL
STATEMENT OF COMMITTEE APPROVAL

Dr. Hazim El-Mounayri, Chair

Department of Mechanical and Energy Engineering

Dr. Andres Tovar

Department of Mechanical and Energy Engineering

Dr. Jing Zhang

Department of Mechanical and Energy Engineering

Approved by:

Dr. Sohel Anwar

Chair of the Graduate Program

Dedicated

to my parents Williams and Beatrice Attoye. I pray to always bring them honour.

ACKNOWLEDGMENTS

I would like to express my most sincere gratitude to my research advisor, Dr. Hazim El-Mounayri, for his invaluable guidance and financial support. His training has helped me to grow professionally and personally. I also want to thank the members of my exam committee, Dr. Andres Tovar and Dr. Jing Zhang for their invaluable suggestions to improve this research project. I am sincerely grateful to the mechanical engineering graduate research coordinator Dr. Sohel Anwar and my academic program adviser Mr. Jerry Mooney and also Ms. Summer Layton for their seasoned and insightful suggestions and concern in facilitating my program at the mechanical engineering department. My sincere thanks also to Dr. Peter Orono for his mentorship and the great opportunity to work and learn under his oversight. I am also sincerely grateful to Mr. Patrick Gee for his immense kindness and opportunities to work, learn and involvement with the IUPUI-MEAP. I am deeply grateful to Mr. Michael Golub and my great friend and Brother Mr. Joseph Derrick; their help, kindness and belief in me is not quantifiable. I am sincerely grateful for my great friends Ehsan Malekipour, Homero Valladares-Santiago, Jennifer Solis-Ocampo, Shaunak Chandwadka, Namurata Upadhyaya, Tushar Deshpande and Tanjimul Allam for their great help and critical roles they held during this research work. My sincere thanks also to Ms. Linda Wright and Ms. Deborah Bennet of the mechanical engineering department at IUPUI and Ms. Stephanie Coyle, formerly of the mechanical engineering department at IUPUI and Ms. Terri Talbert-Hatch of the school of engineering and technology at IUPUI for their never ending kindness and constant encouragement. I am very grateful to my friends and colleagues at my research lab; Reza Farahanhi, Sajjad Reisi, Anurag Deb, Avinash Mumbaraddi, Hosein Khazael, Shashank Alai, Suchana Jahan and Prasad Mentha. I am humbled by their graciousness and honoured to have worked and learned alongside them. I want to give heartfelt thanks and sincere appreciation to Dr. and Dr. (Mrs.) Stan and Iyabo Okoro, Mr. Olaolu Laseinde, Mr. Bayode Atandeyi, Mr. Yeajun Yoo and the RCCG Covenant House

Church Indianapolis for all their great kindness, and providing a home for me. Finally, I am deeply grateful for the immense support and encouragement from my wife, OluwaBukola Edasemore, my parents, my brothers (Paul, Daniel and Timothy) and their families.

TABLE OF CONTENTS

Page

LIST OF TABLES

Table Page

LIST OF FIGURES

Figure Page

Figure Page

Figure Page

Figure Page

Figure Page

ABBREVIATIONS

AM: Additive Manufacturing

RP: Rapid Prototyping

CAD: Computer Aided Design

ABSTRACT

Attoye, Samuel Osekafore. M.S.M.E., Purdue University, December 2018. A Study of Fused Deposition Modeling (FDM) 3-D Printing Using Mechanical Testing and Thermography. Major Professor: Hazim El-Mounayri.

Fused deposition modeling (FDM) represents one of the most common techniques for rapid proto-typing in additive manufacturing (AM). This work applies image based thermography to monitor the FDM process in-situ. The nozzle temperature, print speed and print orientation were adjusted during the fabrication process of each specimen. Experimental and numerical analysis were performed on the fabricated specimens. The combination of the layer wise temperature profile plot and temporal plot provide insights for specimens fabricated in x, y and z-axis orientation. For the x-axis orientation build possessing 35 layers, Specimens B16 and B7 printed with nozzle temperature of 225 °C and 235 °C respectively, and at printing speed of 60 mm/s and 100 mm/s respectively with the former possessing the highest modulus, yield strength, and ultimate tensile strength. For the y-axis orientation build possessing 59 layers, Specimens B23, B14 and B8 printed with nozzle temperature of 215 °C, 225 °C and 235 °C respectively, and at printing speed of 80 mm/s, 80 mm/s and 60 mm/s respectively with the former possessing the highest modulus and yield strength, while the latter the highest ultimate tensile strength. For the z-axis orientation build possessing 1256 layers, Specimens B6, B24 and B9 printed with nozzle temperature of 235 °C, 235 °C and 235 °C respectively, and at printing speed of 80 mm/s, 80 mm/s and 60 mm/s respectively with the former possessing the highest modulus and ultimate tensile strength, while B24 had the highest yield strength and B9 the lowest modulus, yield strength and ultimate tensile strength. The results show that the prints oriented in the y-axis orientation perform relatively better than prints in the x-axis and z-axis orientation.

1. INTRODUCTION

1.1 Additive Manufacturing

Additive Manufacturing Several terms including additive fabrication, free form fabrication, direct part manufacturing, layered manufacturing refer to additive manufacturing (AM), [1, 2]. According to ASTM designation, additive manufacturing is the process of joining materials to make objects from 3-D model data, usually layer upon layer, as opposed to subtractive manufacturing technologies [3]. Classification for additive manufacturing technologies is shown in Fig. 1.1 from [4]. These groups; binder jetting, directed energy deposition, material extrusion, material jetting, powder bed fusion, sheet lamination and vat photo-polymerization provide AM technology classes. Additive Manufacturing technologies facilitate the fabrication of parts and devices that are geometrically complex, have graded material compositions, and can be customized for design and manufacturing of cellular structures [5].

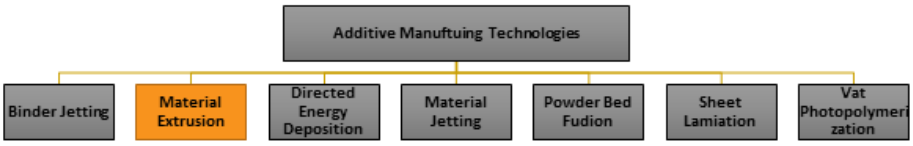

Figure 1.1. Categorization of Additive manufacturing technologies.

Material based extrusion is a prominent method applied in additive manufacturing [4]. The competitive and dynamic nature of the manufacturing market requires a swift concept to design to market process. Additive manufacturing (AM) techniques are capable of meeting this need and achieving zero wastage by reducing material to product ratio [6]. The ease of accomplishing rapid prototyping applications positions AM methodologies as

an integral component of the sustainable manufacturing landscape [7,8]. Rapid prototyping (RP) as a manufacturing concept, refers to a set of manufacturing methodologies applied to swiftly fabricate a functional component and or assembly using derived 2-D profiles from processed computer aided design (CAD) data. The 2-D profiles are built in successive 2-D layers. FDM, is a sub-set technology of additive manufacturing by material extrusion, as an AM technique, FDM is applicable in achieving rapid prototyping. The concept of applying a layer-wise approach in manufacturing is at the core of additive manufacturing. This approach is also applied in developing fuel cells [9].

1.1.1 Fused Deposition Modeling

FDM is an additive manufacturing technique devised and patented by Scott Crump. The industrialized form of FDM is the property of STRATASYS, Inc. FDM technology shown in Fig. 1.2 is essentially G-code controlled vertical material extrusion process. FDM produces parts fit for mechanical, chemical and biochemical operating conditions (end use parts). Fig. 1.2 presents the basic components of the FDM process. Fused deposition modeling process commences with the relevant slicer software. The slicer software performs the function of receiving the 3-D CAD information of the part in the form of a stereolithography (STL) file. Example of slicer software include, Repertoire and, Catalyst.

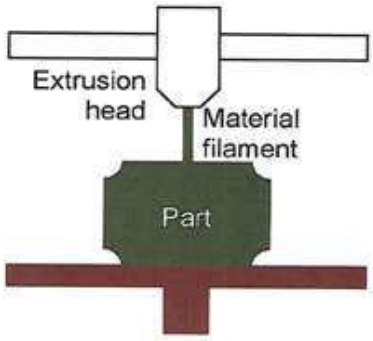

Figure 1.2. Basic components of material extrusion process.

FDM printers are no longer confined to desktop. The build volumes are increased to accommodate larger parts and print at higher deposition rates. In 2014, a Chinese company; Qingdao Unique Products Develop Co Ltd, a local maker of 3-D printers developed a printer with a build volume of 12 x 12 x 12 m for the purpose of building construction. One notable advantage of this new printer is its use of light weight graphene glass fiber reinforced plastic as printing material. The printing material is also strong, corrosion-resistant, and environmentally friendly. Other examples of printers include Builders Extreme 2000 3D with a build volume of 700 x 700 x 1820 mm and featuring an integrated heated bed, two nozzles and color-mixing options. The InnoFil Pro1 filament, which uses reinforced PLA compound thus making it applicable in engineering-grade 3D printing. The Delta Wasp 3MT 3D printer by Italian 3D printing pioneers WASP. Is able to 3D print concrete, clay and plastics a layer resolution 0.5 mm and on a cylindrical build space of 100 x 100 cm. In addition has the capability to act as a CNC mill. The BigDelta 3D printer, released in September 2015, prints clay funneled through a central nozzle. The Discovery extruder; invented in 2017 by Andrew Finkle prints plastic, silicone, clay, wood putty, royal icing, nutella, and chocolate. It was designed to be pre-integrated with Ultimaker printers. The UPrint SE series, with dimension-1200es series, 3D System's Cube, Stratasys' Mojo, MakerBot's Replicator and Fortus-250mc series are also examples of FDM printers. FDM machines have been developed by different manufacturers and the FDM process is performed by the several machine models. However, the basic steps of the process as shown in Fig. 1.3 is unchanged. A critical step in the FDM process is raising the material (polymer) to its glass transition temperature. Extrusion shows more efficiency at temperatures markedly greater than the glass transition temperature of the material. At these levels, the polymer viscosity reduces and its flow is increases.

Figure 1.3. Basic procedure involved in FDM process.

Commonly used materials in FDM are polymeric materials are shown in Fig. 1.4. Polylactic acid (PLA) is a very common desktop printing thermoplastic. Its ability to be pliable when heated and solid when cooled makes it easy to be extruded through the nozzle to build up layers in the FDM process. Although the general tolerances and accuracy of FDM printed materials are mainly dependent on the calibration of the printer and how complex the model is, PLA is useful in creating dimensionally accurate parts with small features and sharp corners. PLA is not as ductile as some other thermoplastics such as ABS so it is widely used for rapid prototyping where form is crucial [10].

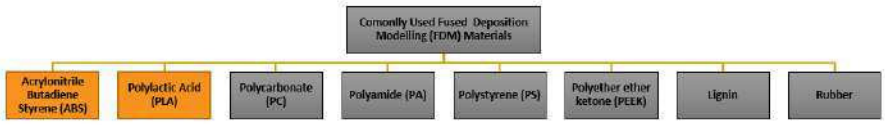

Figure 1.4. Materials commonly used in FDM.

1.2 Image Based Thermography

While current AM machines are greatly improved from early versions, many of the same problems identified by early researchers in the 1980s (porosity, cracking, thermal management issues, material supply issues) persist. This is largely attributable to a lack of in process monitoring and closed loop control algorithms used to manage machine operation [11]. Infra-red imaging is at the core of image based thermography. It has gained acceptance in progress observation of the FDM process. Merits of thermography include, its non-invasive and comparably swift procedure, and its capability in processing and presenting surface temperature distribution during FDM [12].

1.3 Research Rationale and Objectives

FDM is a rapid prototyping (RP) technology, enabling fabrication of three-dimensional parts with complex shapes directly from metal powder (and also non-metal powder) with no or minimal post-processing and integrated parts of a high strength-to-weight ratio [13, 14]. FDM also supports development of functionally graded materials (FGMs). These are

materials with engineered composition, structure and or specific properties aiming to become superior over homogeneous materials composed of same or similar constituents [15]. However, the effectiveness of an RP process is significantly determined by optimizing the part build time, quality, dimensional accuracy, production cost and mechanical properties. According to [16], a major concern in industries with high quality demands (aerospace, biomedical, precision production), is the online quality of the process. The additive manufacturing process integrity has significant impact on the final product quality [11]. In order to establish the technological and economic success of AM in the market, a suitable system for process monitoring is required [17]. Online or inline or real-time or in-situ control enables quality check and on-time intervention of the build process and facilitates swift corrective action [18]. Thus, preventing expensive or impossible part-design adjustments during offline analysis [18]. The ratio of research literature on FDM studies in process investigation, process-parameter effects, process applications, and product characterization to process monitoring is high. Yet, studies by [16] state as critical to industries with high quality demands, is the online quality of the manufacturing process. This research also proposes to facilitate online monitoring of the FDM manufacturing process. The objectives of this research are to;

- Perform real-time monitoring of FDM process of PLA plastic to identify thermal distribution and thermal levels during part evolution
- Interpret the thermal data to determine the effect of the trends observed on process integrity and part quality
- Study effect of printing parameters on mechanical properties of FDM parts

For the purpose of this study PLA thermoplastic is utilized as the raw material.

2. LITERATURE REVIEW

The FDM process is an additive manufacturing technique based on material extrusion. The basic components are presented in Fig. 2.1 from [19]. The operational procedure involves laying plastic filament or metal wire, which has been unwound from a spool in layers along the x-y axis. After every complete layer the extruder head moves upwards (positive z- orientation) for the next layer.

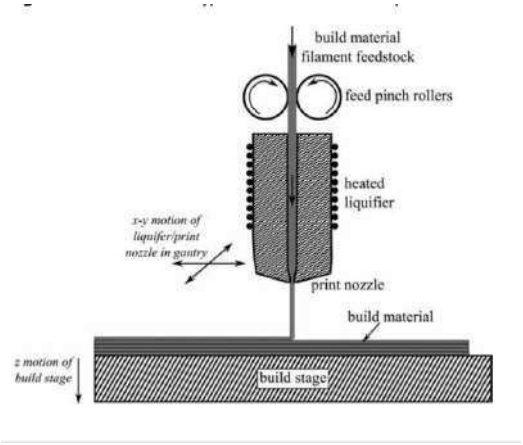

Figure 2.1. Schematic view of the fused deposition modeling process components.

The constructed material is usually made available in filament form as the nozzle has resistive heaters that regulates the plastic at a temperature just over its melting point, causing it to freely flow and subsequently form the layer. There is an instant hardening of the plastic as it bonds to the layer below. As soon as the layer is constructed, the platform lowers and another layer is deposited by the extrusion nozzle. A characteristic feature of FDM printing is the visibility of the printing layers.

FDM represents one of the most common techniques for proto-typing in AM [20]. It is one of the AM technologies that redefined the printing and manufacturing industry. In the printing industry, it broke the limitations of 2D printing enabling individuals to easily bring

their conceptual forms from a 3-dimensional virtual world to life. In the manufacturing industry, the production of goods is no longer restricted to the traditional system of using manual labor and different machinery for different parts. FDM technology however is not free from limitations. Three of these key limitations are the range of materials you can replicate, difficulties in 3D printing finely detailed items, and finished product quality issues. Hence there has always been a constant desire for improvement mostly in these three areas. The expiration of patent rights on the first FDM machine (developed by S. Scott Crump in the late 1980s) paved the way for a large open source development community called RepRap; a self-replicating capable of printing most of its components. Today, there are hundreds of manufactures of FDM printers, some of which produce open-source FDM printers. Most of these manufactures put in a lot of work to meet up with the current demands of the society. Research into FDM can be split into three main categories: novel applications, materials and system improvements [21]. The vast majority of system improvements are software based and are related to tool path generation, slicing algorithms and part orientation optimization. Current research has led to technological advancements of FDM in the manufacturing industry.

2.1 Thermomechanical Aspects of Fused Deposition Modeling

During the extrusion process, the temperature of the material is elevated to its glass transition temperature (this differs from the material melting point). The glass transition temperature refers to the state at which amorphous phase commences. This is distinct from the melting point (where crystalline phase separates and starts to flow). For plastics, temperature is higher than room temperature [22]. Comparing the elastic modulus of plastics to temperature provides more insight on the material glass temperature. Fig. 2.2 from [23] shows the a drop in elastic modulus as temperature increases. The polymer also changes from glassy state to leathery to rubbery then liquid flow as the temperature increases.

FDM fabricated parts also show anisotropic material behavior [24], [25], [26]. This has been observed through the strength analysis effect of print orientation and other spatial

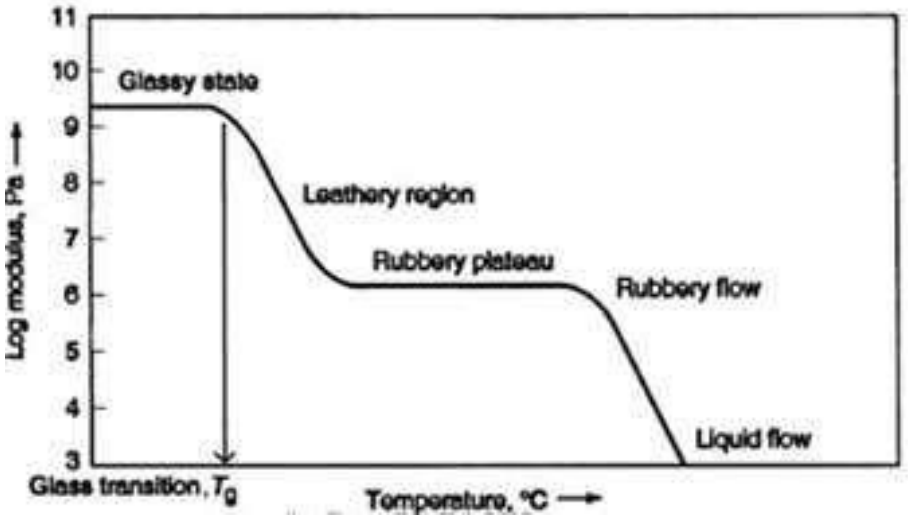

Figure 2.2. Plot showing the influence of temperature on elastic modulus of plastics.

parameters such as raster path on FDM printed parts. The tensile and yield strength results show a significant anisotropic effect [27], [28], [29], [30].

2.1.1 Potential Defects in Fused Deposition Modeling

Defects generally arise from either the print material characteristics (which dependent upon its mechanical and rheological properties) or from the fused deposition processes [31]. Defects can occur in regions of enhanced stress concentration [32], [33], [34]. Resulting in sharp features that amplify mechanical stress adversely affect the ultimate mechanical properties. Surface defects occur as a staircase and slicer conversion effect (which produces polygonal finite elements). Surface defects also occur as support structure burrs, furrowed top surface and start - end errors [35].

The staircase effect is predominantly caused by the slice manufacturing method; it can be corrected by controlling the layer height and processing strategy. The chordal effect on the other hand arises from the stl files which approximate surfaces as a web of triangles and are traditionally used by a lot of RP methods. Although choosing a different surface

modeling format will be effective, a short-term solution will be to offset the part positively and complete with a post-process finishing [36], [37].

A combination of hardware and software restrictions along with material properties can lead to internal defects in polymer and green ceramic parts. The voids in the surrounding areas of the boundaries caused by incomplete filling can result in too little material flow filling up the intersections and thus resulting in a void. This challenge can however be corrected by allocating a negative offset to the perimeter and expanding the flow rate at the points of intersection [31].

Warping and Curling defect presented in Fig. 2.3 from [38] appear as; the printed part curving or bending upwards from the build plate or platform. The build layers cool as deposition occurs; however, earlier deposited layers have already experienced cooling and subsequent contraction.

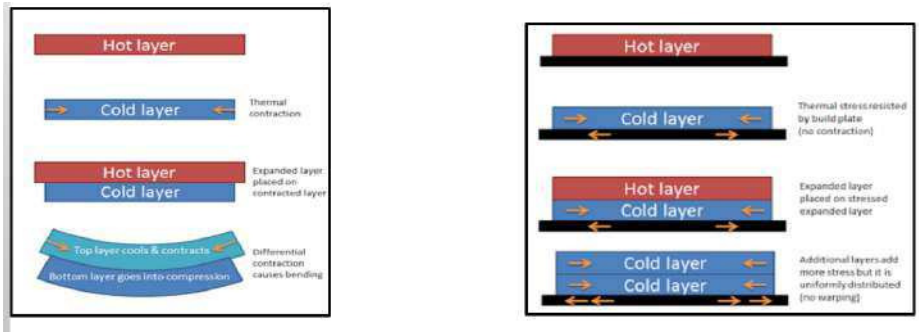

Figure 2.3. Cooling of build layers and part contraction in FDM process.

Thus, the top layer contracts relative to the bottom layer. New layers possess a higher temperature than preceding one, thus creating thermal gradient between the layers and resulting thermal stresses. The cooling and contraction of the part causes warping. Furthermore, when the thermal stresses are greater than bonding between the base layer and the build plate this leads to the part edge curling upwards [39].

To facilitate better printing process, prior to the material deposition the build plate temperature is raised during printing to avoid warping. Also, the build plate temperature is maintained slightly below the point where the material begins to solidify (glass transition

temperature). Thus ensuring that, the base of the build part stays flat and adhered to the build plate [40].

Elephants Foot defect occurs when the first layer of the built is unable to sustain the weight of succeeding layers. The result is the parts base swells outwards [41].

String defect refers to the presence of excess melted material in the extruder nozzle. Resulting in the production of unwanted thin strips of print material. This leads to the print material dripping. Printer manufacturers have integrated retraction capabilities into the printer nozzle to prevent strings

2.2 State of the Art in Fused Deposition Modeling

Shortening build time and improving the surface accuracy especially for complex product models is an important interest in research in RP [4], [42], [43]. The slicing process is also susceptible to the stair-case effect, leading to poor surface quality of end-products [44], [45]. The adaptive tool path generation method is a viable solution to these concerns [46], [47], [48]. Tool path in FDM is the trajectory of the nozzle (print head) during manufacturing process to fill the interior of each layer. There are two main tool path trajectories for FDM processes: contour parallel path and orientation parallel path [49], [50] as shown in Fig. 2.4 from [46].

[46] proposed an approach which covers both surface accuracy and fabrication efficiency. The proposed method consists of three steps. First, an adaptive slicing considering both surface quality and building time is proposed for following tool path generation. Adaptive slicing can alleviate the staircase effect by the alteration of layer thickness according to the geometric characteristic of models.

Secondly, a hybrid tool path strategy was introduced to improve the boundary contours accuracy and reduce the time for interior filling. This step is an adaptive process to choose an appropriate proportional relationship between the two types of tool paths: contour parallel path and direction parallel path according to the specific fabrication requirements.

Abrupt changes in tool path orientation leads to unfilled areas and unstable speed. Tool path adjustment mitigates errors and aids in the improvement of fabrication quality.

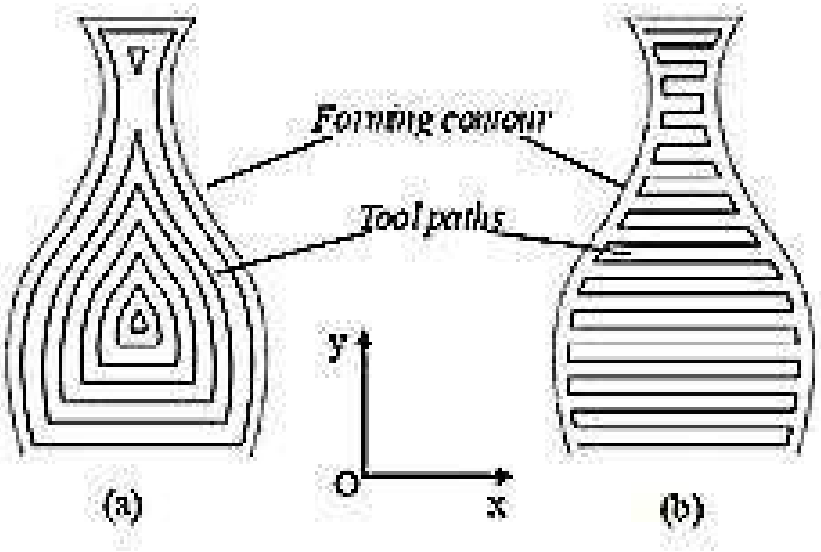

Figure 2.4. Cooling of build layers and part contraction in FDM process.

The tool path adjustment facilitates balance between fabrication quality and building time. This balance was achieved by choosing the speed of nozzle, the number of the contour parallel tool paths and orientation of parallel tool paths. Selection of the parameters is based on the accuracy requirement and the geometrical information of the model [51], [52].

3D Printer farms are an example of improved software based system and are the latest in small manufacturing technology. It is a setup of multiple printers in a cluster to operate with common software for running and monitoring the printers [53]. By utilizing multiple printers set up in an array, products can be produced at higher speeds and brought to market faster. The cost of entry is lower than buying one industrial 3D printer and the array can be scaled up more economically when the need arises. The Stratasys Fortus 380 is an example of an FDM printer farm. It has a maximum print size of 355 x 305 x 305 mm and can print in 7 materials including ABS, ASA, PC and Nylon [54]. According to founder Rene Gurka, founder of BigRep, the real future of 3D printing is in 3D printing farms where multiple large scale models operate in unison and are maintained by a single system [55].

In the advancement of FDM extruder technology, adaptive filament deposition (AFD) and planar layer deposition (PLD) were developed as material deposition techniques for the freeform fabrication of metals and ceramics [56], [57]. AFD utilizes a conical spindle inside a deposition head to vary the volumetric flow rate of liquids through the extrusion orifice. After leaving the orifice the liquid jet is cooled by the ambient air temperature and becomes a filament. Retracting the spindle away from the orifice allows higher flow rates which in turn increases the filament size.

Various polymeric materials have been explored for application in FDM, however commercial FDM machines mostly use acrylonitrile butadiene styrene (ABS) and polylactic acid (PLA) [20]. That is because most commercial FDM extruders have 300C limit, while enabling rapid solidification. This is to ensure that the printed layers do not lose shape.

While there are different types of materials that can be used in AM, the material properties are typically not as strong as their conventionally manufactured counterparts due to the anisotropy caused by the layer-by-layer [58]. Recent research has shown the viability of composite materials such as metal matrix composites, ceramic composites, natural fibre-reinforced composites and polymer matrix composites [59]. Researchers at Rutgers University in the United States have developed fused deposition of ceramics (FDC) [10].

Currently, the most common FDM filaments are PLA, ABS and Nylon for printing parts while PVA and HIPS are the most common support filaments due to their dissolvability. New filaments that use TPE or TPU (Thermoplastic polyurethane) print parts with much higher elasticity than ABS and PLA. Composite filaments include carbon fiber, metal powder or wood fibers with PLA, Nylon or ABS. Among the most common three filaments, Nylon has the highest strength and flexibility, followed by PLA that has a medium strength and least flexibility. Finally, ABS has the lowest strength accompanied with higher flexibility than PLA. ABS has the advantage of being dissolvable in acetone which gives the ability to chemically treat its surface for better finishing [60].

2.3 Research in Monitoring Fused Deposition Modeling Process

Process monitoring of additive manufacturing refers to the observation of the internal workings of the 3D printer during the fusion process stage. Process monitoring also encompasses the observation of the printing process parameters [61]. An understanding of what takes place during this stage will lead to the development of a quality control system which would aid in industrial additive manufacturing [11]. In addition, seamlessly controllable approaches in process calibration and oversight ensures part verification and validation on an industrial scale. This is critical in the biomedical, aerospace and defense industries [62], also would improve manufacturing time and enhance mass production of customized parts.

In their study, [63] used ultrasonic excitation as a means of detecting filament bonding failures introduced by manipulating the print bed temperature during the fused deposition modeling build process. The work demonstrated the capability of correcting these filament bonding failures using a correction mechanism introduced through tunable control of another process parameter of the printer. By demonstrating the detection and correction of filament bonding failures in situ, the results showed a progress towards a fully closed loop control for fused deposition modeling processes.

Nozzle clogging in FDM printer extruders leads to process errors and subsequent print failure [64]. Current FDM machines have limited techniques to monitor process conditions to minimize process errors such as nozzle clogging, [65] presented a physics-based dynamic model suitable for monitoring nozzle clogging in FDM. The approach involved simulation of nozzle clogging using nozzles of diameters from 0.5 to 0.2 mm with change intervals of 0.1 mm. Sets of experiments were carried out by measuring vibration of the liquefier block mount during material extrusion. The results showed that liquefier block mount transverse vibration amplitude increases non-linearly at nozzle blockage onset. Thus, providing proven reasons for integrating sensors to monitor the onset of nozzle clogging as a viable solution.

Although research has been done and is on-gong to improve current AM products, issues like porosity, cracking, thermal management issues, and material supply issues persist. This is attributable to the inadequacy of integrated systems to study the on-going

fabrication, and closed loop control algorithms for machine operation oversight [11]. Due to the aforementioned dearth, manufacturers adjust process parameters based on heuristics and previous fabrication runs, yielding limited improvement in part quality and requiring many build runs for convergence. While some process monitoring methods can generally be incorporated to all techniques of additive manufacturing, some are specifically designed to a particular 3D printing type and can be adapted to them only.

The typical machine condition monitoring sequence includes fabrication parameter choice protocols, perception and data retrieval, data conversion handling and attribute elicitation, intellective judgment and response [66]. Machine condition monitoring strategies are commonly based on two types of models, physics-based models and data-driven (empirical) models. Physics-based models predict the phenomena of systems with the consideration of physical natures and mechanisms of the systems. Data-driven models utilize historical data only to build analytical models for product property or failure predictions [67], [68], [69], [70].

In a study on process monitoring, [66] employed acoustic emission (AE) technique for in-situ monitoring of FDM machine conditions. The approach diagnosed and established machine normal and abnormal states. Machine condition normal states were determined as, material loading, normal extruding, and idle. Machine condition abnormal states were classified to include; print material run-out, extruder semi-blocked with chatter and uneven extrusion due to breakdown of heater, low-quality filament, extruder wear, or working environment contamination, as well as total blockage without extrusion. The time-domain features of AE hits were used as the indicators. AE approach overview is presented in Fig. 2.5 showing the FDM printer states monitored during the fabrication process.

Temperature fluctuations, distribution and the influence of fabrication process thermal loads developed during the building process also affect the FDM product quality [71], [72], [73], [74]. Also [75] carried out numerical study on temperature distribution during the FDM process. The approach utilized real time and in-situ monitoring during the fabrication of multilayered thin plates by embedded thermal sensors.

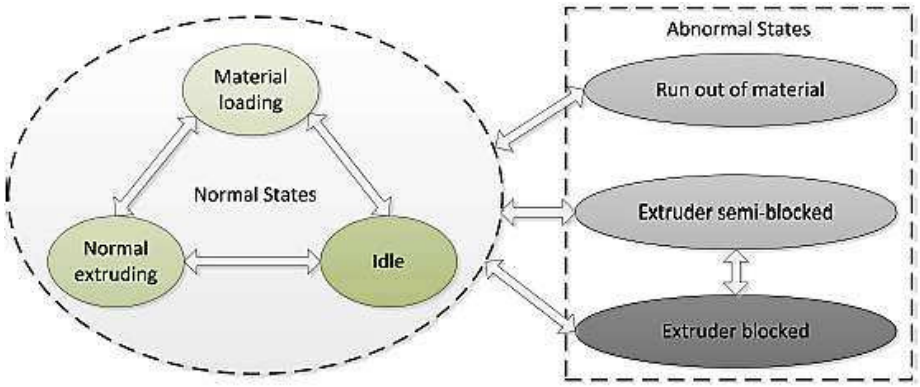

Figure 2.5. Machine conditions during FDM fabrication process.

2.4 Thermography Applications in Additive Manufacturing

All matter with a temperature above absolute zero radiates electromagnetic energy due to atomic excitation [76]. An object, when heated, radiates electromagnetic energy in form of waves over a range of wavelengths. The amount of energy radiated by an objects depends on its absolute temperature, its emissivity, and is a function of wavelength [77]. Temperature sensors are able to retrieve this electromagnetic energy and correlate the identified radiation intensity with the temperature of the object. Thermal scanners measure thermal data in IR region of the electromagnetic spectrum [78]. Most commonly used intervals are the intervals 3 µm - 5 µm (Mid-infrared) and 8 µm - 14 µm (thermal infrared) as shown in Fig. 2.6 from [41].

In a thermal image, the pixels Fig. 2.7 (left) from [79] are acquired by sensor detectors and arranged in a focal plane array (FPA). The individual pixel is repository electromagnetic radiation. Thus facilitating collection of radiation emitted from a two-dimensional space. When the intensity of the radiation is converted into a two-dimensional map of temperature, a thermogram results Fig. 2.7 (right) from [79]. IR thermography is the use of thermograms, resulting from the collection of radiation in the IR part of the spectrum, to study the temperature distribution in an object [77].

Infrared thermography procedure as shown in Fig. 2.8 from [79] has been employed in AM process monitoring research. Most of these studies are based on Selective Layer

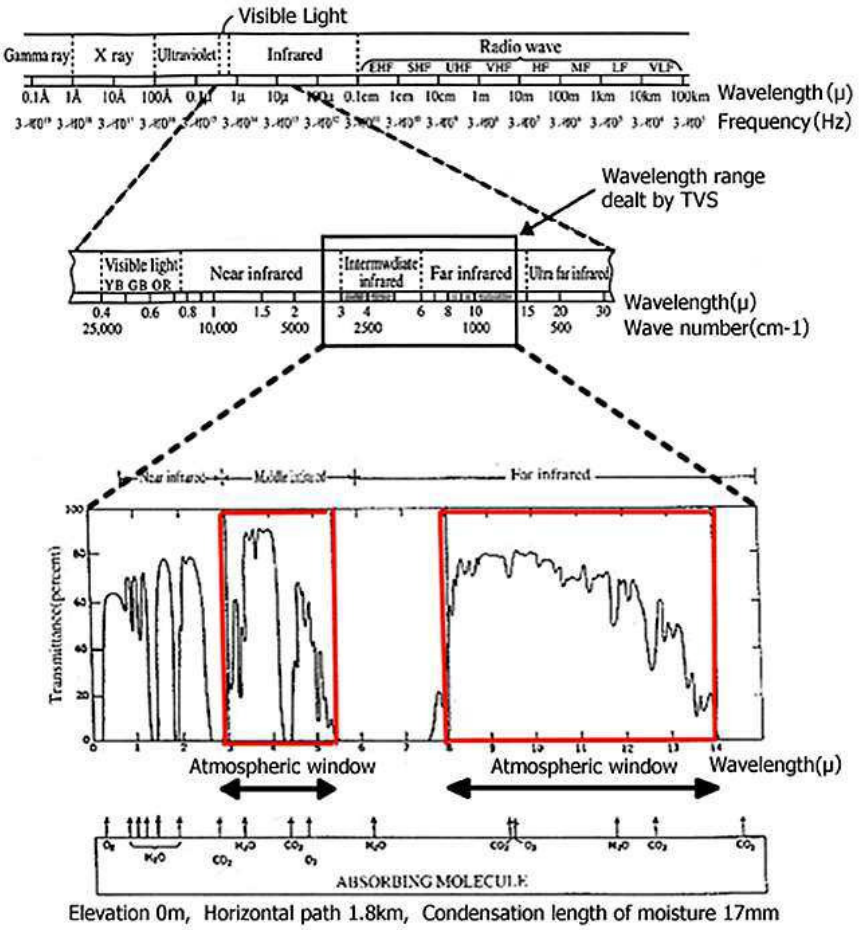

Figure 2.6. Infrared wavelength region in the electromagnetic spectrum.

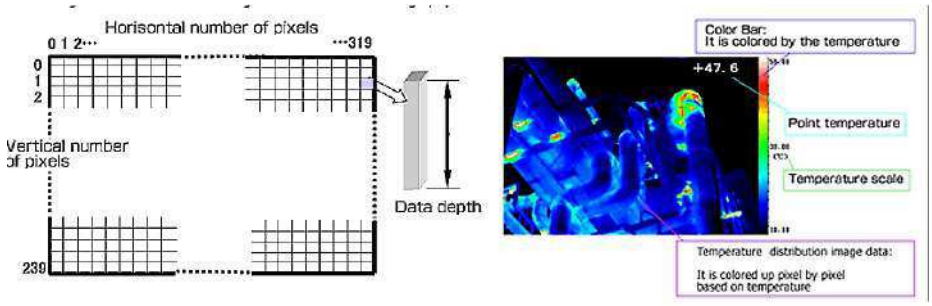

Figure 2.7. Arrangement of detector and image data of infrared thermography (left) and temperature distribution infrared image data (right).

Melting (SLM) (metal based AM). This could be attributed to SLM core characteristic as a thermal process [80], [81], [2].

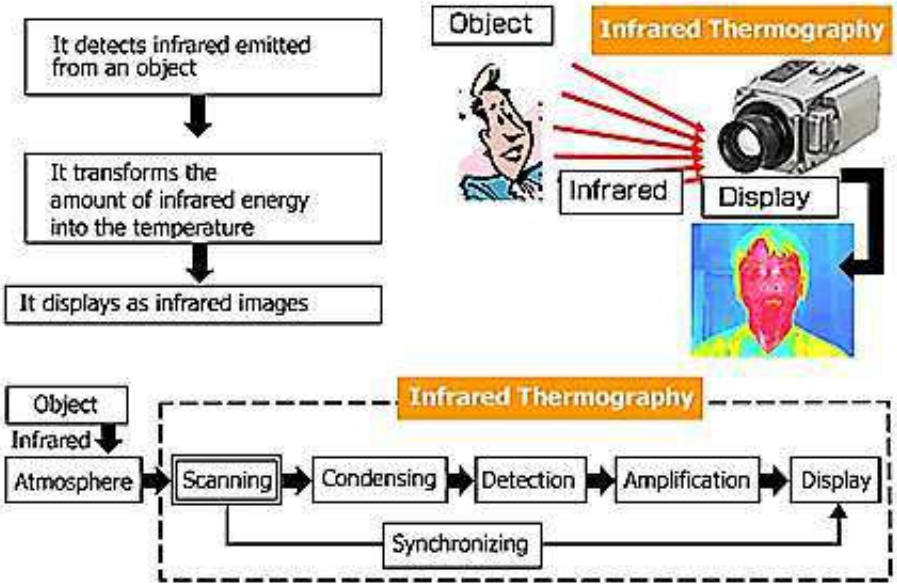

Figure 2.8. Measurement principle and work-flow process for data retrieval by thermography.

For example, [2] applied true temperature measurements for the purpose of validating high-fidelity multiphysics models of the PBF processes. Their approach involved augmenting the orthodox IR camera imaging with hyperspectral imaging. Where a traditional IR camera integrates over a range of wavelengths, the hyperspectral camera function simultaneously captures individual images at multiple discreet wavelengths permitting individual pixel to be analyzed. The plots of intensity versus wavelength were also developed.

The FDM process is also inherently a thermal process and thus lends itself to study using IR cameras. Temperatures within the oven, temperature mapping of parts during deposition, and extrusion temperatures as a function of tip design are critical to the 3D printing process [82].

In their study, [12] developed an experimental model to facilitate optimized cost infrared thermography imaging method. Acquiring thermal data of filaments at the interface and

their corresponding cooling mechanism was performed. A three-dimensional finite element model was established for process simulation using element "birth and death" feature. Validation of the developed model was performed using the experimental model thermal response. [82] used a two-step approach to perform thermal imaging of an FDM production system using an extended-range IR camera. The objective was to quantify the temperature variation of the parts in-situ. The IR camera was also used to map the temperature within the build volume.

In the first approach an extended range IR camera equipped with a low pass cutoff filter is used to image directly through a double pane soda lime glass window. This allowed a view of the entire build volume and measurements of the temperature uniformity of the oven, as well as, individual parts as they are being printed. In the second approach, a small lightweight uncooled longwave IR camera was mounted on the liquefier head and focused onto a close-up view of the heated extrusion tip. This view allowed higher resolution imaging and temperature measurements of the thermoplastic as they were extruded and began to cool on contact with the layer of material below.

According to [83], thermographic imaging presents a viable method for in-situ monitoring for AM manufacturing. However, challenges due to the difference in surface emittance between the print powder and solidified part being observed adversely impacts temperature data accuracy.

To further enhance thermal based process monitoring, [83] developed a method for calibrating temperature profiles from thermographic data. to account for this emittance change, and to determine important characteristics of the build through additional processing. The results show that by using a simple post-processing analysis of the IR intensity data, one can create a relatively accurate representation of the layer-wise temperature profile within an AM build.

3. METHODOLOGY

3.1 Materials and Methodology

The approach adopted in this study is shown in Fig. 3.1. Firstly a suitable design for the test specimen is selected. This is followed by minor adjustments in the specimen dimensions in the scale, to deal with the build volume constraints presented by the available equipment.

Figure 3.1. Methodology process flow.

The specimen selected for monitoring and evaluation is shown in Fig. 3.2. the specimen was based on the ASTM tensile strength test standard part. Although the dimensions were adjusted to facilitate the printing process.

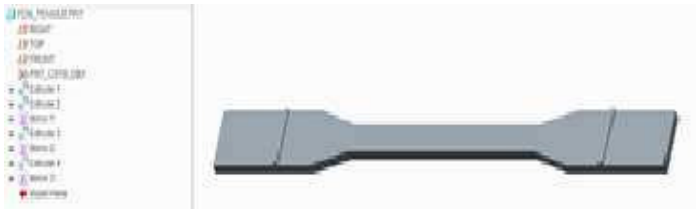

Figure 3.2. Specimen designed for monitoring and evaluation.

The design process was followed by the fabrication process. Two (2) sets of the specimen were fabricated. Set-A consisted of thirty-six (36) individual printed specimens (specimen A1 to A36). Set A was taken as an initial run. This was due to the on-line monitoring not achieving usable thermal information of the part build layers. The printing process parameters (nozzle temperature, printing speed and print orientation) were adjusted for

Table 3.1.
Printing parameters adjusted for fabrication process of set-A consisting of specimens A1 to A36

Printing parameter			
Nozzle temperature ℃	220	215	200
Printing speed mm/s	60	40	20

each part. A Makerbot Replicator 5th Gen. FDM 3-D printer shown in Fig. 3.3 was used to fabricate the Set-A specimens.

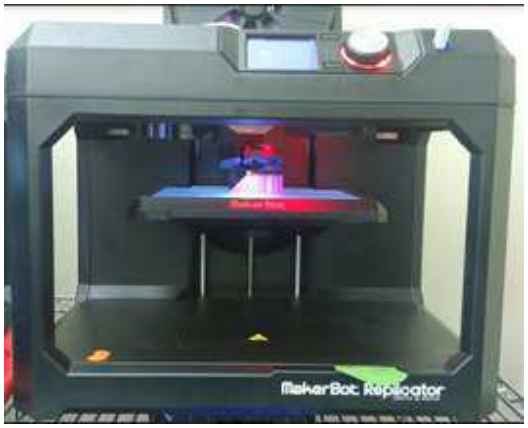

Figure 3.3. Makerbot Replicator 5th gen. FDM 3-D printer.

The printing parameter values used during the fabrication process are given in Table3.1. They were selected based on the recommendations of the machine and material specifications. For set-A the material used was the MakerBot PLA.

The build orientation was adjusted in the x, y, z and 45 degree orientations as shown in Fig. 3.4 .

The list of the fabricated specimens and the printing parameters adjusted during printing are given in Tables 3.2, 3.3, 3.4 and 3.5

Set-B consisted of twenty-seven (27) individual printed specimens. For set-B thermal information of the part build layers was acquired. The printing process parameters (nozzle

Table 3.2.
List of specimens A1 to A9 and parameters used in printing on the MakerBot 5th Gen FDM 3-D printer

Specimen number	Nozzle temperature °C	Print speed mm/s	Print orientation
A1	220	60	x-axis
A2	220	60	y-axis
A3	220	60	z-axis
A4	220	40	x-axis
A5	220	40	y-axis
A6	220	40	z-axis
A7	220	20	x-axis
A8	220	20	y-axis
A9	220	20	z-axis

Table 3.3.
List of specimen A10 to A18 and parameters used in printing on the MakerBot 5th Gen FDM 3-D printer

Specimen number	Nozzle temperature °C	Print speed mm/s	Print orientation
A10	215	60	x-axis
A11	215	60	y-axis
A12	215	60	z-axis
A13	215	40	x-axis
A14	215	40	y-axis
A15	215	40	z-axis
A16	215	20	x-axis
A17	215	20	y-axis
A18	215	20	z-axis

Table 3.4.
List of specimen A19 to A27 and parameters used in printing on the MakerBot 5th Gen FDM 3-D printer

Specimen number	Nozzle temperature °C	Print speed mm/s	Print orientation
A19	200	60	x-axis
A20	200	60	y-axis
A21	200	60	z-axis
A22	200	40	x-axis
A23	200	40	y-axis
A24	200	40	z-axis
A25	200	20	x-axis
A26	200	20	y-axis
A27	200	20	z-axis

Table 3.5.
List of specimen A28 to A36 and parameters used in printing on the MakerBot 5th Gen FDM 3-D printer

Specimen number	Nozzle temperature °C	Print speed mm/s	Print orientation
A28	220	60	45°
A29	220	40	45°
A30	220	20	45°
A31	215	60	45°
A32	215	40	45°
A33	215	20	45°
A34	200	60	45°
A35	200	40	45°
A36	200	20	45°

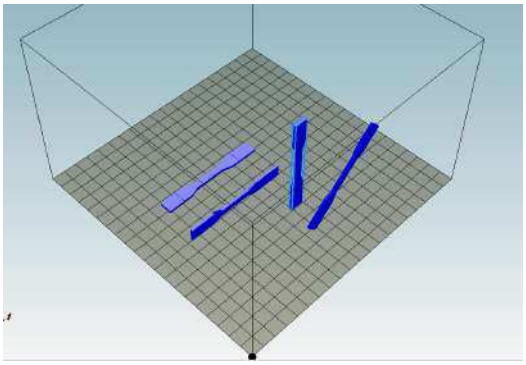

Figure 3.4. x, y, z and 45 degree build orientation used in fabricating specimen set-A .

temperature, printing speed and print orientation) were adjusted for each part. An Air-Wolf Fig. 3.5 FDM 3-D printer was used to fabricate set-B specimens.

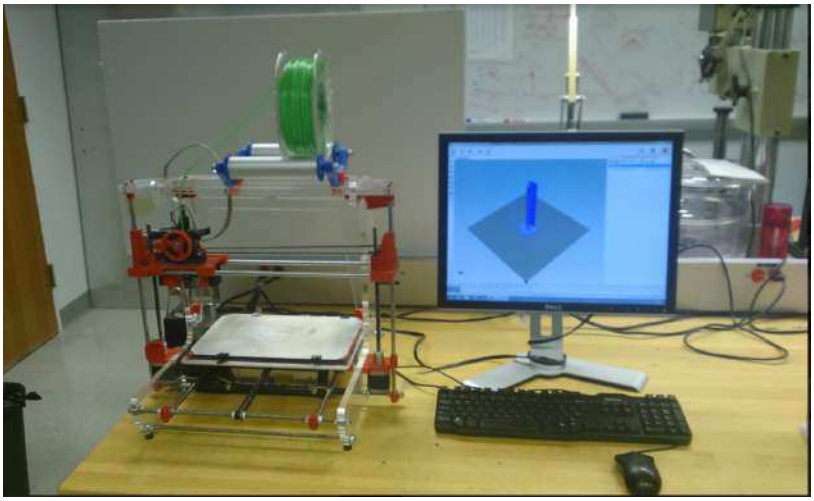

Figure 3.5. Air-Wolf FDM 3-D printer.

The printing parameter values for set-B presented in Table 3.6 were selected based on the recommendations of the machine and material specifications. For set-B the material used was ABS.

The list of the fabricated specimens and the printing parameters adjusted during printing are given in Tables 3.7, 3.8 and 3.9.

The build orientation was adjusted in the x, y and z orientations as shown in Fig. 3.6

Table 3.6.
Parameters adjusted for fabrication process of set-B specimen B1 to B27

Printing parameter			
Nozzle temperature ℃	235	225	215
Printing speed mm/s	100	80	60

Table 3.7.
List of specimen B1 to B9 and parameters used in printing on the AirWolf FDM 3-D printer

Specimen number	Nozzle temperature ℃	Print speed mm/s	Print orientation
B1	235	100	x-axis
B2	235	100	y-axis
B3	235	100	z-axis
B4	235	80	x-axis
B5	235	80	y-axis
B6	235	80	z-axis
B7	235	60	x-axis
B8	235	60	y-axis
B9	235	60	z-axis

To facilitate acquiring the manufacturing process thermal information. A FLIR IR camera A325 series shown on the left in Fig. 3.7 interfaced with the Research IR Max software student test version shown on the right in Fig. 3.7 was used for monitoring the process.

The fabricated specimens are evaluated and the results were analyzed. In-situ monitoring of specimen B1-27 shown on the left of Fig. 3.8 was successful. Fig. 3.8 shows the equipment set-up for monitoring and retrieving the FDM process thermal data.

Mechanical analysis of set-A and set-B was performed using Q-test machine, extensometer and test-works software.

Table 3.8.
List of specimen B10 to B18 and parameters used in printing on the AirWolf FDM 3-D printer

Specimen number	Nozzle temperature °C	Print speed mm/s	Print orientation
B10	225	100	x-axis
B11	225	100	y-axis
B12	225	100	z-axis
B13	225	80	x-axis
B14	225	80	y-axis
B15	225	80	z-axis
B16	225	60	x-axis
B17	225	60	y-axis
B18	225	60	z-axis

Table 3.9.
List of specimen B19 to B27 and parameters used in printing on the AirWolf 5th Gen FDM 3-D printer

Specimen number	Nozzle temperature °C	Print speed mm/s	Print orientation
B19	215	100	x-axis
B20	215	100	y-axis
B21	215	100	z-axis
B22	215	80	x-axis
B23	215	80	y-axis
B24	215	80	z-axis
B25	215	60	x-axis
B26	215	60	y-axis
B27	215	60	z-axis

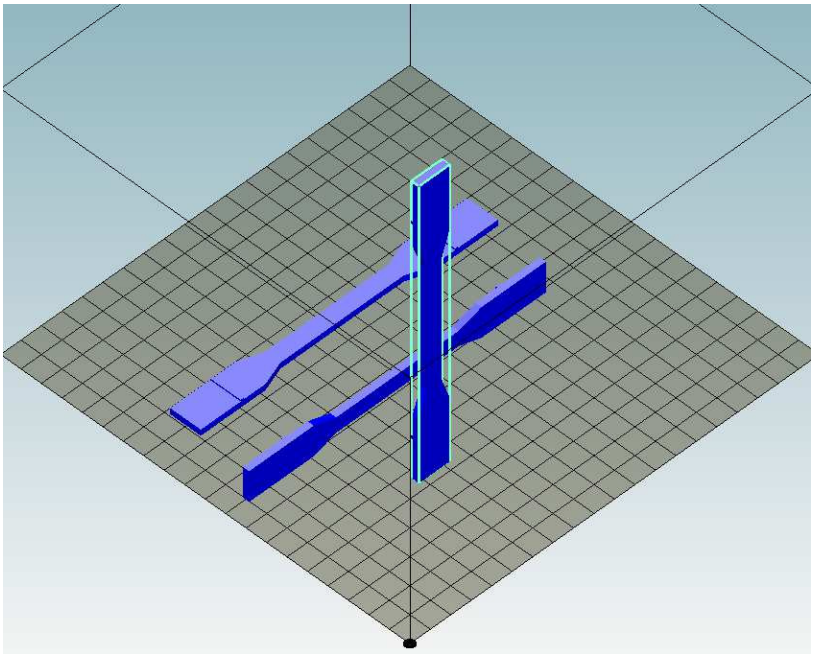

Figure 3.6. x, y and z axis build orientation used in fabricating specimen set-B.

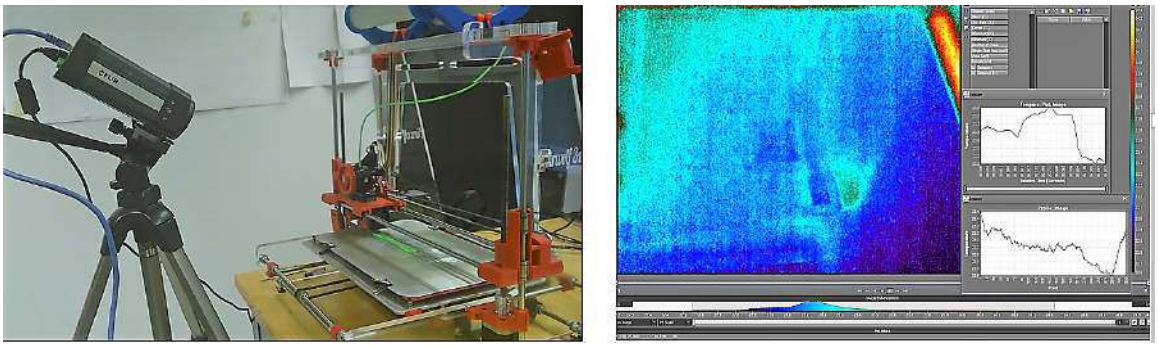

Figure 3.7. FLIR IR camera A325 (left) and Research IR Max software interface (right).

3.2 Experimental Set-up for Mechanical Testing of Fabricated Specimens

The objective of the experimental analysis performed wads to determine the stress-strain relationship of the FDM printed specimens. This was accomplished by performing tensile strength test on the fifty-four (54) specimens. A combination of a Q-Test machine shown on the left of Fig. 3.9 and Matt Struve Demo MTS Extensometer shown on the right of Fig. 3.9 interfaced with the Test-Works software platform. Was used for the mechanical test.

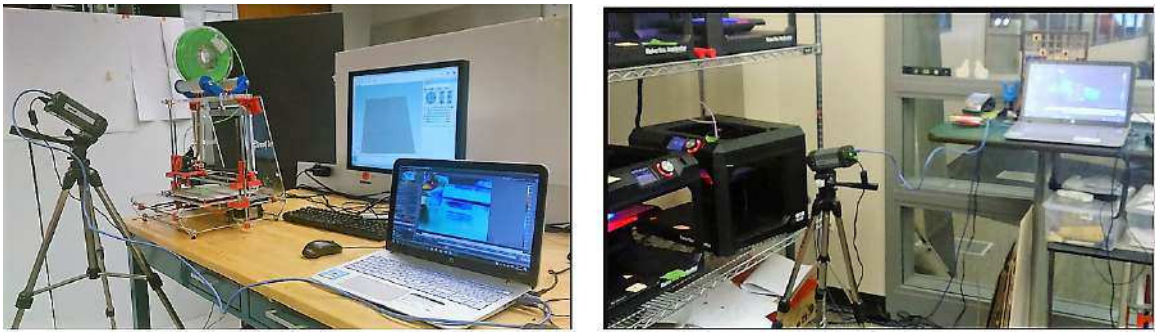

Figure 3.8. Monitoring the FDM process on the Air-Wolf 3-D printer (left) and Monitoring the FDM process on the MakerBot 3-D printer (right) .

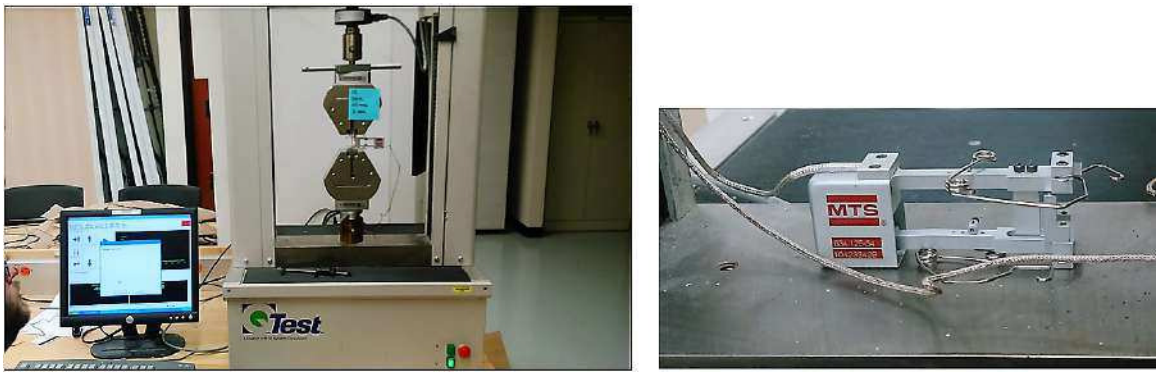

Figure 3.9. Q-Test machine (left) and Matt Struve Demo MTS Extensometer (right).

To determine the stress-strain relationship of each specimen, the following steps were followed; The width and thickness and, the length of the segment with a reduced cross sectional area was measured. Each specimen was installed separately into the steel jaws of the Q-test machine and the extensometer was attached at the mid-length as shown in Fig. 3.10.

The Test-Works software was activated and run. To begin the software analysis each specimens thickness and width are supplied through the user interface. The test runs until the system senses a set limit on load, extension, strain or a significant decrease in load indicating specimen fracture. The effect of printing parameters adjusted during fabrication (nozzle temperature, printing speed and print orientation) on the part build process was observed. The interaction between the printing parameters and their effect on

Figure 3.10. Installation of specimen into Q-test machine and extensometer attached to the specimen for mechanical testing.

the mechanical properties (tensile strength, yield strength, Youngs modulus and ultimate tensile strength) were determined.

4. RESULTS AND DISCUSSION

The results from in-situ monitoring of the FDM process are presented in this chapter. The effect of adjusting the printing parameters (nozzle temperature, printing speed and print orientation) during the fabrication on the part build process are also presented in this chapter. The interaction between the printing parameters and their effect on the part thermal evolution and mechanical properties (tensile strength, yield strength, Youngs modulus and ultimate tensile strength) are determined.

4.1 Results from Mechanical Testing of the Specimens Fabricated on the MakerBot 5th Gen 3-D Printer

During the printing process, it was observed that the specimens fabricated in the x-axis orientation took the shortest time to print. This was due to the fewer layers required to complete the part build in this orientation. The specimens printed in the 45 degree axis orientation took considerably longer to print. This was due to the requirement of support structure. The MakerBot 5th Gen 3-D printer showed no observable difficulty in building the specimens. Although thermal data from the printing process on MakerBot 5th Gen 3-D printer was not achieved, the process provided a means for preparing in-situ monitoring on the AirWolf 3-D printer.

Fig. 4.1 and 4.2 present the specimens prior to tensile strength evaluation on the Q-test machine. These specimens were printed using different orientation axes (x, y, z and 45 degrees). Fig. 4.1 presents the specimens prior to tensile strength evaluation on the Q-test machine. These specimens were printed in the x, y and z- axis orientation.

The effect of the print speed on the build time was negligible. However the mechanical analysis show more discernible influence of the print speed parameter on the build process and final product mechanical properties. Support structures were implemented to accom-

Figure 4.1. Specimen A1 to A27 prior to evaluation on the Q-test machine.

plish the part build in the 45 degree axis orientation. Fig. 4.2 presents the specimens prior to tensile strength evaluation on the Q-test machine. These specimens were printed the 45 degree axis orientation.

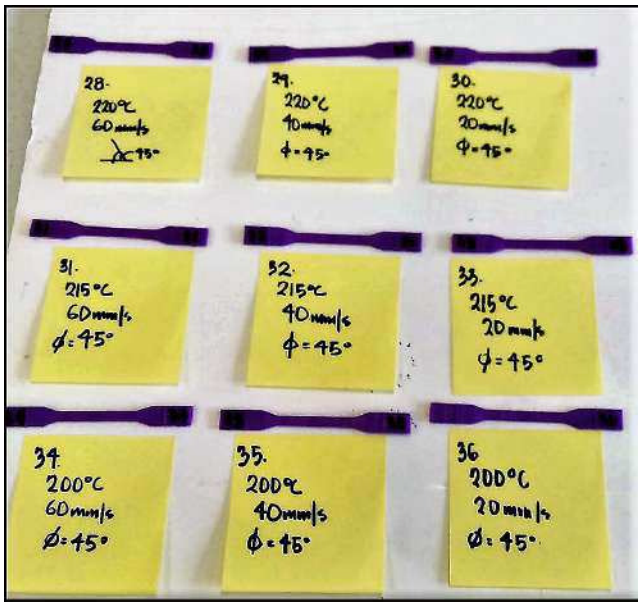

Figure 4.2. Specimen A28 to A36 prior to evaluation on the Q-test machine.

Fig. 4.3 - 4.8 show that, the specimens printed in the x-axis orientation (A1, A4, A7, A10, A13, A16, A19, A22 and A25) tended to fracture at location close to the end at the neck region. The specimens printed in the y-axis orientation (A2, A5, A8, A11, A14, A17, A20, A23 and A26) tended also to fracture at location close to the end at the neck region.

However, the specimens printed in the z-orientation (A3, A6, A9, A12, A15, A18, A21, A24 and A27) tended to fracture at location closer to the mid region of the specimen. Fig. 4.3 - 4.8 also show the specimens after tensile strength evaluation on the Q test machine.

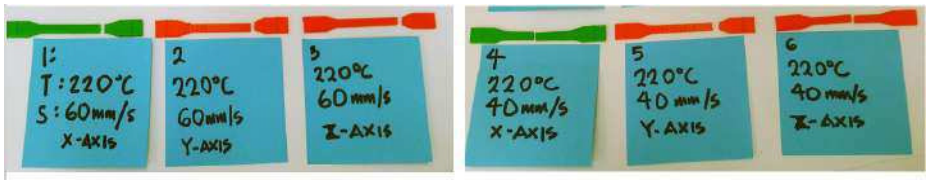

Figure 4.3. Specimen A1 to A6 after evaluation on the Q test machine.

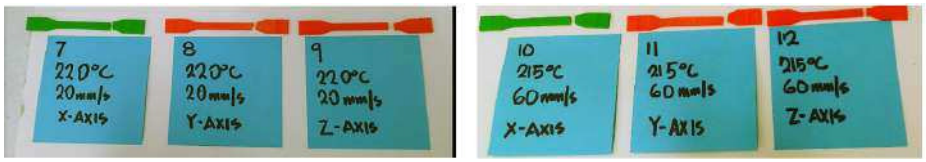

Figure 4.4. Specimen A7 to A12 after evaluation on the Q test machine.

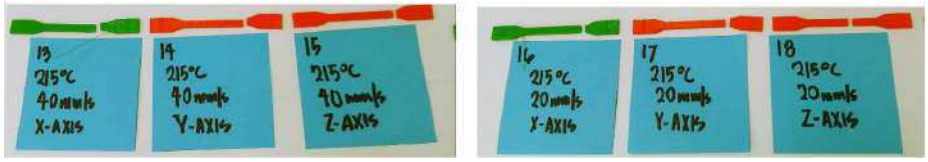

Figure 4.5. Specimen A13 to A18 after evaluation on the Q test machine.

Figure 4.6. Specimen A19 to A24 after evaluation on the Q test machine.

For specimens A1 to A36, printed on the MakerBot 5th Gen 3-D Printer along the x, y, z and 45 degree axes orientation the stress-strain curves show the effect of the changing

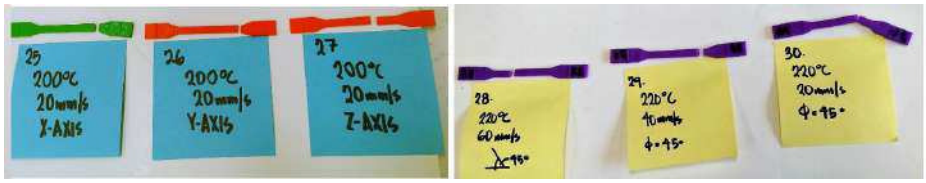

Figure 4.7. Specimen A25 to A30 after evaluation on the Q test machine.

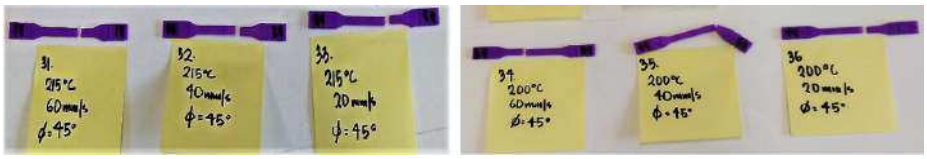

Figure 4.8. Specimen A31 to A36 after evaluation on the Q test machine.

the printing parameters on the mechanical behavior of each specimen. Values of the modulus, yield strength and ultimate tensile strength of the specimens gotten from the tensile strength analysis are presented in Tables 4.1 - 4.4. While, Fig. 4.9 - 4.24 present the plots of the stress- strain curves for the specimens according to the print orientation axis.

The plots for specimen A1, 4 and 7 shown in Fig. 4.9 suggest that holding the nozzle temperature constant at 220 °C and reducing the printing speed, from 60mm/s to 40mm/s to 20mm/s would initially increase, then subsequently decrease the specimen modulus. This would also initially increase, then subsequently decrease the specimen yield strength. However the ultimate tensile strength continues increasing.

The plots for specimen A10, 13 and 16 shown in Fig. 4.10 suggest that holding the nozzle temperature constant at 215 °C and reducing the printing speed, from 60mm/s to 40mm/s to 20mm/s would decrease the specimen modulus. This would also decrease the specimen yield strength. However, the ultimate tensile strength initially increases, then subsequently decreases.

The plots for specimen A19, 22 and 25 shown in Fig. 4.11 suggest that holding the nozzle temperature constant at 200 °C and reducing the printing speed, from 60mm/s to 40mm/s to 20mm/s would decrease the specimen modulus. This would also decrease

Table 4.1.
Mechanical properties of specimens printed in the x-axis orientation on the MakerBot 5th Gen. 3-D Printer

Specimen number	Modulus (ksi)	Yield strength (ksi)	Ultimate tensile strength (ksi)
A1	157.9225	0.33208	4.652
A4	175.4068	0.3684	5.851
A7	168.0255	0.35298	6
A10	182.0886	0.36648	6.339
A13	167.8267	0.335	6.443
A16	164.2413	0.32895	6.426
A19	185.764	0.37276	6.421
A22	168.9967	0.35316	6.516
A25	158.4194	0.31537	6.179

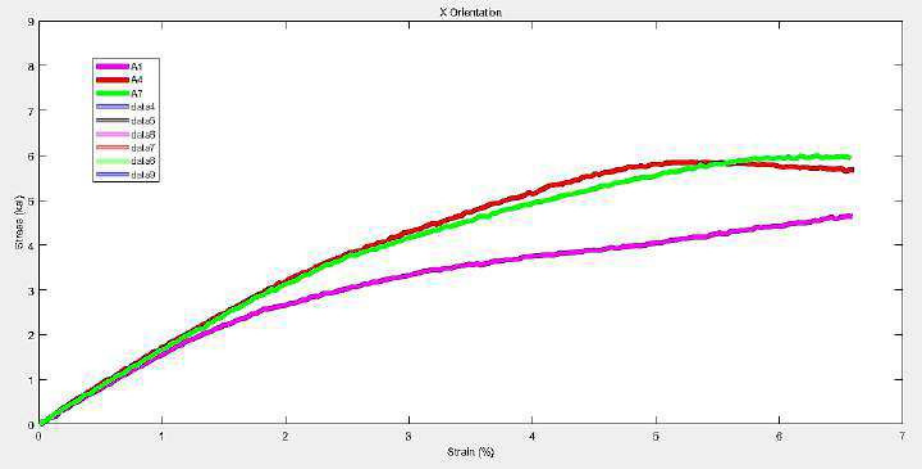

Figure 4.9. Plot of stress-strain curve for specimens A1, 4 and 7, printed in the x-axis orientation on the MakerBot 5th Gen. 3-D Printer.

the specimen the yield strength. However, the ultimate tensile strength initially increases, then subsequently decreases.

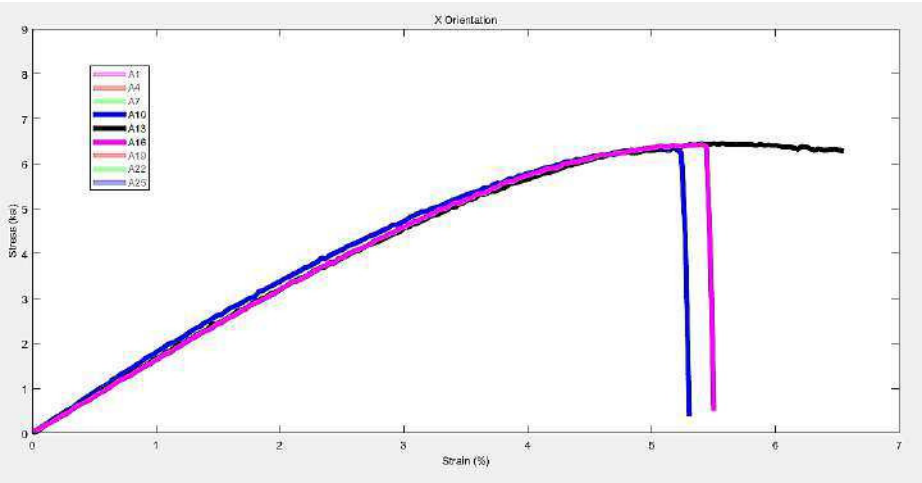

Figure 4.10. Plot of stress-strain curve for specimens A10, 13 and 16, printed in the x-axis orientation on the MakerBot 5th Gen. 3-D Printer.

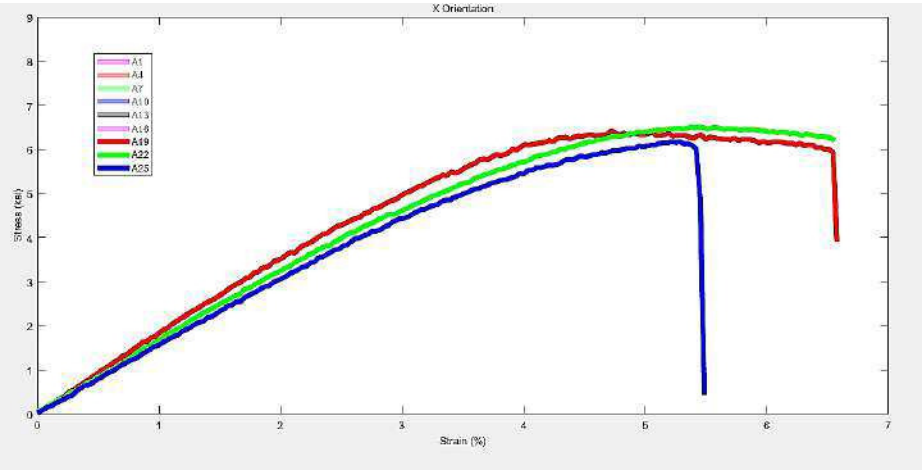

Figure 4.11. Plot of stress-strain curve for specimens A19, 22 and 25, printed in the x-axis orientation on the MakerBot 5th Gen. 3-D Printer.

For the specimens printed in the x-axis orientation Table 4.1, specimen A19; printed with nozzle temperature of 200 °C and printing speed of 60 mm/s possesses the highest yield strength, and modulus however, specimen A22 (printed with nozzle temperature of 200 °C and at printing speed of 40 mm/s) is seen to possess the highest ultimate tensile strength. Specimen A1 (printed with nozzle temperature of 220 °C and at printing speed of 60 mm/s), possess the lowest modulus, while specimen A25 (printed with nozzle temperature

of 200 °C and at printing speed of 20 mm/s) possesses the lowest yield strength. Fig. 4.12 presents the stress strain curve of the specimens printed in the xaxis orientation.

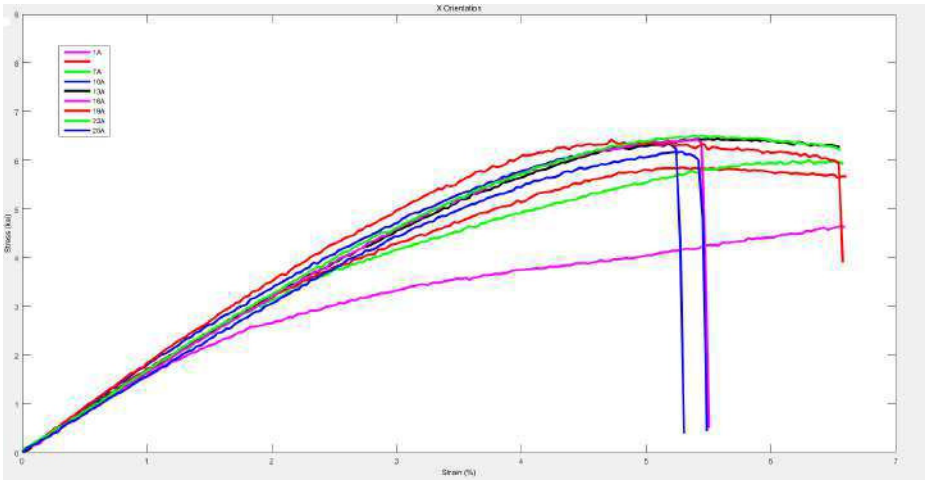

Figure 4.12. Plot of stress-strain curve for all specimens printed in the x-axis orientation on the MakerBot 5th Gen. 3-D Printer.

Values of the modulus, yield strength and ultimate tensile strength of the specimens gotten from the tensile strength analysis of the specimens printed in the y-axis orientation are presented in Table 4.2.

The plots for specimen A2, 5 and 8 shown in Fig. 4.13, suggest that holding the nozzle temperature constant at 220 °C and reducing the printing speed, from 60mm/s to 40mm/s to 20mm/s would decrease the specimen modulus. This would however initially increase the specimen yield strength then subsequently decrease it. The ultimate tensile strength would decrease in response.

The plots for specimen A11, 14 and 17 shown in Fig. 4.14 suggest that holding the nozzle temperature constant at 215 °C and reducing the printing speed, from 60mm/s to 40mm/s to 20mm/s would initially decrease, then subsequently increase the specimen modulus. This would also initially decrease, then subsequently increase the specimen yield strength. The ultimate tensile strength would also initially decrease, then subsequently increase.

The plots for specimen A20, 23 and 26 shown in Fig. 4.15 suggest that holding the nozzle temperature constant at 200 °C and reducing the printing speed, from 60mm/s to

Table 4.2.
Mechanical properties of specimens printed in the y-axis orientation on the MakerBot 5th Gen. 3-D Printer

Specimen number	Modulus (ksi)	Yield strength (ksi)	Ultimate tensile strength (ksi)
A2	201.9015	0.42244	8.373
A5	205.4062	0.42984	7.856
A8	192.8354	0.38665	7.693
A11	203.1224	0.42538	8.377
A14	196.2084	0.37691	7.503
A17	200.2271	0.42172	8.162
A20	213.5352	0.4473	8.753
A23	207.5584	0.41528	8.192
A26	206.0683	0.4304	6.709

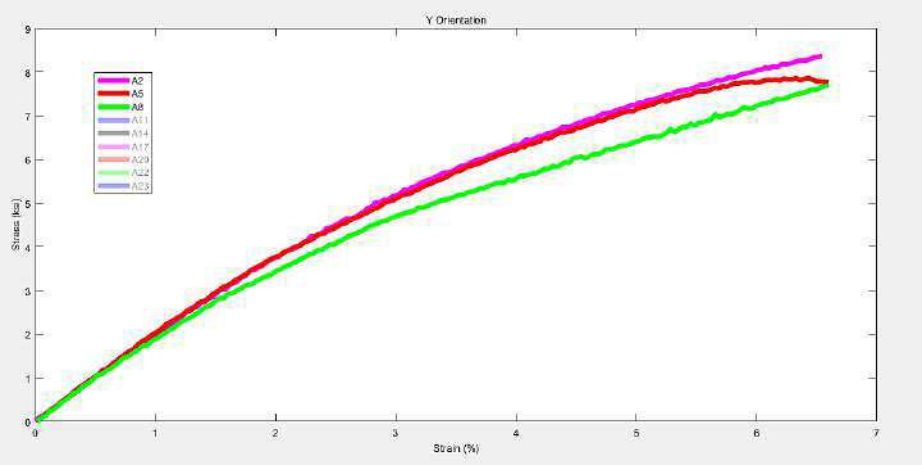

Figure 4.13. Plot of stress-strain curve for specimens A2, 5 and 8, printed in the y-axis orientation on the MakerBot 5th Gen. 3-D Printer.

40mm/s to 20mm/s would decrease in the specimen modulus. However, this would cause an initial decrease, then subsequent increase of the specimen yield strength. However the ultimate tensile strength continues decreasing.

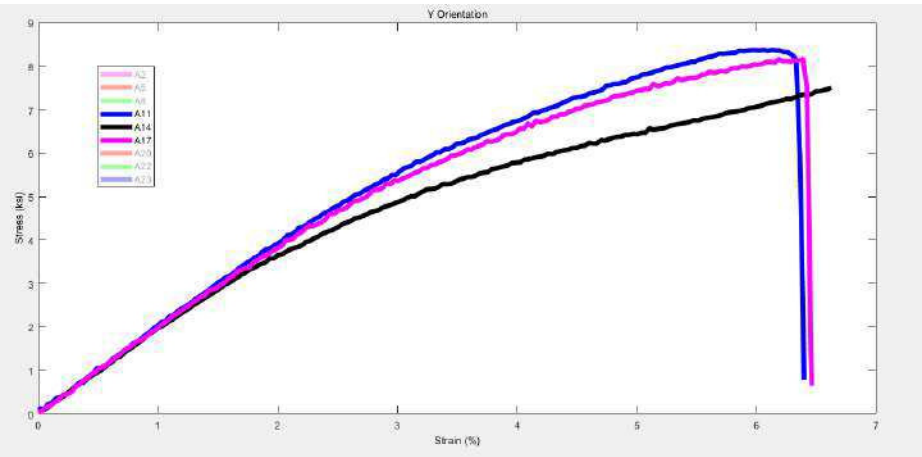

Figure 4.14. Plot of stress-strain curve for specimens A11, 14 and 17, printed in the y-axis orientation on the MakerBot 5th Gen. 3-D Printer.

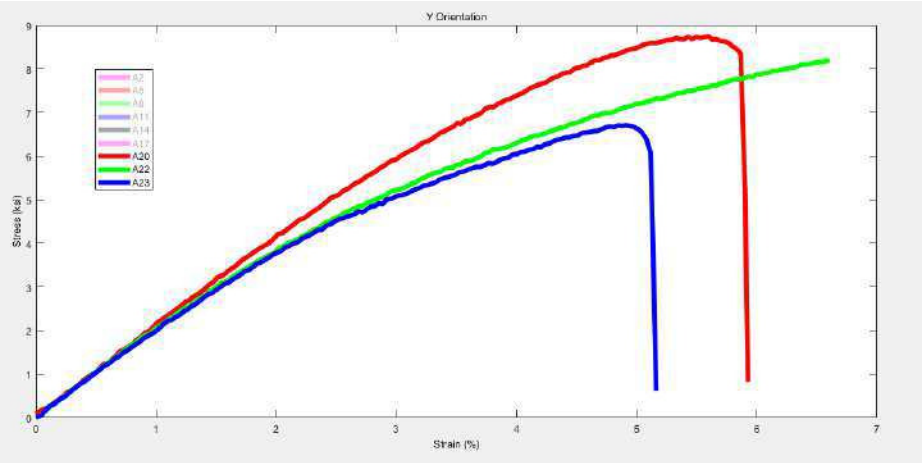

Figure 4.15. Plot of stress-strain curve for specimens A20, 23 and 26, printed in the y-axis orientation on the MakerBot 5th Gen. 3-D Printer.

For the specimens printed in the y-axis orientation specimen A20; printed with nozzle temperature of 200 °C and at printing speed of 60 mm/s possesses the highest yield strength, modulus and ultimate tensile strength. Specimen A14 (printed with nozzle temperature of 215 °C and at printing speed of 40 mm/s) is seen to possess the lowest modulus and yield strength. Fig. 4.16 presents the stress strain curve of all the specimens printed in the y axis orientation.

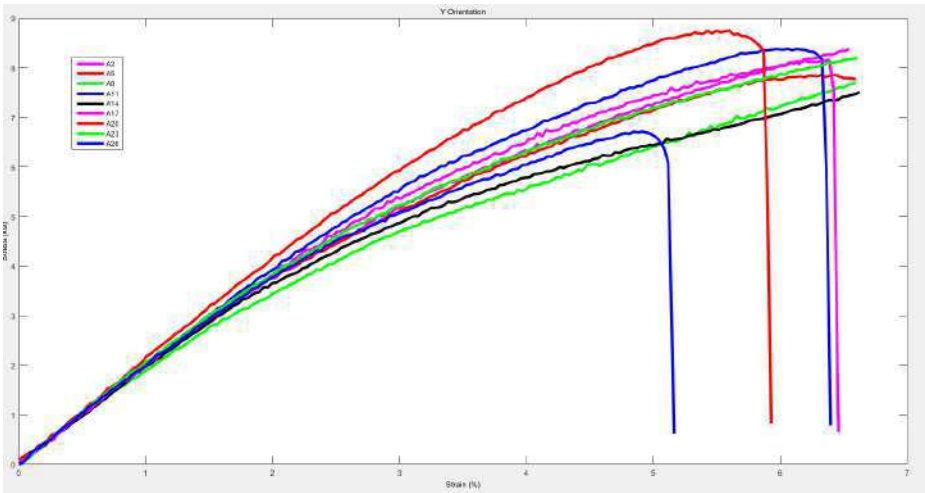

Figure 4.16. Plot of stress-strain curve for all specimens printed in the y-orientation on the MakerBot 5th Gen. 3-D Printer.

Values of the modulus, yield strength and ultimate tensile strength of the specimens gotten from the tensile strength analysis of the specimens printed in the z-axis orientation are presented in Table 4.3.

The plots for specimen A3, 6 and 9 shown in Fig. 4.17 suggest that holding the nozzle temperature constant at 220 °C and reducing the printing speed, from 60mm/s to 40mm/s to 20mm/s would increase the specimen modulus. This would also increase the specimen yield strength. However, the ultimate tensile strength initially decreases, then subsequently increases.

The plots for specimen A12, 15 and 18 shown in Fig. 4.18 suggest that holding the nozzle temperature constant at 215 °C and reducing the printing speed, from 60mm/s to 40mm/s to 20mm/s would initially decrease, then subsequently increase the specimen modulus. However, this would cause the specimen yield strength to increase. The ultimate tensile would initially increase, then subsequently decrease.

The plots for specimen A21, 24 and 27 shown in Fig. 4.19 suggest that holding the nozzle temperature constant at 200 °C and reducing the printing speed, from 60mm/s to 40mm/s to 20mm/s would decrease the specimen modulus. This would also decrease the

Table 4.3.
Mechanical properties of specimens printed in the z-axis orientation on the MakerBot 5th Gen. 3-D Printer

Specimen number	Modulus (ksi)	Yield strength (ksi)	Ultimate tensile strength (ksi)
A3	163.1846	0.31028	4.848
A6	160.4726	0.32245	3.599
A9	184.3235	0.37032	5.659
A12	184.7677	0.3842	5.427
A15	178.8283	0.39152	5.513
A18	188.1478	0.39475	5.336
A21	190.0429	0.37885	5.491
A24	162.6397	0.3418	5.58
A27	156.1865	0.3276	5.063

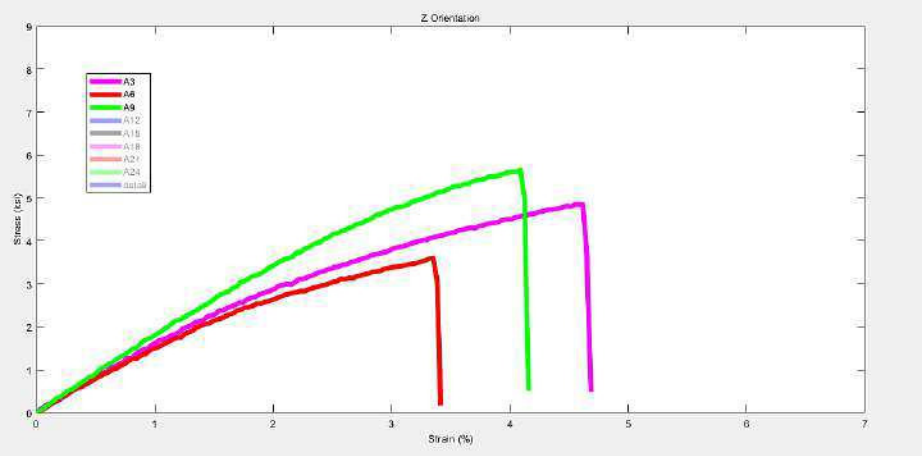

Figure 4.17. Plot of stress-strain curve for specimens A3, 6 and 9, printed in the z-axis orientation on the MakerBot 5th Gen. 3-D Printer.

specimen yield strength. However, the ultimate tensile strength initially increases, then subsequently decreases.

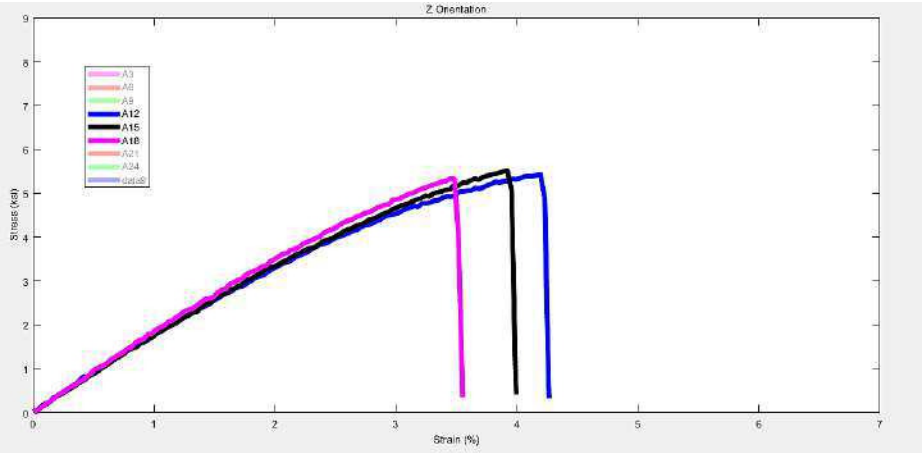

Figure 4.18. Plot of stress-strain curve for specimens A12, 15 and 18, printed in the z-axis orientation on the MakerBot 5th Gen. 3-D Printer.

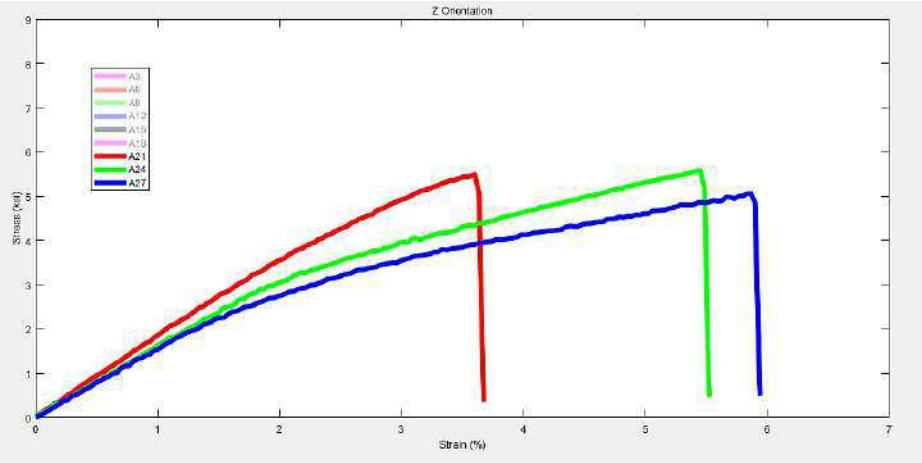

Figure 4.19. Plot of stress-strain curve for specimens A21, 24 and 27, printed in the z-axis orientation on the MakerBot 5th Gen. 3-D Printer.

For the specimens printed in the z-orientation Table 4.3, specimen A21; printed with nozzle temperature of 200 °C and at printing speed of 60 mm/s possesses the highest modulus. Specimen A18 (printed with nozzle temperature of 215 °C and at printing speed of 20mm/s) possesses the highest yield strength. Specimen A9 (printed with nozzle temperature of 220 °C and at printing speed of 40mm/s) is seen to possess the highest ultimate tensile strength. Specimen A27 (printed with nozzle temperature of 200 °C and

at printing speed of 20mm/s), possess the lowest modulus and yield strength. Fig. 4.20 presents the plot for stress strain curve of the specimens printed in the z orientation.

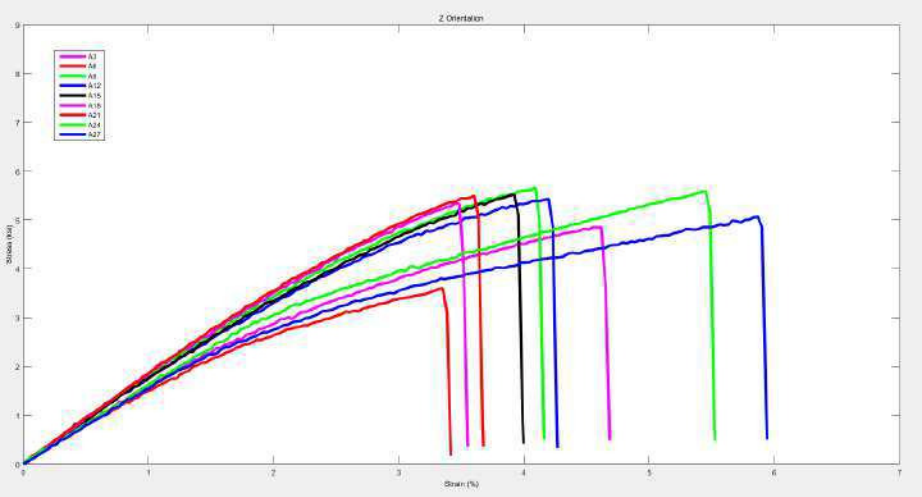

Figure 4.20. Plot of stress-strain curve for all specimens printed in the z-axis orientation on the MakerBot 5th Gen. 3-D Printer.

Values of the modulus, yield strength and ultimate tensile strength of the specimens gotten from the tensile strength analysis of the specimens printed in the 45 degree axis orientation are presented in Table 4.4

The plots for specimen A28, 29 and 30 as shown in Fig. 4.21 suggest that holding the nozzle temperature constant at 220 °C and reducing the printing speed, from 60mm/s to 40mm/s to 20mm/s would initially increase, then subsequently decrease the specimen modulus. This would also initially increase, then subsequently decrease the specimen yield strength. However the ultimate tensile strength continues decreasing.

The plots for specimen A31, 32 and 33 shown in Fig. 4.22 suggest that holding the nozzle temperature constant at 215 °C and reducing the printing speed, from 60mm/s to 40mm/s to 20mm/s would decrease the specimen modulus. This would also decrease the specimen yield strength. However, the ultimate tensile strength initially decreases, then subsequently increases.

The plots for specimen A34, 35 and 36 shown in Fig. 4.23 suggest that holding the nozzle temperature constant at 200 °C and reducing the printing speed, from 60mm/s

Table 4.4.
Mechanical properties of specimens printed in the 45 degree axis orientation on the MakerBot 5th Gen. 3-D Printer

Specimen number	Modulus (ksi)	Yield strength (ksi)	Ultimate tensile strength (ksi)
A28	90.48767	0.19042	1.167
A29	97.51946	0.19422	1.455
A30	78.56346	0.14316	0.501
A31	87.12378	0.19391	1.624
A32	84.57848	0.17918	1.106
A33	80.65544	0.1571	1.663
A34	82.35858	0.1572	1.153
A35	74.89029	0.16172	1.679
A36	100.3899	0.1731	0.997

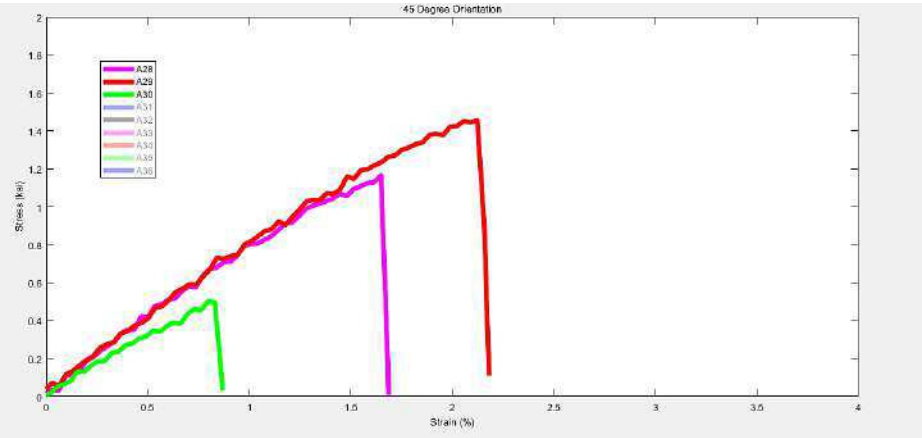

Figure 4.21. Plot of stress-strain curve for specimens A28, 29 and 30, printed in the 45 degree axis orientation on the MakerBot 5th Gen. 3-D Printer.

to 40mm/s to 20mm/s would initially decrease, then subsequently increase the specimen modulus. However this would cause the specimen yield strength to increase. The ultimate tensile strength would initially increase, then subsequently decrease.

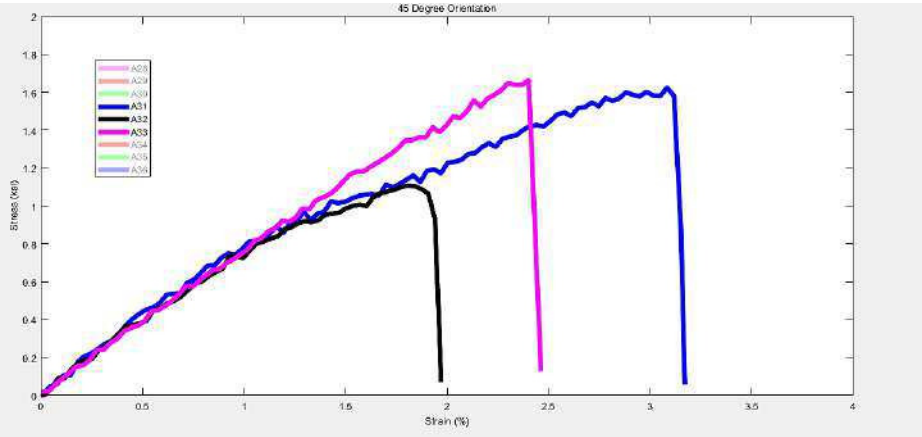

Figure 4.22. Plot of stress-strain curve for specimens A31, 32 and 33, printed in the 45 degree axis orientation on the MakerBot 5th Gen. 3-D Printer.

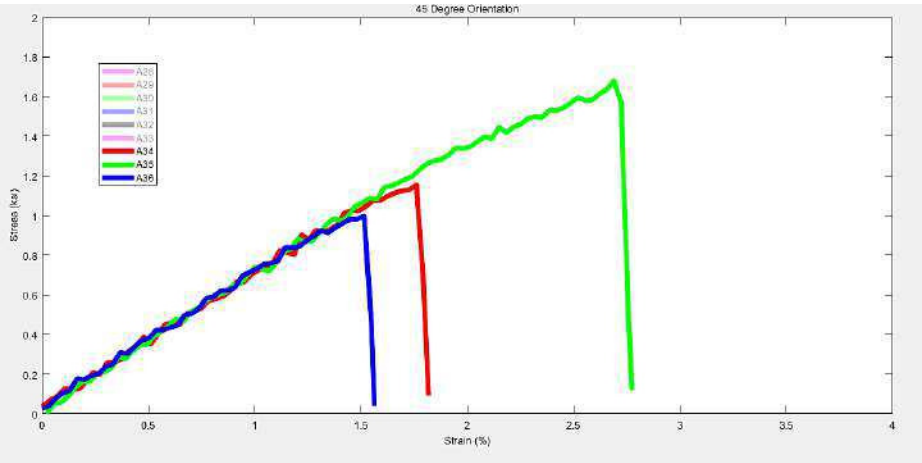

Figure 4.23. Plot of stress-strain curve for specimens A34, 35 and 36, printed in the 45 degree axis orientation on the MakerBot 5th Gen. 3-D Printer.

For the specimens printed in the 45 degree axis orientation Table 4.4, specimen A36; printed with nozzle temperature of 200 °C and at printing speed of 20mm/s possesses the highest modulus. Specimen A29 (printed with nozzle temperature of 220 °C and at printing speed of 40 mm/s) possesses the highest yield strength. Specimen A35 (printed with nozzle temperature of 200 °C and at printing speed of 40mm/s) is seen to possess the highest ultimate tensile strength. Specimen A35 (printed with nozzle temperature of

200 °C and at printing speed of 40mm/s), also possess the lowest modulus. Specimen A30 (printed with nozzle temperature of 220 °C and at printing speed of 20mm/s), possessed the lowest yield strength. Fig. 4.24 presents the plot for stress strain curve of the specimens printed in the 45 degree axis orientation.

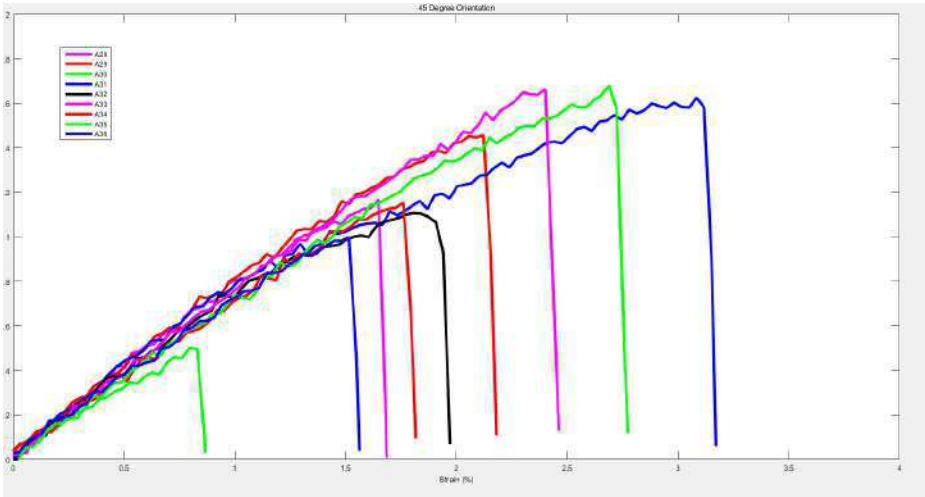

Figure 4.24. Plot of stress-strain curve for all specimens printed in the 45 degree axis orientation on the MakerBot 5th Gen. 3-D Printer.

The results from the initial printing and evaluation indicate that the specimens printed in the yaxis orientation show better mechanical properties than the specimen printed in the x, z and 45 degree axis orientation.

4.2 Results from the Specimens Fabricated on the AirWolf 3-D Printer

In-situ monitoring of the fabrication process was performed during the printing of specimens B1 to B27 Fig. 4.25. The thermal evolution of each part was monitored and thermal data plots retrieved using the FLIR research camera and Research IR Max software as mentioned in Section 3.2. Thermal data was acquired for each of the specimens. The figures presented are for specimens printed in the x- axis, y- axis and z-axis orientation as shown in Fig. 3.6. During the printing process, it was observed that the specimens fabricated in the x-axis orientation took the shortest time to print. This was due to the

fewer layers required to complete the part build in this orientation. The specimens printed in the z-axis orientation took considerably longer to print. This was due to the requirement of support structure and the specimen height. The AirWolf 3-D printer had difficulty in building the specimens in the y-axis and z-axis orientation. Fig. 4.25 shows the specimens prior to tensile strength evaluation on the Q-test machine. These specimens were printed using different orientation axes (x, y and z) and adjusting the printing parameters (nozzle temperature and print speed). The effect of the print speed on the build time was observed to influence the build process. The mechanical analysis also showed the influence of the print speed parameter on the build process and final product mechanical properties. Support structures were implemented to accomplish the part build in the x- and y- axis orientation.

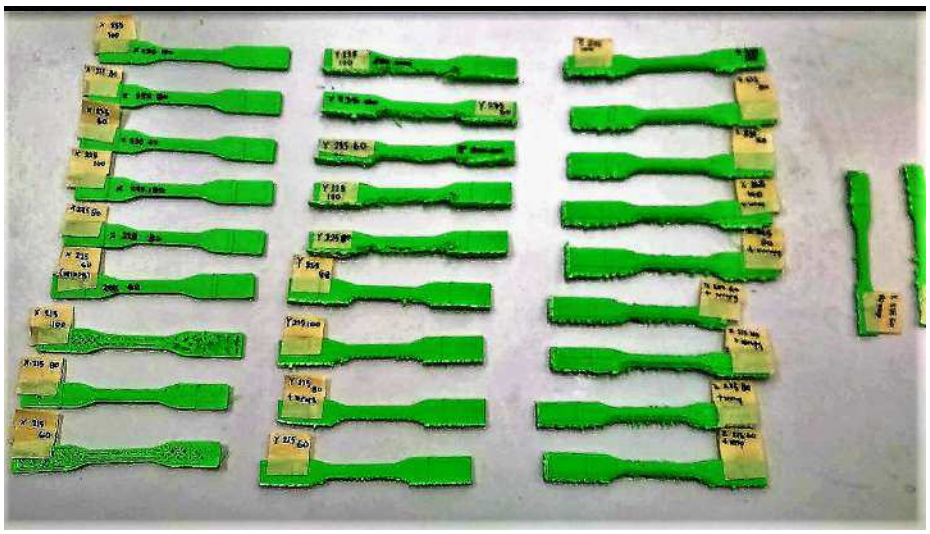

Figure 4.25. Specimen B1 to B27 printed on the AirWolf 3-D printer prior to evaluation on the Q-test machine.

4.2.1 Thermography Results from the Specimens Fabricated on the AirWolf 3-D Printer

The thermal images and thermal data plots for select specimens printed in the x, y and z-axis orientation are shown in Fig. 4.27 - 4.95. Each layer captured by the IR camera shows;

- the actual IR image of in-situ monitoring of the specimen layer being built (on the GUI left)
- the temperature profile (on the GUI top right)
- the temporal plot (on the GUI bottom right)
- other related information to the build process include, the temperature range band and the number of frames captured by the FLIR research camera during the monitoring process

The temperature profile plot gives average temperature in the column of pixels in the monitored region of interest (ROI). Thus providing information on the average temperature and distribution of temperature over the built layer surface. The ROI in this case is the region showing layer wise material deposition process as specimen individual layers are being built. Three generic plot trends Fig. 4.26a (top left), b (top right) and c (bottom left) were observed during the monitoring process of the specimens in the x-axis, y-axis and z-axis orientation. These plots were observed to occur based on the start point of the printer nozzle and the pattern followed in material deposition.

In the temperature profile plot trend shown in Fig. 4.26a, average temperature retrieved from the ROI column of pixels is initially high; then gradually reduces in magnitude. This occurs when the material deposition pattern is from the geometric origin of layer being printed then follows along entire length of the specimen to the geometric endpoint of layer being printed. In the temperature profile plot trend shown in Fig. 4.26b, average temperature retrieved from the ROI column of pixels is initially low; then gradually increases in magnitude. This occurs when the material deposition pattern is from the geometric endpoint of layer being printed then follows along entire length of the specimen to the geometric origin of layer being printed. In the temperature profile plot trend shown in Fig. 4.26c, average temperature retrieved from the ROI column of pixels is initially high and although gradually reduces in magnitude; begins again to gradually increase in magnitude. This occurs when the material deposition pattern begins either from the

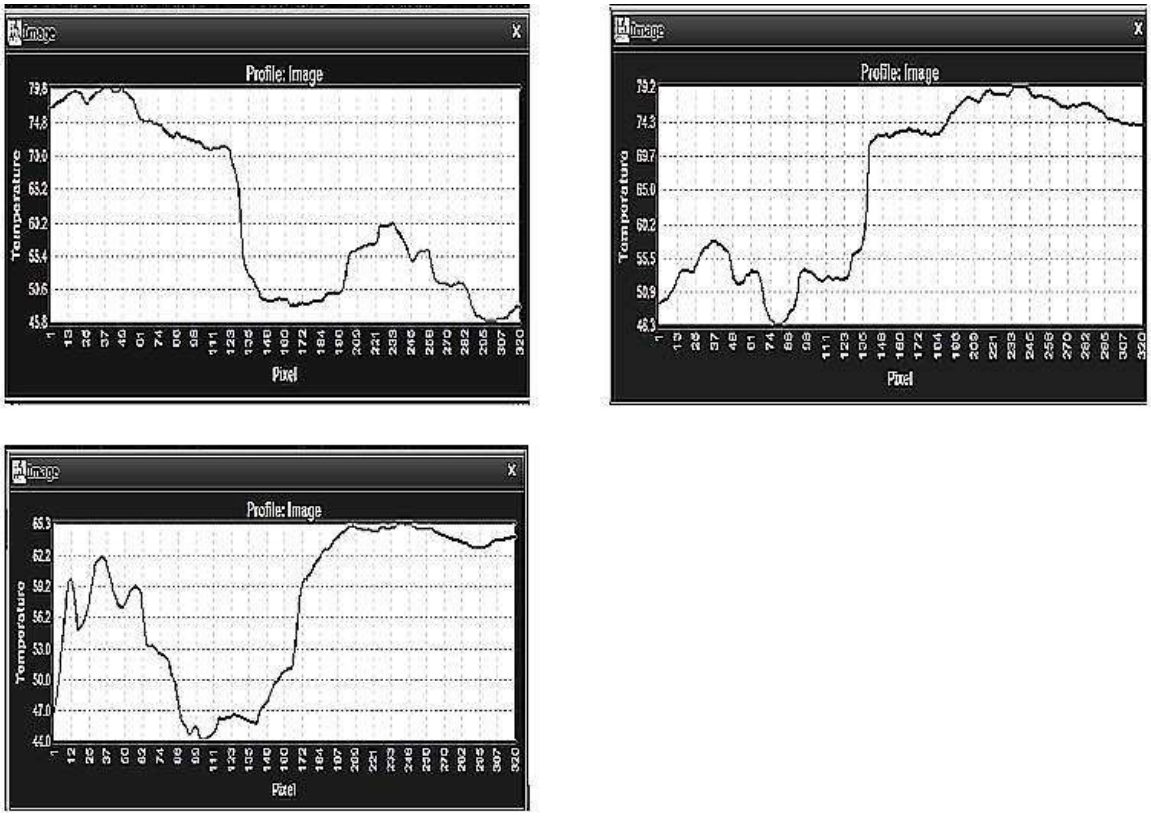

Figure 4.26. Generic plot trends: a (top left), b (top right) and c (bottom left) observed during monitoring process of printing the specimen.

geometric origin or endpoint of layer being printed. Then continues to a point along the length of the specimen layer being printed. It then skips to the opposite end of that layer and begins to deposit material while returning to the skip-point. These material deposition patterns (print strategy) were repeated as the successive layers were built.

The specimens printed in the x-axis orientation required 35 layers to be built. Fig. 4.27 - 4.50, show the layer wise thermal evolution of specimen B4. As aforementioned, the thermal profile plot provides information on the part build temperature with respect to the distribution of heat across the layer surface. The temporal plot provides information on the surface layer surface thermal distribution with respect to time elapsed. The nature of the generated curves can be interpreted to determine part layer wise thermal evolution and the uniformity of heat in successive part built layers.

The temporal plot presents data on the layer surface temperature with respect to printing time. The layer surface temperature is influenced by interaction between the area closest to the printer nozzle (heat affected zone HAZ) as the material being deposited, the already deposited material on that layer and previously built layers. The temporal plot also shows distribution of temperature through the specimen built layers. In observing the temporal plot, a smooth plot suggests a more evenly distributed temperature at the layer being built and between the layer being built and preceding layers. Smoother temporal plots were observed to occur more during printing in the y-axis orientation and x-axis orientation. The fluctuations observed in the temporal plots are attributed to the presence of intermittent pores and dense regions in the specimen being built. The fluctuations in the plot are also influenced by the temperature differences between the interacting regions (the area closest to the printer nozzle as the material being deposited, the already deposited material on that layer and previously built layers). The temporal plots of the initial layers of the specimens were also seen to have more fluctuations, than the specimen mid and final build layers. The availability of more deposited material since more layers have been built serve as heat sink and thus facilitate more even distribution of temperature with respect to time at the layer and between the already built layers. The fluctuations observed in the temporal plots could be attributed to the presence of intermittent pores and dense regions in the specimen being built. The temporal plots of the initial layers of the specimens were also seen to have more fluctuations. Due to the large volume of image data and information from mechanical properties data in the results gotten from specimen A1 to A36 and B1 to B27, the thermal images selected for this report are for;

- specimen B4 (printed in the x-axis orientation with nozzle temperature of 235 °C and print speed of 80mm/s)
- specimen B5 (printed in the y-axis orientation with nozzle temperature of 235 °C and print speed of 80mm/s
- specimen B6 (printed in the z-axis orientation with nozzle temperature of 235 °C and print speed of 80mm/s)

4.2.2 Thermography Results from the Specimens Fabricated on the AirWolf 3-D Printer in the x-axis Orientation

Fig. 4.27 - 4.28 show the Research IR Max software user interface for the in-situ monitoring of specimen B4 layers 1 and 2 of 35 layers. As earlier stated, the infra-red image of the build process showing material; deposition and the building of the part in successive layers is shown on the GUI left. The temperature profile on the GUI right shows the trend referred to in Fig. 4.26b.

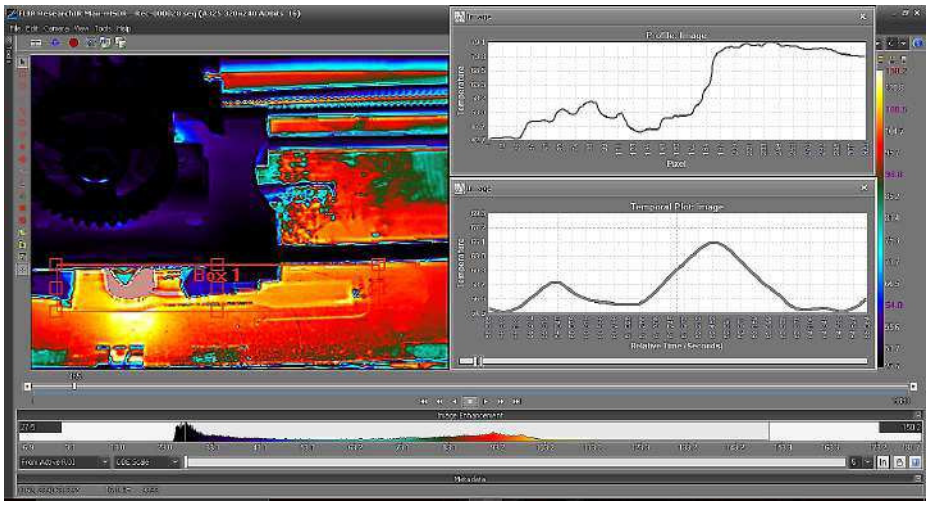

Figure 4.27. Thermal evolution and plot for specimen B4 layer 1.

In this case, average temperature retrieved from the temperature profile plot in ROI column of pixels is initially low; then gradually increases in magnitude. Here the material deposition pattern is from the geometric endpoint of layer being printed and retraced along entire length of the specimen to the geometric origin of the layer being printed. The temporal plot here indicates significant fluctuation in response to the temperature differences between the interacting regions. Fig. 4.29, 4.30 and 4.31 show the Research IR Max software user interface for the in-situ monitoring of specimen B4 layers 3, 4 and 5 out of the complete specimen build of 35 layers. As earlier stated, the infra-red image of the build process showing material; deposition and the building of the part in successive layers is shown on the GUI left. The temperature profile on the GUI right shows the trend

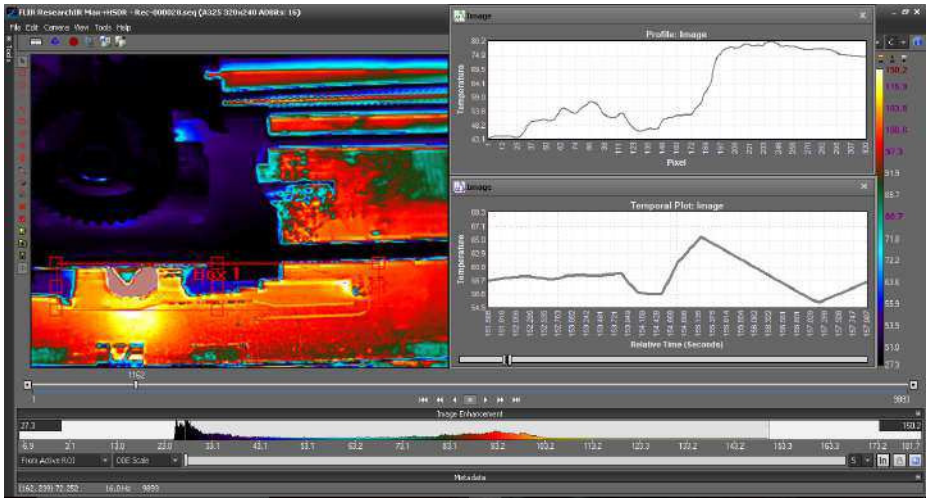

Figure 4.28. Thermal evolution and plot for specimen B4 layer 2.

referred to in Fig. 4.26a. Here; average temperature retrieved from the temperature profile plot in the ROI column of pixels is initially high, then gradually reduces in magnitude. This implies that the material deposition pattern is from the geometric origin of layer being printed and flowing along entire length of the specimen to the layers geometric endpoint. The temporal plot l show significant irregularity at this early stage in the build process.

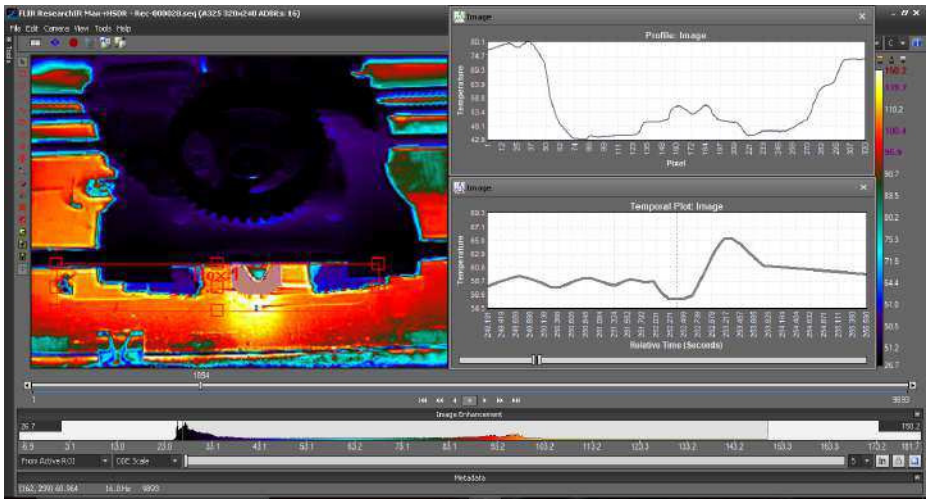

Figure 4.29. Thermal evolution and plot for specimen B4 layer 3.

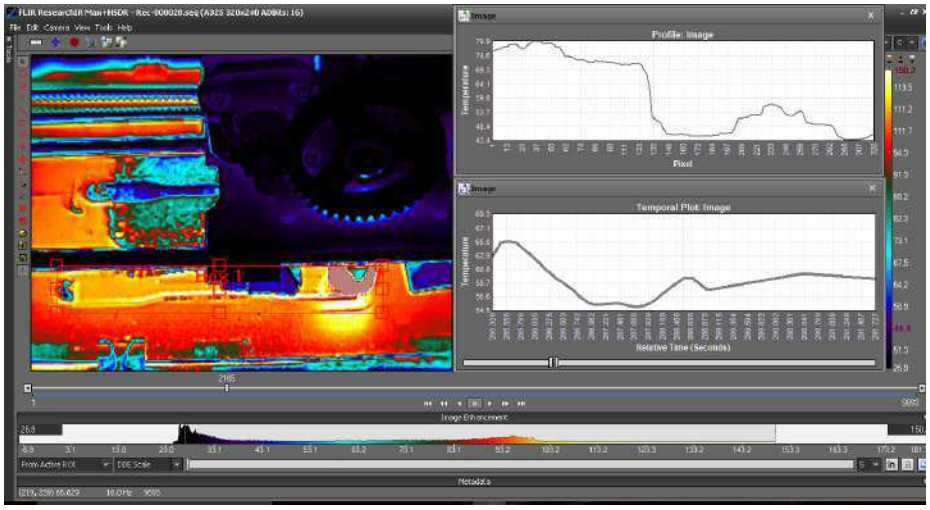

Figure 4.30. Thermal evolution and plot for specimen B4 layer 4.

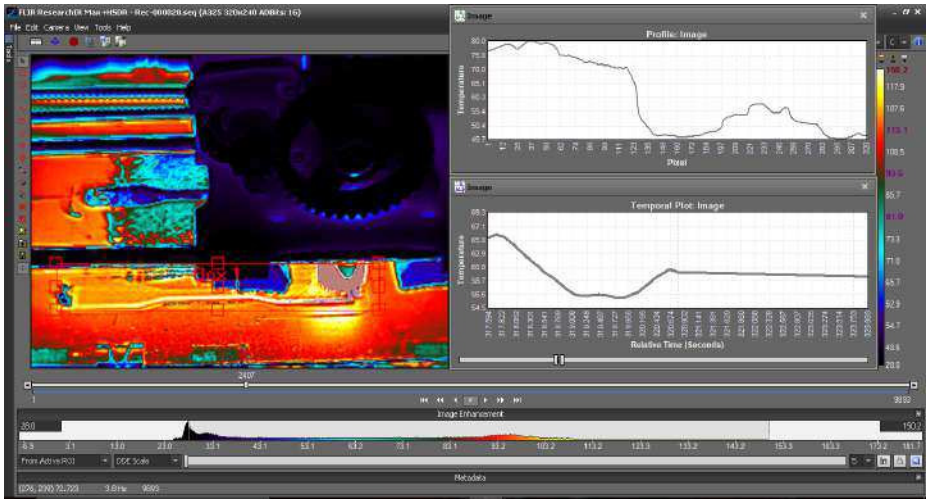

Figure 4.31. Thermal evolution and plot for specimen B4 layer 5.

Fig. 4.32 shows the Research IR Max software user interface for the in-situ monitoring of specimen B4 layer 6 out of the complete specimen build of 35 layers. As earlier stated, the infra-red image of the build process showing material; deposition and the building of the part in successive layers is shown on the GUI left. The temperature profile on the GUI top right shows the trend referred to in Fig. 4.26b. Here; average temperature retrieved from the temperature profile plot in the ROI column of pixels is initially low.

Then gradually increases in magnitude. Implying that the material deposition pattern is from the geometric origin of layer being printed and flowing along entire length of the specimen to the layers geometric endpoint. Although the temporal plot shows initial irregularity, it gradually begins to show more evenness.

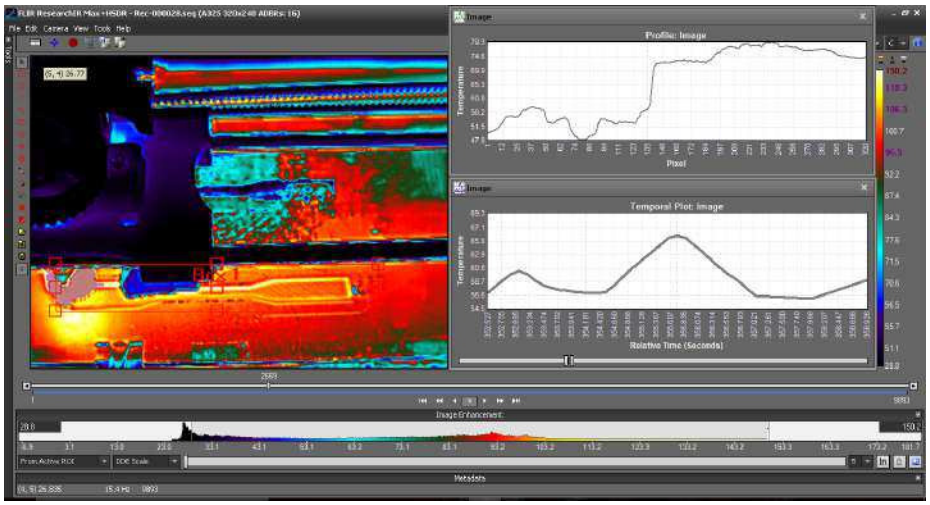

Figure 4.32. Thermal evolution and plot for specimen B4 layer 6.

Fig. 4.33 shows the Research IR Max software user interface for the in-situ monitoring of specimen B4 layer 7 of 35 layers. As earlier stated, the infra-red image of the build process showing material deposition and the building of the part in successive layers is shown on the GUI left. The temperature profile on the GUI top right shows the trend referred to in Fig. 4.26b. In this case, average temperature retrieved from the temperature profile plot in ROI column of pixels is initially low; then gradually increases in magnitude. Here the material deposition pattern is from the geometric endpoint of layer being printed and retraced along entire length of the specimen to the geometric origin of the layer being printed. Although the temporal plot shows initial irregularity, it gradually begins to show more evenness.

Fig. 4.34 shows the Research IR Max software user interface for the in-situ monitoring of specimen B4 layer 8 of 35 layers. As earlier stated, the infra-red image of the build process showing material deposition and the building of the part in successive layers is shown on the GUI left. The temperature profile on the GUI top right shows the trend referred to in Fig.

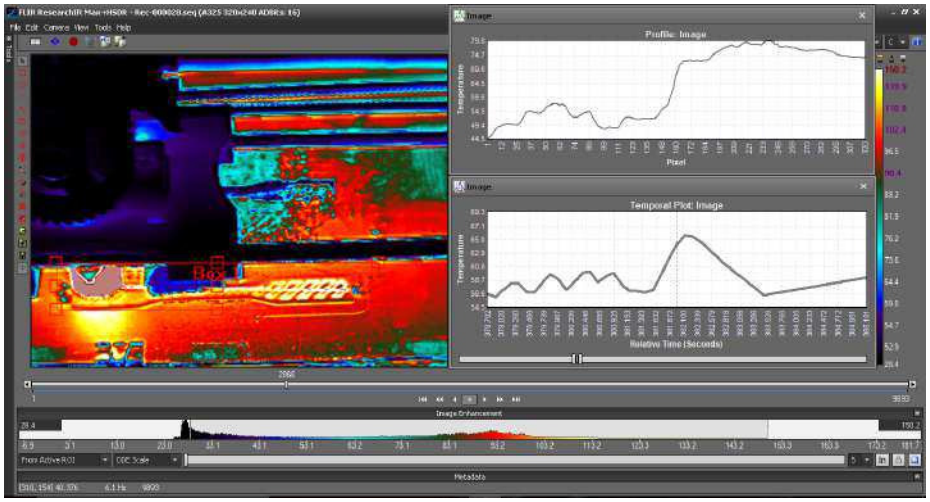

Figure 4.33. Thermal evolution and plot for specimen B4 layer 7.

4.26b. In this case, average temperature retrieved from the temperature profile plot in ROI column of pixels is initially low; then gradually increases in magnitude. Here the material deposition pattern is from the geometric endpoint of layer being printed and retraced along entire length of the specimen to the geometric origin of the layer being printed. Although the temporal plot shows initial irregularity, it gradually begins to show more evenness.

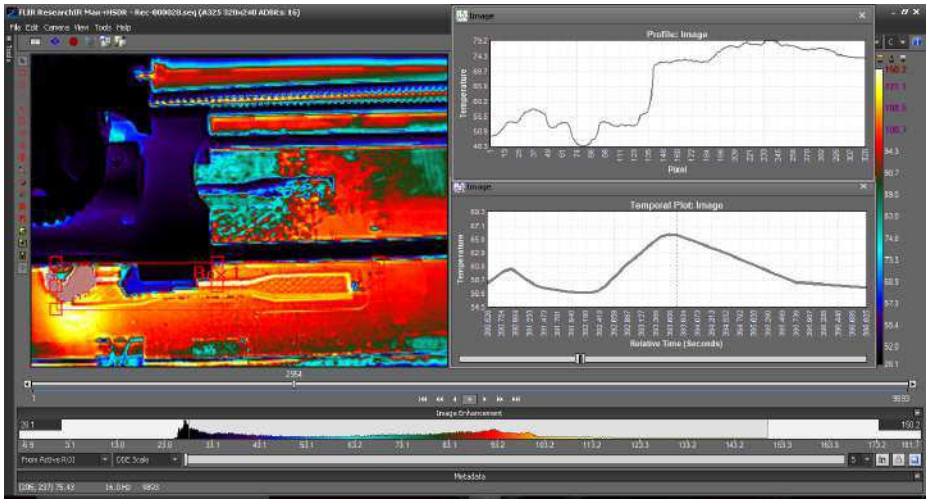

Figure 4.34. Thermal evolution and plot for specimen B4 layer 8.

Fig. 4.35 shows the Research IR Max software user interface for the in-situ monitoring of specimen B4 layer 9 of 35 layers. As earlier stated, the infra-red image of the build process showing material deposition and the building of the part in successive layers is shown on the GUI left. The temperature profile on the GUI top right shows the trend referred to in Fig. 4.26b. In this case, average temperature retrieved from the temperature profile plot in ROI column of pixels is initially low; then gradually increases in magnitude. Here the material deposition pattern is from the geometric endpoint of layer being printed and retraced along entire length of the specimen to the geometric origin of the layer being printed. Although the temporal plot shows initial irregularity, it gradually begin to show more eveness.

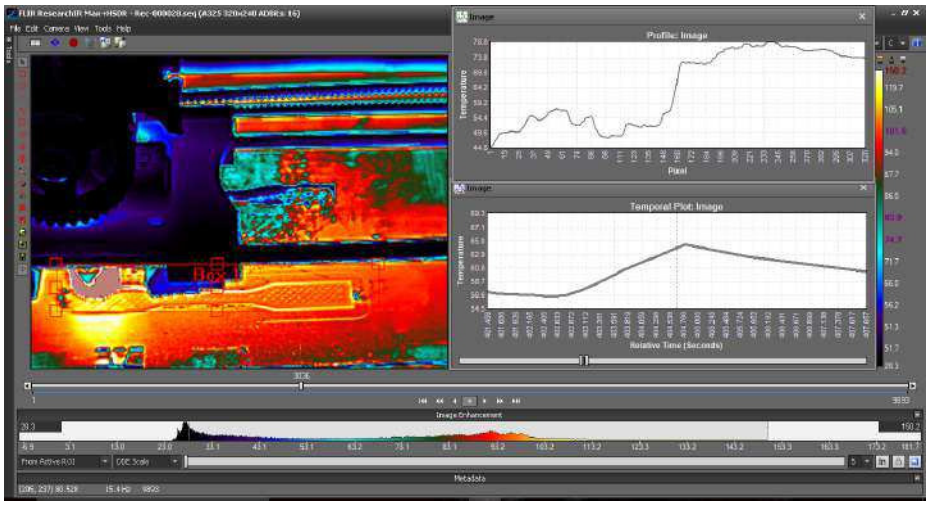

Figure 4.35. Thermal evolution and plot for specimen B4 layer 9.

Fig. 4.36 shows the Research IR Max software user interface for the in-situ monitoring of specimen B4 layer 10 of 35 layers. As earlier stated, the infra-red image of the build process showing material deposition and the building of the part in successive layers is shown on the GUI left. The temperature profile on the GUI top right shows the trend referred to in Fig. 4.26b as discussed in Section 4.2.1 . In this case, average temperature retrieved from the temperature profile plot in ROI column of pixels is initially low; then gradually increases in magnitude. Here the material deposition pattern is from the geometric endpoint of layer

being printed and retraced along entire length of the specimen to the geometric origin of the layer being printed. At this stage in the build process the temporal plot shows eveness.

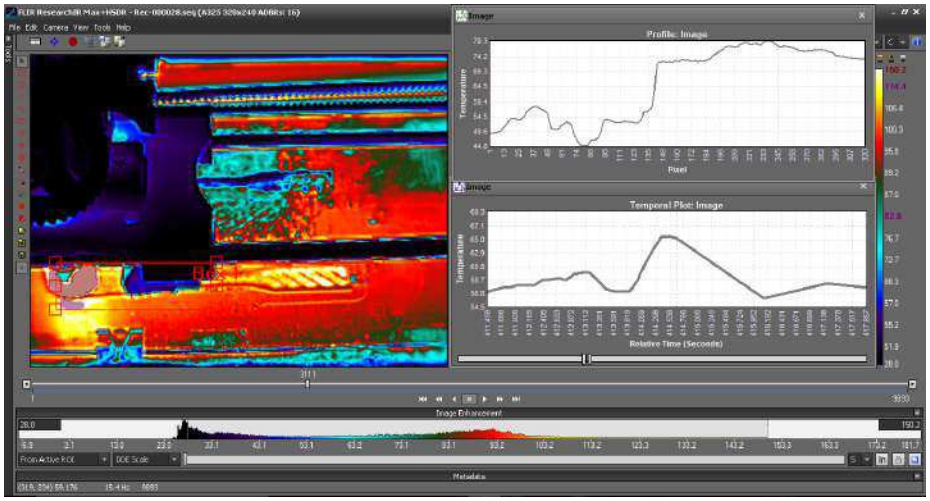

Figure 4.36. Thermal evolution and plot for specimen B4 layer 10.

The following figures, Fig. 4.37 - 4.40, show the Research IR Max software user interface for the in-situ monitoring of specimen B4 layers 11 16 of 35 layers. At this stage of the build process he specimen is about half complete. As earlier stated, the infra-red image of the build process showing material; deposition and the building of the part in successive layers is shown on the GUI left. The temperature profile on the GUI top right for these layers show the trend discussed and referred to in Fig. 4.26b.

In this case, average temperature retrieved from the temperature profile plot in ROI column of pixels is initially low; then gradually increases in magnitude. Here the material deposition pattern is from the geometric endpoint of layer being printed and retraced along entire length of the specimen to the geometric origin of the layer being printed. The irregularity I the temporal plots are reduced. AS the already built layers ow form a major contributor to the interacting regions.

The following figures Fig. 4.41 - 4.44 , are similar to the just discussed layers. The Research IR Max software user interface for the in-situ monitoring of specimen B4 layers 17 20 of 35 layers. At this stage of the build process the specimen is over half complete. As

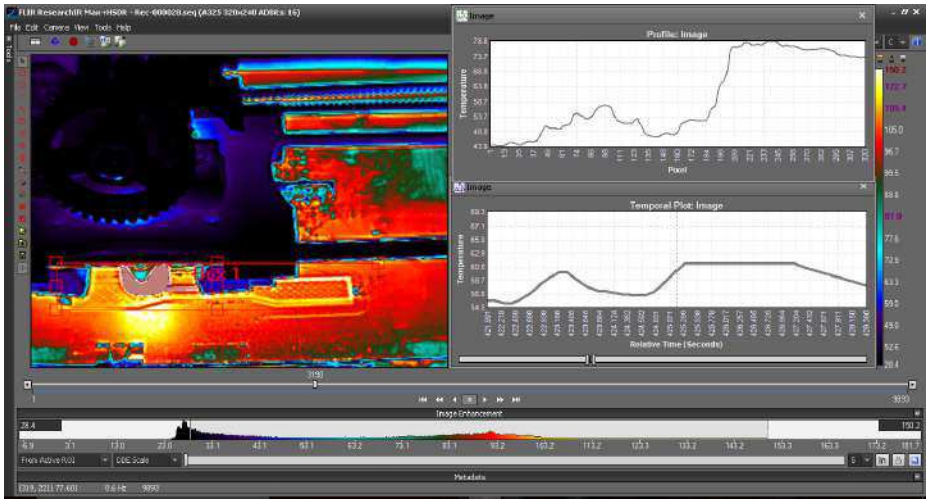

Figure 4.37. Thermal evolution and plot for specimen B4 layer 11.

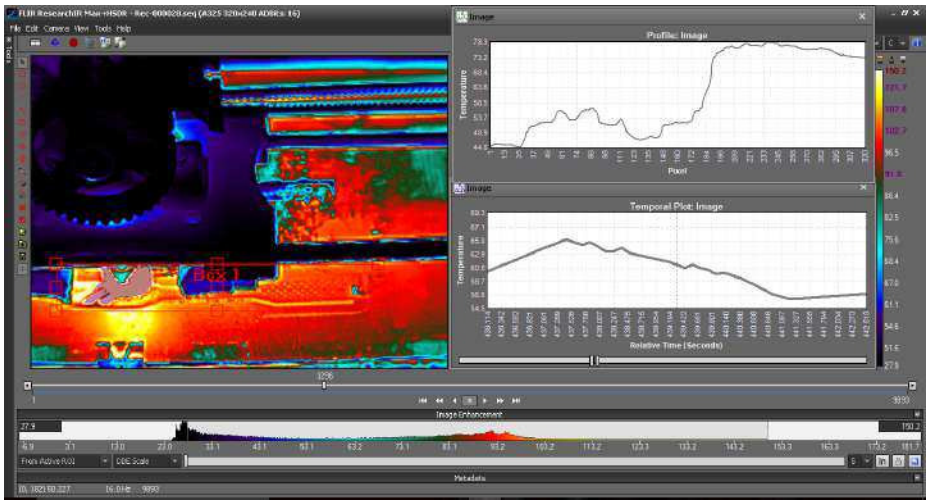

Figure 4.38. Thermal evolution and plot for specimen B4 layer 12.

earlier stated, the infra-red image of the build process showing material; deposition and the building of the part in successive layers is shown on the GUI left. The temperature profile on the GUI top right for these layers show the trend discussed and referred to in Fig. 4.26b.

In this case, average temperature retrieved from the temperature profile plot in ROI column of pixels is initially low; then gradually increases in magnitude. Here the material deposition pattern is from the geometric endpoint of layer being printed and retraced

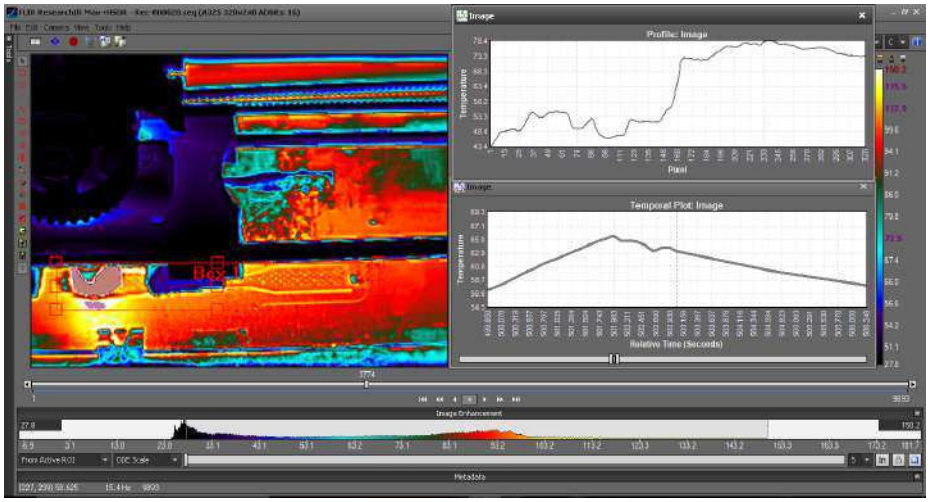

Figure 4.39. Thermal evolution and plot for specimen B4 layer 15.

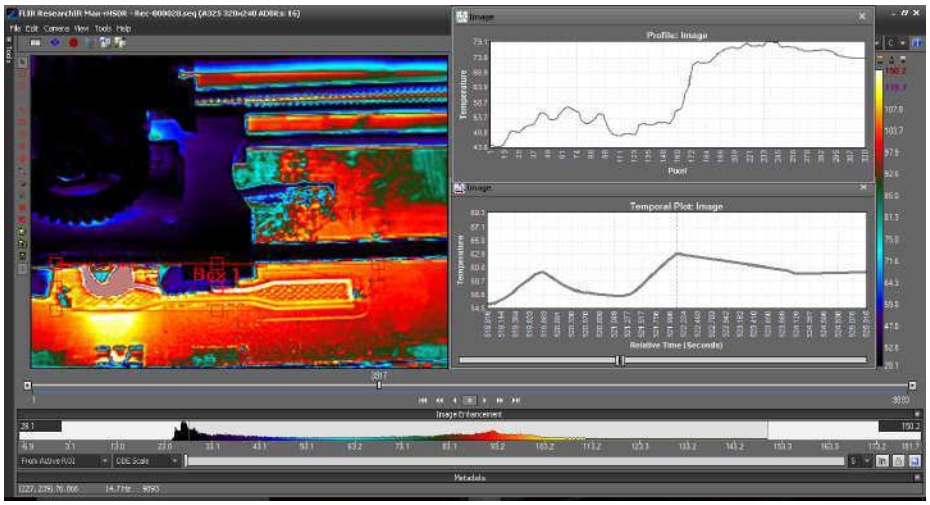

Figure 4.40. Thermal evolution and plot for specimen B4 layer 16.

along entire length of the specimen to the geometric origin of the layer being printed. The irregularity I the temporal plots are reduced. As the already built layers ow form a major contributor to the interacting regions.

In the following figures Fig. 4.45 - 4.46, the Research IR Max software user interface for the in-situ monitoring of specimen B4 layers 30 and 31 of 35 layers. At this later stage of the build process the specimen is at the final stage of completion. As earlier stated, the

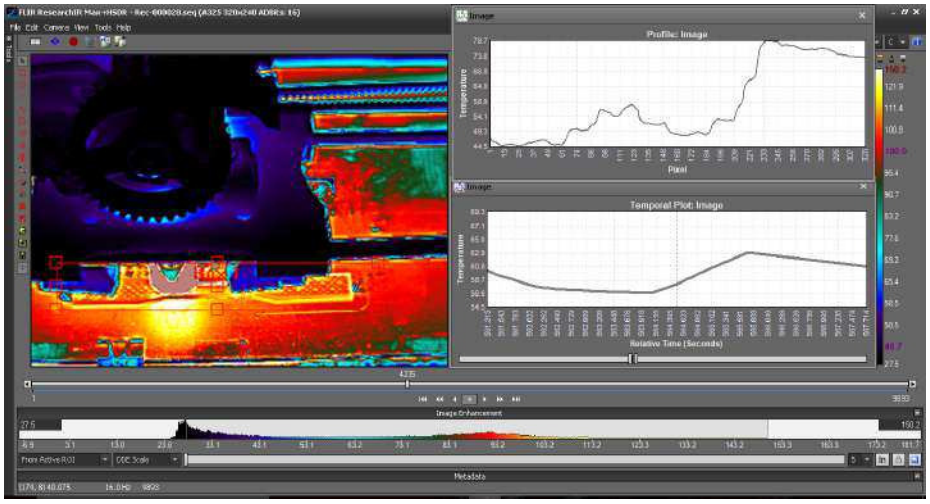

Figure 4.41. Thermal evolution and plot for specimen B4 layer 17.

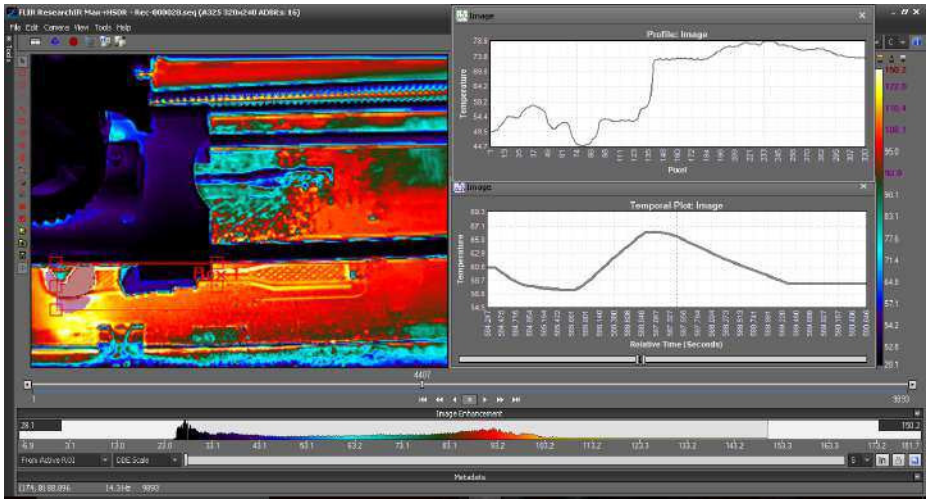

Figure 4.42. Thermal evolution and plot for specimen B4 layer 18.

infra-red image of the build process showing material; deposition and the building of the part in successive layers is shown on the GUI left. The temperature profile on the GUI top right for these layers show the trend discussed and referred to in Fig. 4.26a.

Here, average temperature retrieved from the temperature profile plot in the ROI column of pixels is initially high, then gradually reduces in magnitude. This implies that the material deposition pattern is from the geometric origin of layer being printed and flowing along

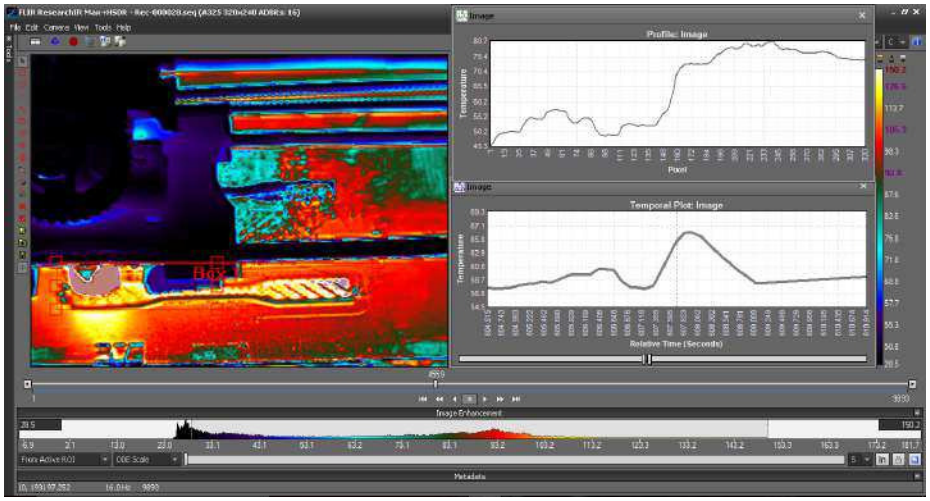

Figure 4.43. Thermal evolution and plot for specimen B4 layer 19.

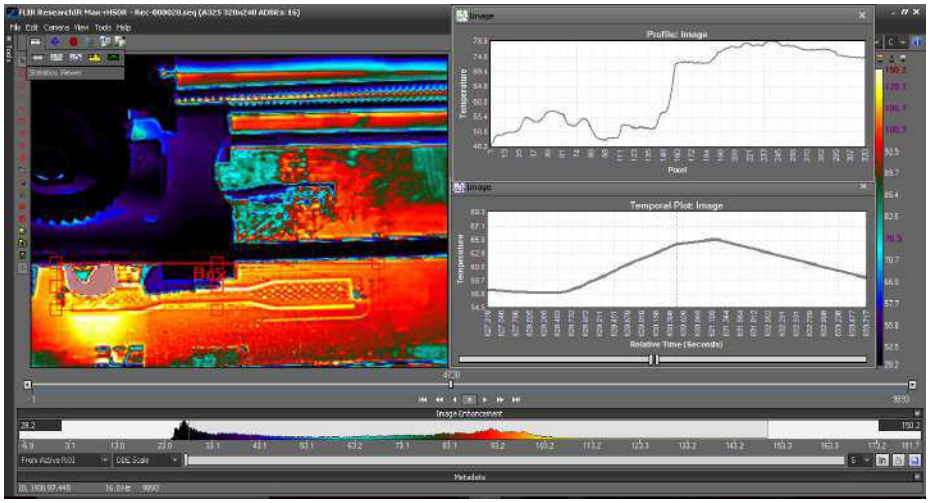

Figure 4.44. Thermal evolution and plot for specimen B4 layer 20.

entire length of the specimen to the layers geometric endpoint. The temporal plot indicates a more evenly distributed temperature between the interacting regions at this stage.

In the following figures Fig. 4.47 - 4.48, show the Research IR Max software user interface for the in-situ monitoring of specimen B4 layers 32 and 33 of 35 layers. At this later stage of the build process the specimen is at the final stage of completion. As earlier stated, the infra-red image of the build process showing material; deposition and

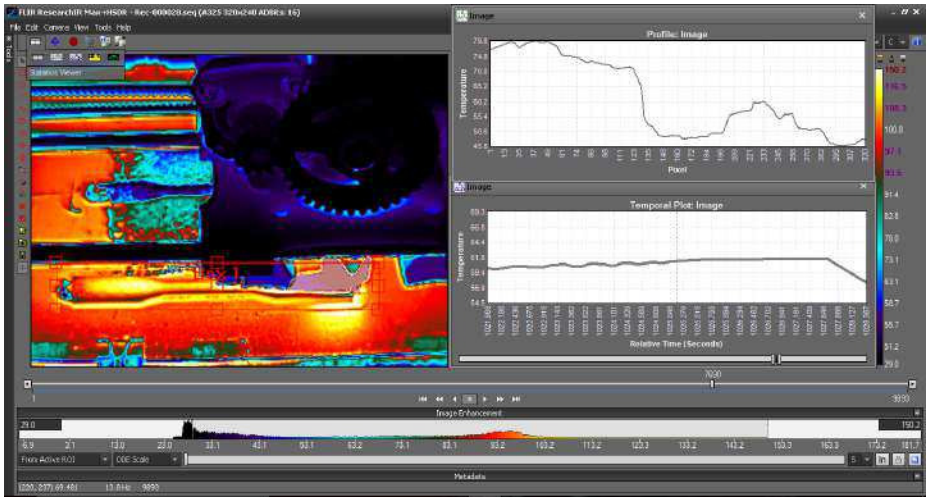

Figure 4.45. Thermal evolution and plot for specimen B4 layer 30.

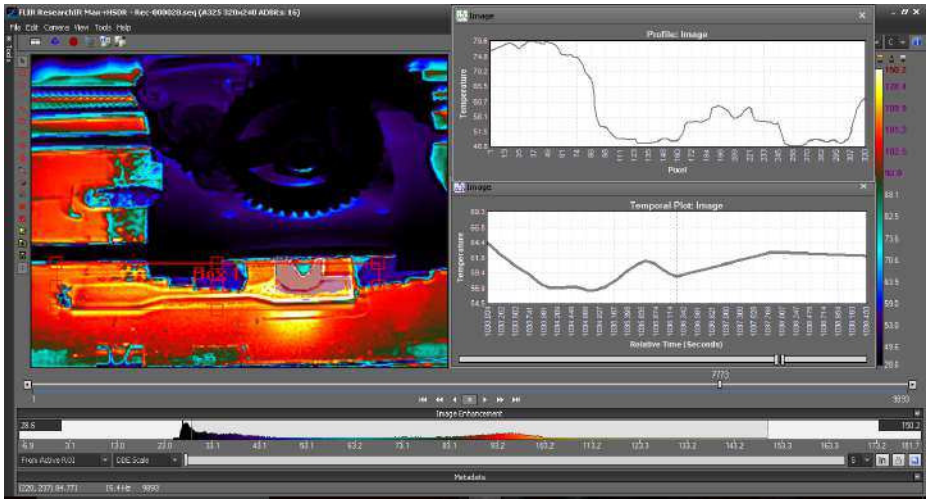

Figure 4.46. Thermal evolution and plot for specimen B4 layer 31.

the building of the part in successive layers is shown on the GUI left. The temperature profile on the GUI top right for these layers show the trend referred to in Fig. 4.26b

In this case, average temperature retrieved from the temperature profile plot in ROI column of pixels is initially low; then gradually increases in magnitude. Here the material deposition pattern is from the geometric endpoint of layer being printed and retraced along entire length of the specimen to the geometric origin of the layer being printed. The temporal plot, indicates significant uniformity.

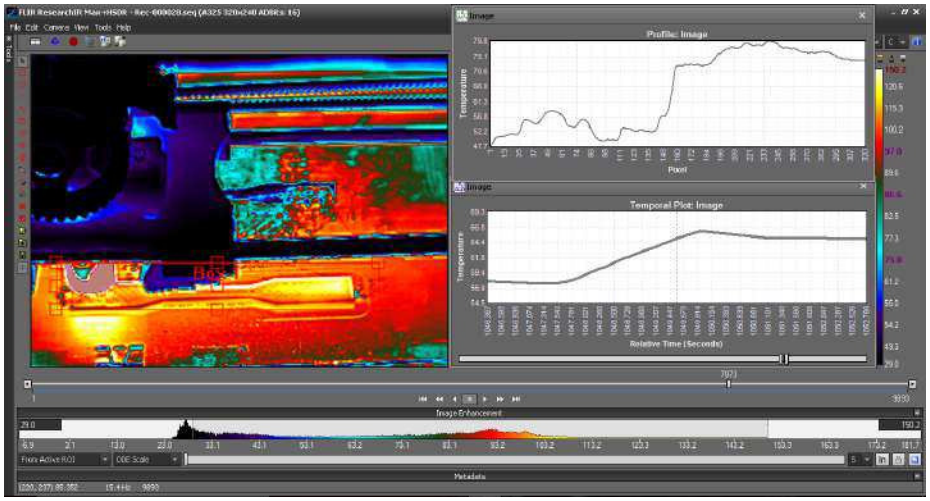

Figure 4.47. Thermal evolution and plot for specimen B4 layer 32.

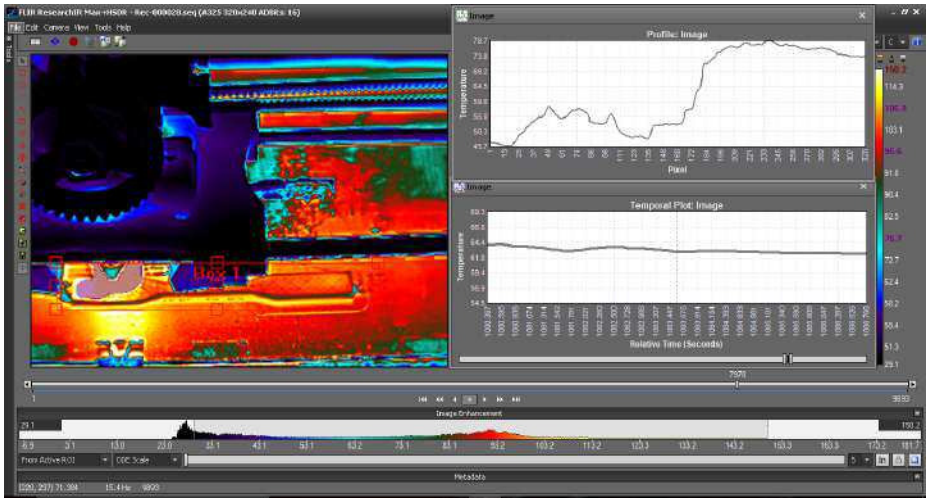

Figure 4.48. Thermal evolution and plot for specimen B4 layer 33.

Fig. 4.49, shows the Research IR Max software user interface for the in-situ monitoring of specimen B4 layer 34 of 35 layers. At this stage of the build process the specimen is at the final stage of completion. As earlier stated, the infra-red image of the build process showing material; deposition and the building of the part in successive layers is shown on the GUI left. The temperature profile on the GUI top right for these layers show the trend discussed and referred to in Fig. 4.26a

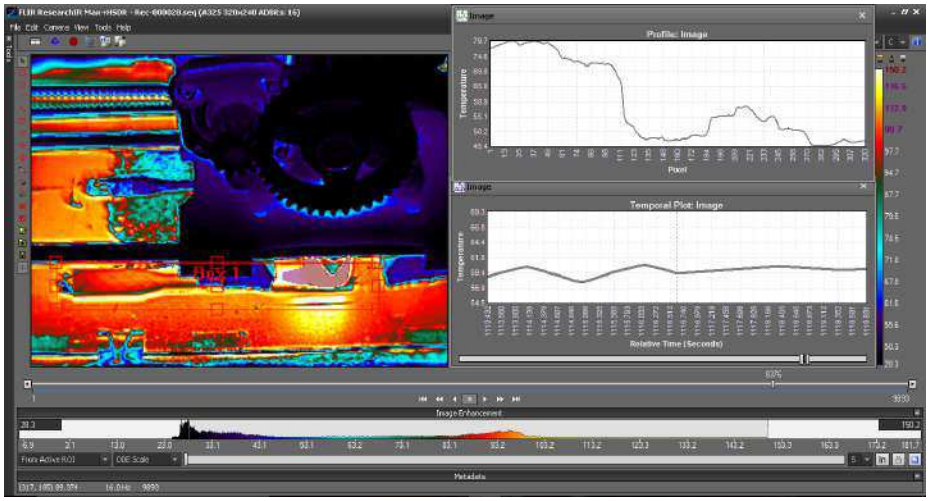

Figure 4.49. Thermal evolution and plot for specimen B4 layer 34.

Here, average temperature retrieved from the temperature profile plot in the ROI column of pixels is initially high, then gradually reduces in magnitude. This implies that the material deposition pattern is from the geometric origin of layer being printed and flowing along entire length of the specimen to the layers geometric endpoint. The evenness of the specimen temporal plot is more pronounced at this stage.

Fig. 4.50, shows the Research IR Max software user interface for the in-situ monitoring of specimen B4 final layer. At this stage of the build process the specimen is complete. The infra-red image of the build process showing material deposition and the building of the part in successive layers is shown on the GUI left. The temperature profile on the GUI top right for these layers show the trend discussed and referred to in Fig. 4.26b.

In this case, average temperature retrieved from the temperature profile plot in ROI column of pixels is initially low, then gradually increases in magnitude. Here the material deposition pattern is from the geometric endpoint of layer being printed and retraced along entire length of the specimen to the geometric origin of the layer being printed. The temporal plot indicates even distribution of temperature within the interacting regions.

The combination of the layer wise temperature profile plot and temporal plot presented and discussed in Fig. 4.27 - 4.50 provide insights for specimens fabricated in x-axis

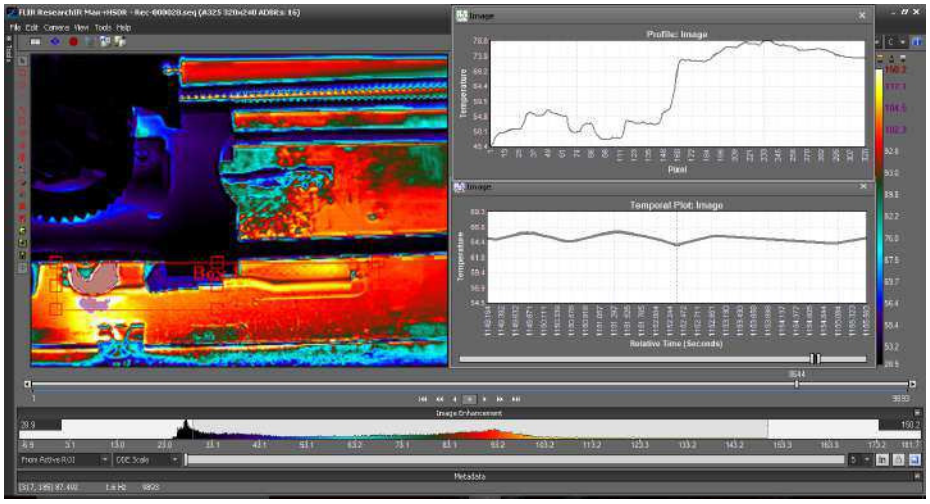

Figure 4.50. Thermal evolution and plot for specimen B4 layer 35.

orientation. The thermal trend through the evolution of the specimen seen in the thermal profile plot suggests a low uniformity in temperature changes between the earlier layers. In layer 1, the thermal profile shows the temperature distributed across the surface with the range of 42.7 °C 79.1°C but in the temporal plot has a range between 54.5°C 65.1°C. At the mid layer (layer 17) these values are at temperature distributed across the surface with the range of 44.5 °C 78.7°C but in the temporal plot has a range between 60.8°C 62.9°C. Finally at the final layer (layer 35), the values are at temperature distributed across the surface with the range of 45.4 °C 78.8°C but in the temporal plot has a range between 64.4°C 66.8°C.

4.2.3 Thermography Results from the Specimens Fabricated on the AirWolf 3-D Printer in the y-axis Orientation

The specimens printed in the y-axis orientation required 59 layers to be built. Fig. 4.51 - 4.72, show the layer wise thermal evolution of specimen B5. The thermal profile plot provides information on the part build temperature with respect to the distribution of heat across the layer surface. The temporal plot provides information on the surface layer surface thermal distribution with respect to time elapsed. The nature of the generated

curves can be interpreted to determine part layer wise thermal evolution and the uniformity of heat in successive part built layers.

Fig. 4.51 - 4.53, show the Research IR Max software user interface for the in-situ monitoring of specimen B5 layer 1, 2 and 3 of 59 layers. As earlier stated, the infra-red image of the build process showing material deposition and the building of the part in successive layers is shown on the GUI left. The temperature profile on the GUI top right shows the trend discussed and referred to in Fig. 4.26c of Section 4.2.1 .

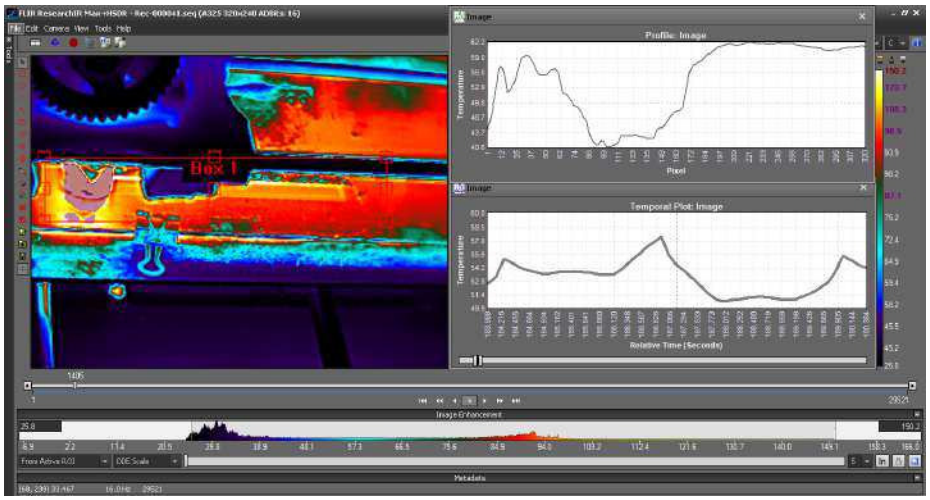

Figure 4.51. Thermal evolution and plot for specimen B5 layer 01.

The temperature profile plot shows that, average temperature retrieved from the ROI column of pixels is initially high and although gradually reducing in magnitude, begins again to gradually increase in magnitude. Material was deposited from the geometric origin or endpoint of layer being printed. Then continued to a point along the length of the specimen layer being printed. The printer nozzle then skipped to the opposite end of that layer and began to deposit material while returning to the skip-point. The temporal plot show significant irregularity at this early stage in the build process.

Fig. 4.54 , 4.55 and 4.56 present specimen B5 layer 4, 5 and 6 of 59 layers. Similar temperature profile plots to the preceding layers are observed. As earlier stated, the infra-red image of the build process showing material deposition and the building of the

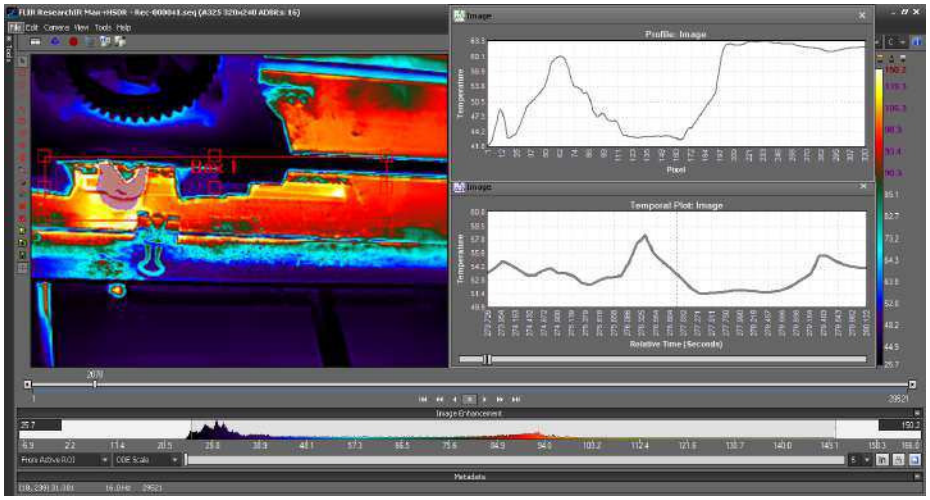

Figure 4.52. Thermal evolution and plot for specimen B5 layer 02.

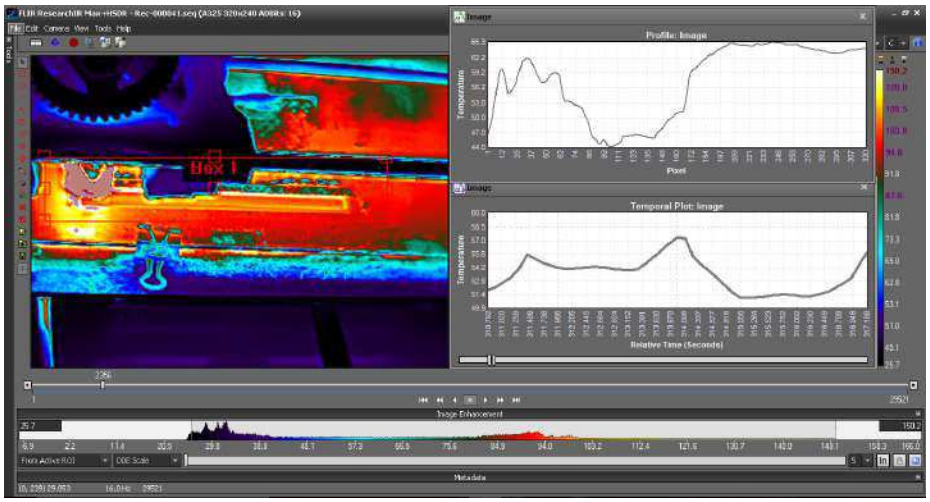

Figure 4.53. Thermal evolution and plot for specimen B5 layer 03.

part in successive layers is shown on the GUI left. The temperature profile on the GUI top right shows the trend referred to in Fig. 4.26c.

Here, average temperature retrieved from the ROI column of pixels is initially high and although gradually reducing in magnitude; begins again to gradually increase in magnitude. Material was deposited from the geometric origin or endpoint of layer being printed. Then continued to a point along the length of the specimen layer being printed. The printer nozzle then skipped to the opposite end of that layer and began to deposit material while

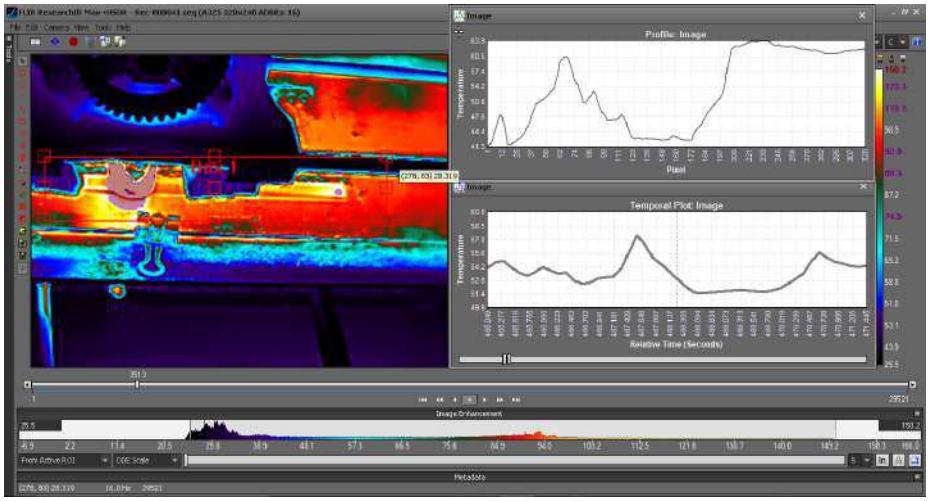

Figure 4.54. Thermal evolution and plot for specimen B5 layer 04.

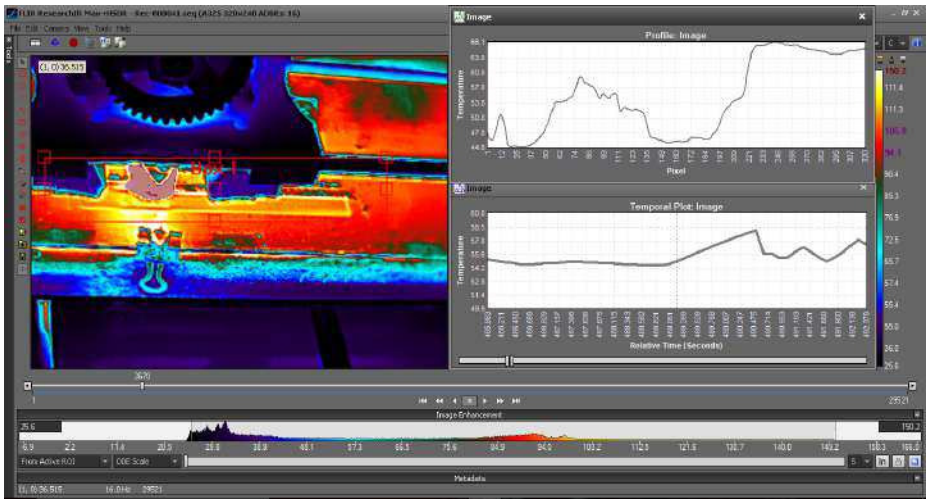

Figure 4.55. Thermal evolution and plot for specimen B5 layer 05.

returning to the skip-point. Although this is an early stage of the build process, the temporal plot shows eveness. This indicates uniform distribution of temperature between the interacting layers. The printing axis could be the factor influencing this.

Specimen B5 layer 7, 8 and 9 of 59 layers are shown in Fig. 4.57, 4.58 and 4.59. These layers possess similar temperature profile plots to the preceding layers when observed. As earlier stated, the infra-red image of the build process showing material deposition and

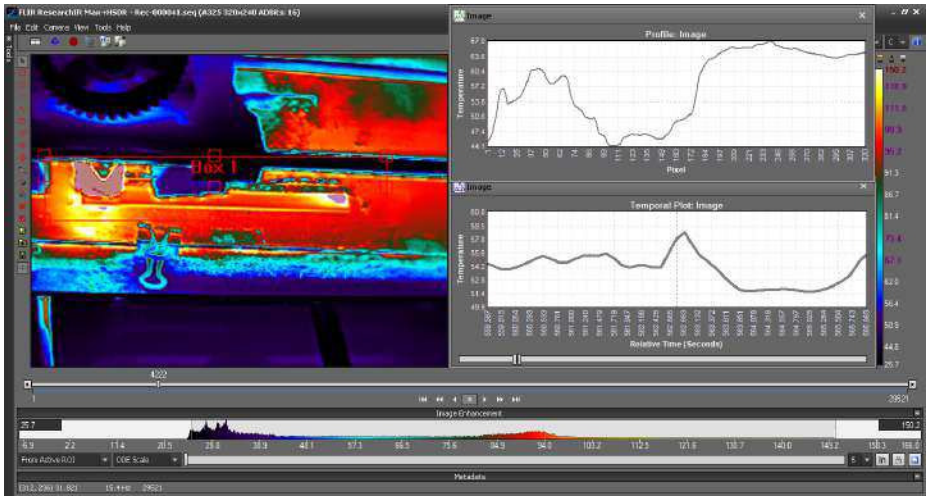

Figure 4.56. Thermal evolution and plot for specimen B5 layer 06.

the building of the part in successive layers is shown on the GUI left. The temperature profile on the GUI top right shows the trend referred to in Fig. 4.26c.

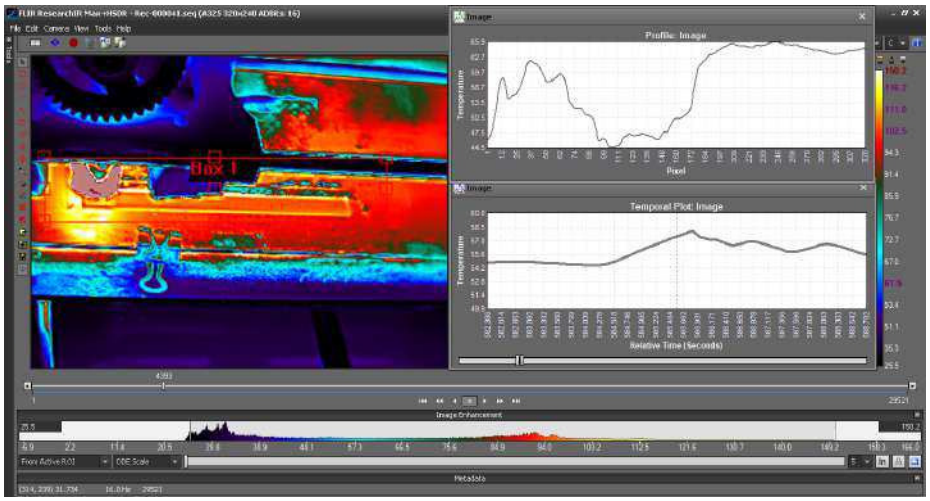

Figure 4.57. Thermal evolution and plot for specimen B5 layer 07.

The average temperature retrieved from the ROI column of pixels is initially high and although gradually reducing in magnitude; begins again to gradually increase in magnitude. Material was deposited from the geometric origin or endpoint of layer being printed. Then continued to a point along the length of the specimen layer being printed. The printer

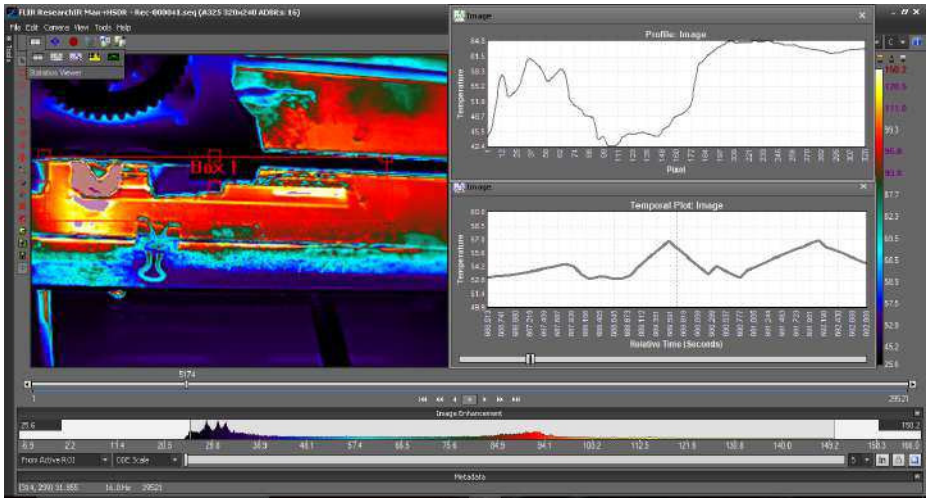

Figure 4.58. Thermal evolution and plot for specimen B5 layer 08.

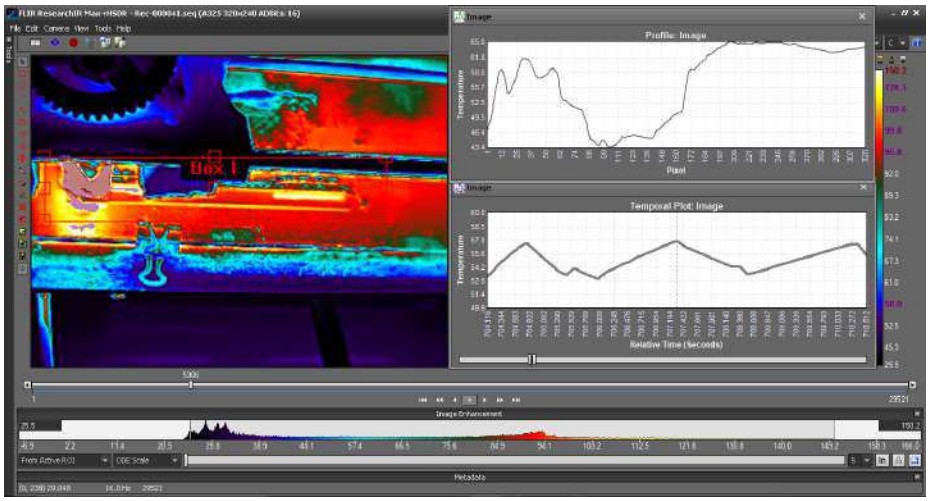

Figure 4.59. Thermal evolution and plot for specimen B5 layer 09.

nozzle then skipped to the opposite end of that layer and began to deposit material while returning to the skip-point. The temporal plots in these figures show irregularity. This is attributed to being in the early stage of the build process.

Specimen B5 layer 10 of 59 layers is presented in Fig. 4.60. The infra-red image of the build process showing material deposition and the building of the part in successive layers is shown on the GUI left. The temperature profile on the GUI top right shows the some similarity trend referred to in Fig. 4.26c.

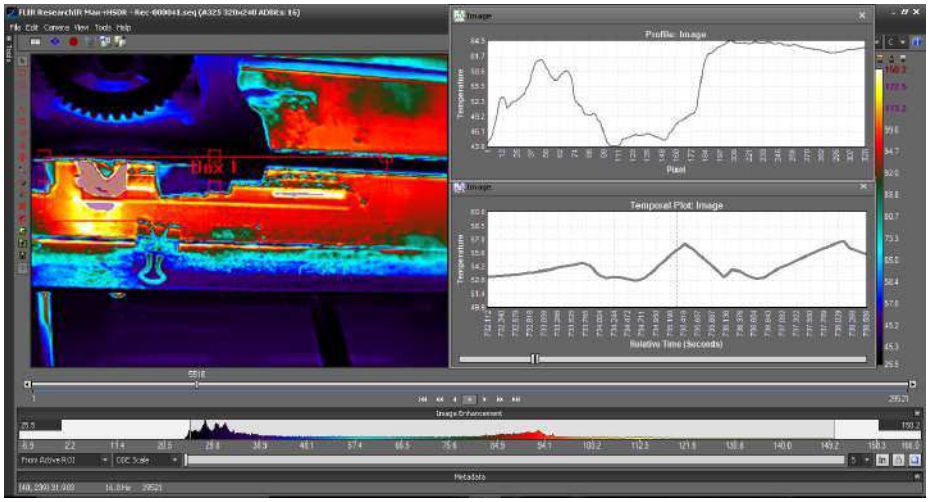

Figure 4.60. Thermal evolution and plot for specimen B5 layer 10.

Average temperature retrieved from the temperature profile plot in ROI column of pixels is initially low; then gradually increases in magnitude. Here the material deposition pattern is from the geometric endpoint of layer being printed and retraced along entire length of the specimen to the geometric origin of the layer being printed. The temporal plot still shows fluctuations at this stage.

Fig. 4.61 and 4.62 show the Research IR Max software user interface for the in-situ monitoring of specimen B5 layers 28 and 29. As earlier stated, the infra-red image of the build process showing material deposition and the building of the part in successive layers is shown on the GUI left. The temperature profile on the GUI top right shows a trend slightly similar to that referred to in Fig. 4.26c.

The temperature profile plot shows that, average temperature retrieved from the ROI column of pixels is initially high and although gradually reducing in magnitude; begins again to gradually increase in magnitude. Material was deposited from the geometric origin or endpoint of layer being printed. Then continued to a point along the length of the specimen layer being printed. The printer nozzle then skipped to the opposite end of that layer and began to deposit material while returning to the skip-point. At this stage the specimen is at the mid-point of completion; the temporal plot shows expected uniformity.

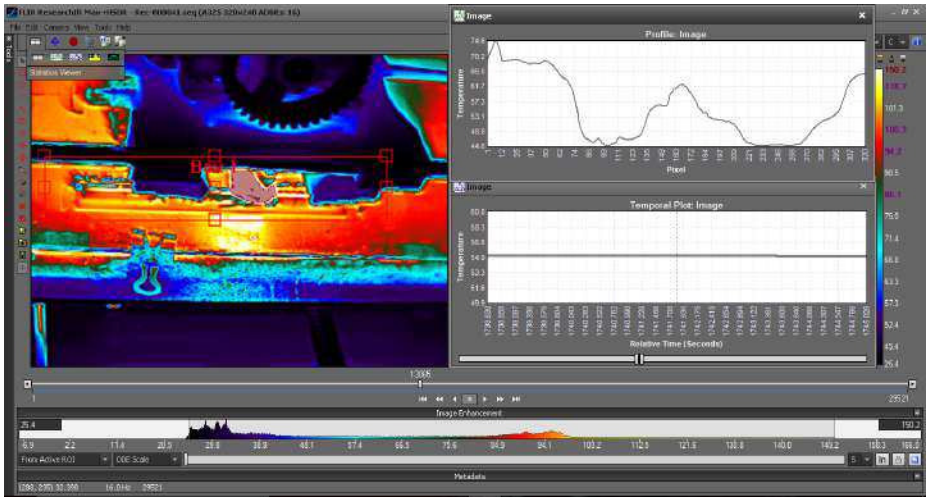

Figure 4.61. Thermal evolution and plot for specimen B5 layer 28.

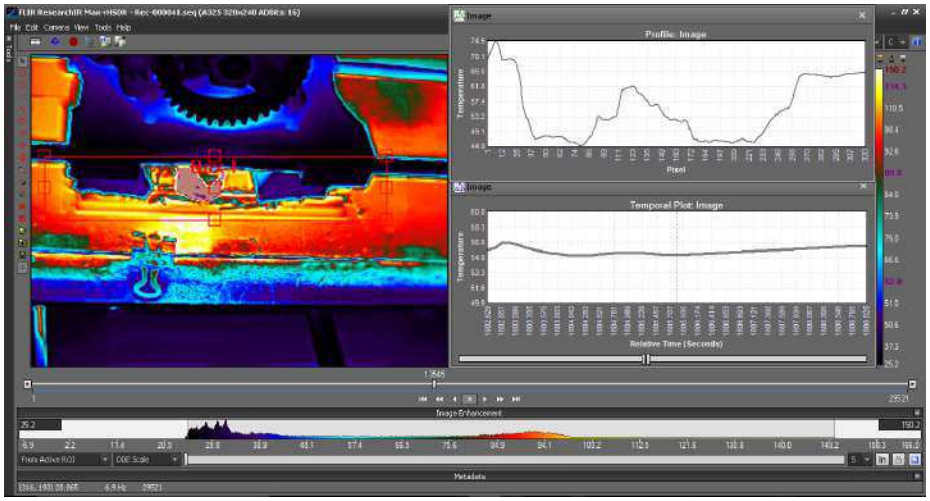

Figure 4.62. Thermal evolution and plot for specimen B5 layer 29.

Fig. 4.63 and 4.64 , are similar to the just discussed layers. The Research IR Max software user interface for the in-situ monitoring of specimen B4 layers 30 and 31 of 59 layers. As earlier stated, the infra-red image of the build process showing material; deposition and the building of the part in successive layers is shown on the GUI left. The temperature profile on the GUI top right for these layers show the trend referred to in Fig. 4.26c.

The temperature profile plot shows that, average temperature retrieved from the ROI column of pixels is initially high and although gradually reducing in magnitude; begins

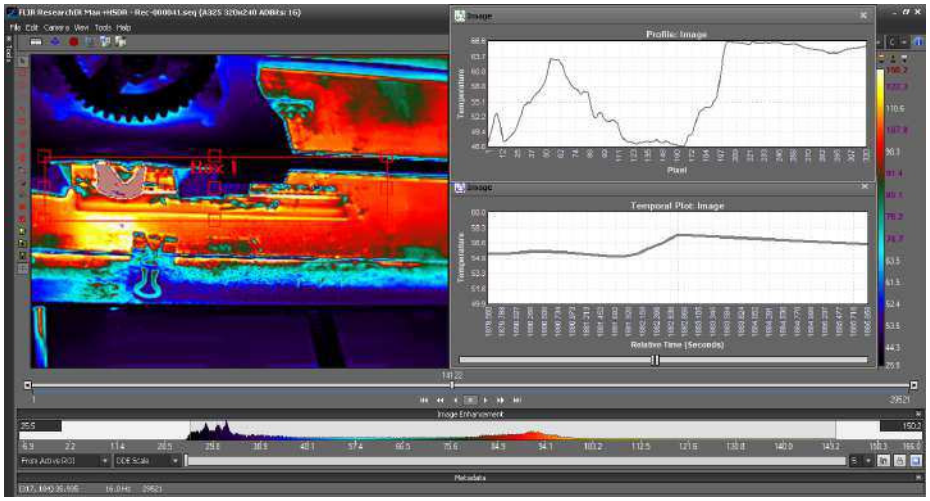

Figure 4.63. Thermal evolution and plot for specimen B5 layer 30.

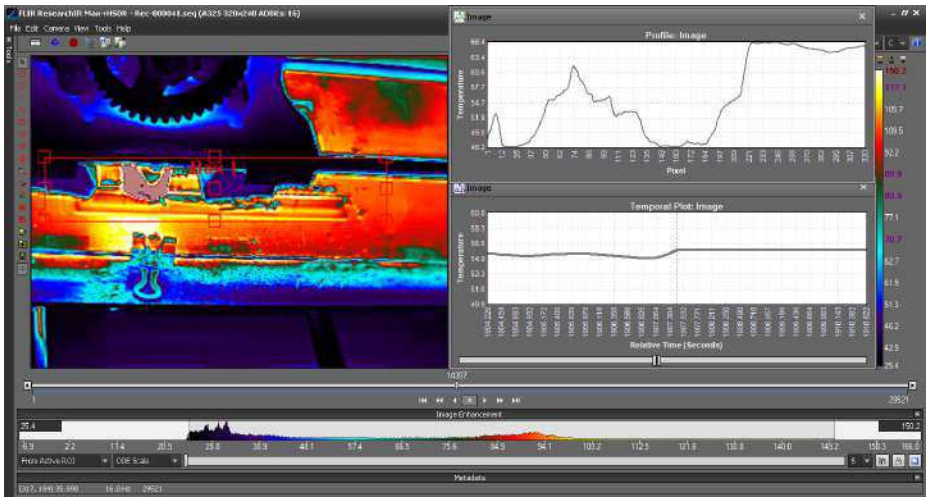

Figure 4.64. Thermal evolution and plot for specimen B5 layer 31.

again to gradually increase in magnitude. Material was deposited from the geometric origin or endpoint of layer being printed. Then continued to a point along the length of the specimen layer being printed. The printer nozzle then skipped to the opposite end of that layer and began to deposit material while returning to the skip-point. The temporal plot shows expected uniformity.

Fig. 4.65 and 4.66 show the Research IR Max software user interface for the in-situ monitoring of specimen B5 layers 32 and 33. As earlier stated, the infra-red image of the

build process showing material deposition and the building of the part in successive layers is shown on the GUI left. The temperature profile on the GUI top right shows the trend referred to in Fig. 4.26a.

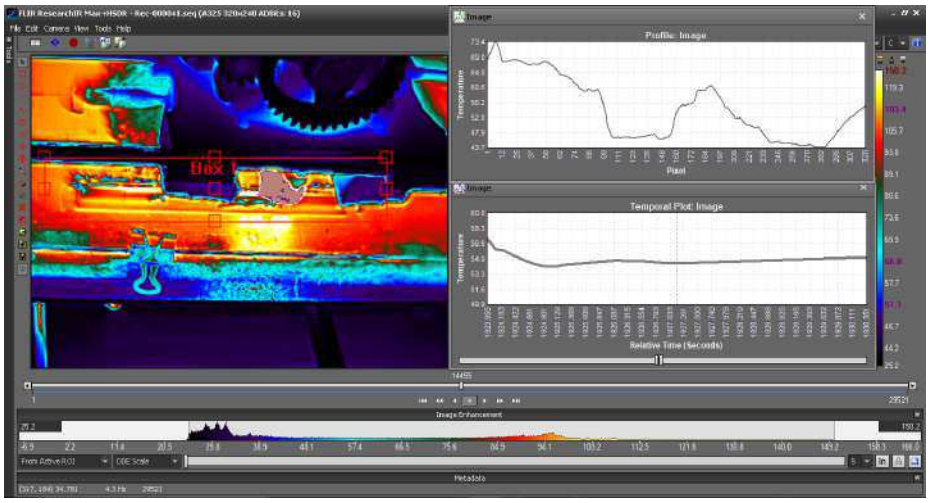

Figure 4.65. Thermal evolution and plot for specimen B5 layer 32.

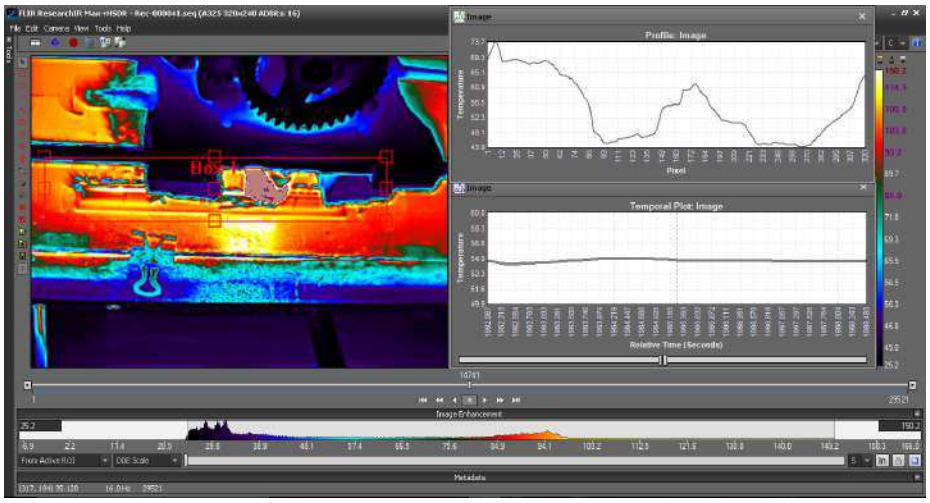

Figure 4.66. Thermal evolution and plot for specimen B5 layer 33.

Here, average temperature retrieved from the temperature profile plot in the ROI column of pixels is initially high, then gradually reduces in magnitude. This implies that the material deposition pattern is from the geometric origin of layer being printed and flowing along entire

length of the specimen to the layers geometric endpoint. At this stage in the build process the specimen is over half completed and the temporal plots show significant evenness.

Fig. 4.67, 4.68 and 4.69 show the Research IR Max software user interface for the in-situ monitoring of specimen B5 layers 54 - 56. As earlier stated, the infra-red image of the build process showing material deposition and the building of the part in successive layers is shown on the GUI left. The temperature profile on the GUI top right shows the trend referred to in Fig. 4.26c.

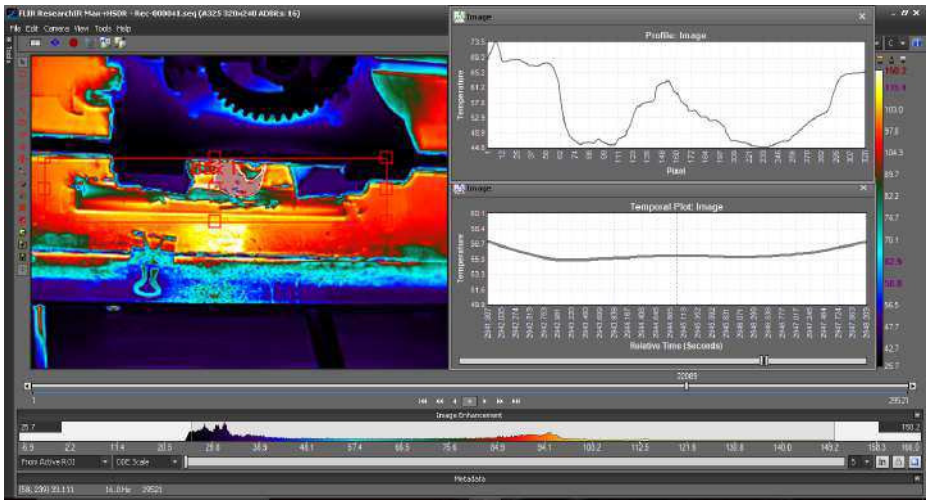

Figure 4.67. Thermal evolution and plot for specimen B5 layer 54.

The temperature profile plots show that, average temperature retrieved from the ROI column of pixels is initially high and although gradually reducing in magnitude; begins again to gradually increase in magnitude. Material was deposited from the geometric origin or endpoint of layer being printed. Then continued to a point along the length of the specimen layer being printed. The printer nozzle then skipped to the opposite end of that layer and began to deposit material while returning to the skip-point. The specimen build process is at the final stages and the temporal plots are regular and indicate uniform distribution of temperature between the interacting regions.

Fig. 4.70 and 4.71 show the Research IR Max software user interface for the in-situ monitoring of specimen B5 layers 57 and 58. As earlier stated, the infra-red image of the

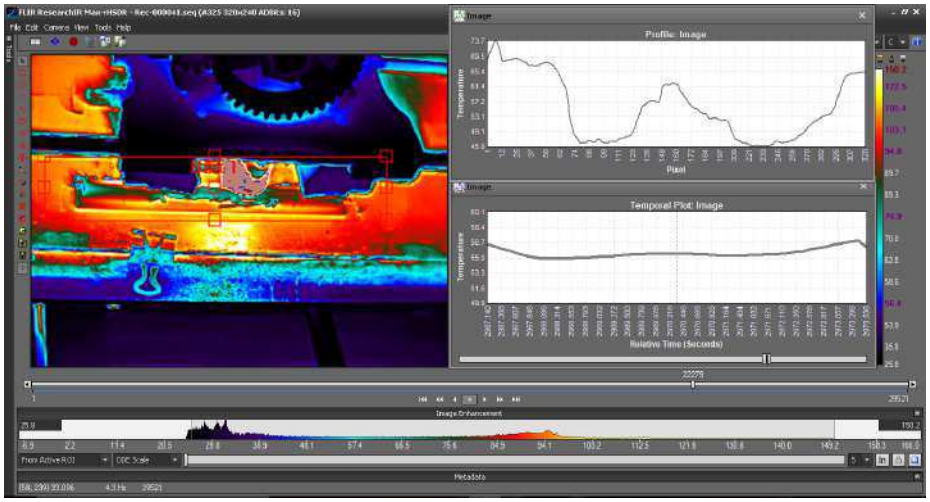

Figure 4.68. Thermal evolution and plot for specimen B5 layer 55.

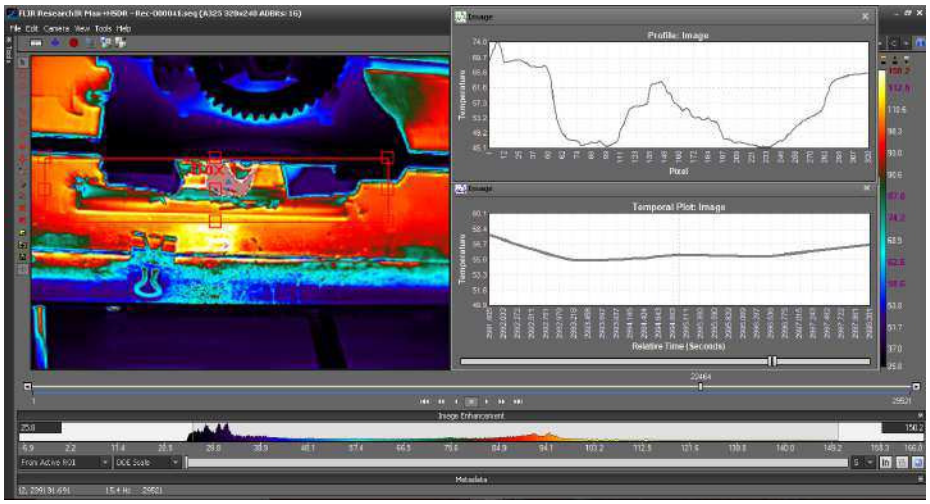

Figure 4.69. Thermal evolution and plot for specimen B5 layer 56.

build process showing material deposition and the building of the part in successive layers is shown on the GUI left. The temperature profile on the GUI top right shows the trend referred to in Fig. 4.26c.

The temperature profile plots show that, average temperature retrieved from the ROI column of pixels is initially high and although gradually reducing in magnitude; begins again to gradually increase in magnitude. Material was deposited from the geometric

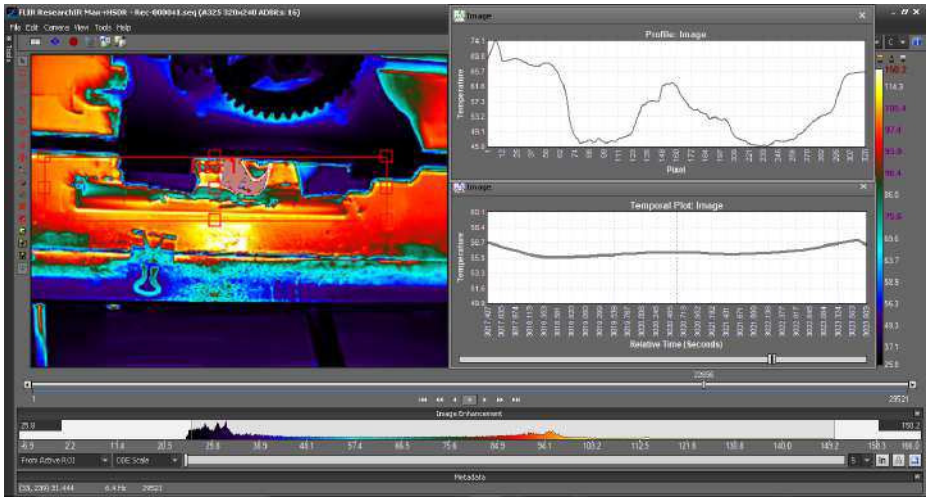

Figure 4.70. Thermal evolution and plot for specimen B5 layer 57.

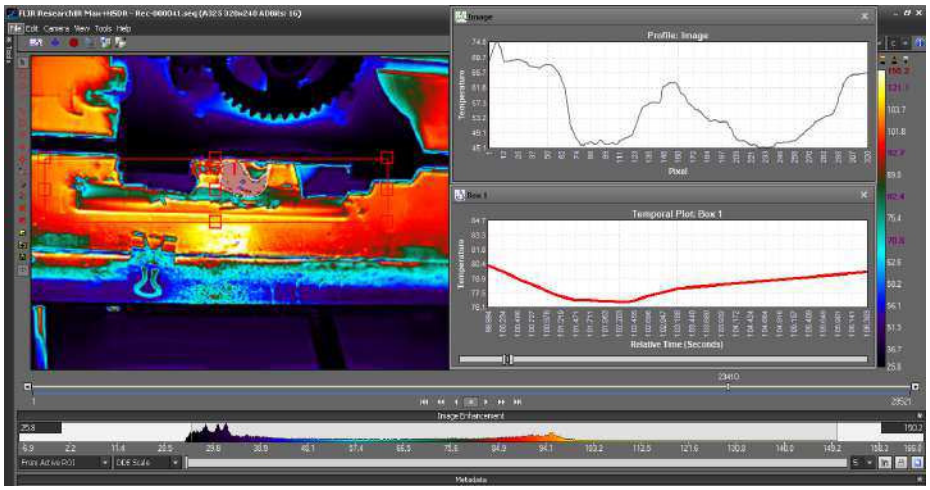

Figure 4.71. Thermal evolution and plot for specimen B5 layer 58.

origin or endpoint of layer being printed. Then continued to a point along the length of the specimen layer being printed. The printer nozzle then skipped to the opposite end of that layer and began to deposit material while returning to the skip-point. The specimen build process is at the final layer and the temporal plots are regular and indicate uniform distribution of temperature between the interacting regions.

Fig. 4.72 shows the Research IR Max software user interface for the in-situ monitoring of specimen B5 layers 59. As earlier stated, the infra-red image of the build process showing

material deposition and the building of the part in successive layers is shown on the GUI left. The temperature profile on the GUI top right shows the trend referred to in Fig. 4.26b.

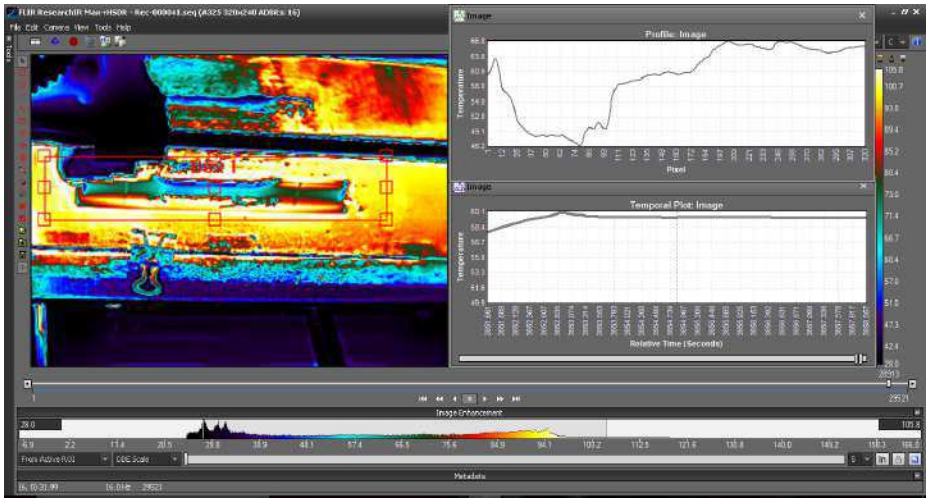

Figure 4.72. Thermal evolution and plot for specimen B5 layer 59.

In this case, average temperature retrieved from the temperature profile plot in ROI column of pixels is initially low, then gradually increases in magnitude. Here the material deposition pattern is from the geometric endpoint of layer being printed and retraced along entire length of the specimen to the geometric origin of the layer being printed.

The combination of the layer wise thermal profile plot and temporal plot (Fig. 4.51 - 4.72) provide insights for specimens fabricated in y-axis orientation. The thermal trend through the evolution of the specimen seen in the thermal profile plot suggests uniformity in temperature changes between the layers. In layer 1; the thermal profile shows the temperature distributed across the surface with the range of 43.7 °C 62.2 °C and in the temporal plot a range between 52.8 °C 57.0 °C. At the mid layer (layer 29) these values are at temperature distributed across the surface with the range of 66.1 °C 70.1 °C and in the temporal plot a range between 54.9 °C 56.6 °C. Finally at the final layer (layer 59), the values are at temperature distributed across the surface with the range of 60.9 °C 66.6 °C and in the temporal plot a range between 58.4 °C 60.1 °C. The narrow range in these values could be attributed to the positioning of the specimen in the y-axis orientation.

4.2.4 Thermography Results from the Specimens Fabricated on the AirWolf 3-D Printer in the z-axis Orientation

The specimens printed in the z-axis orientation required 1256 layers to be built. Fig. 4.73 - 4.95, show the layer wise thermal evolution of specimen B6. As discussed in section 4.2.1, the thermal profile plot provides information on the part build temperature with respect to the distribution of heat across the layer surface. The temporal plot provides information on the surface layer surface thermal distribution with respect to time elapsed. The nature of the generated curves can be interpreted to determine part layer wise thermal evolution and the uniformity of heat in successive part built layers.

Fig. 4.73 , 4.74 , 4.75 and 4.76 show the Research IR Max software user interface for the in-situ monitoring of specimen B6 layer 1, 10, 20 and 30 of 1256 layers. As earlier stated, the infra-red image of the build process showing material deposition and the building of the part in successive layers is shown on the GUI left. The temperature profile on the GUI top right shows the trend similar to the plot discussed in Fig. 4.26c of Section 4.2.1.

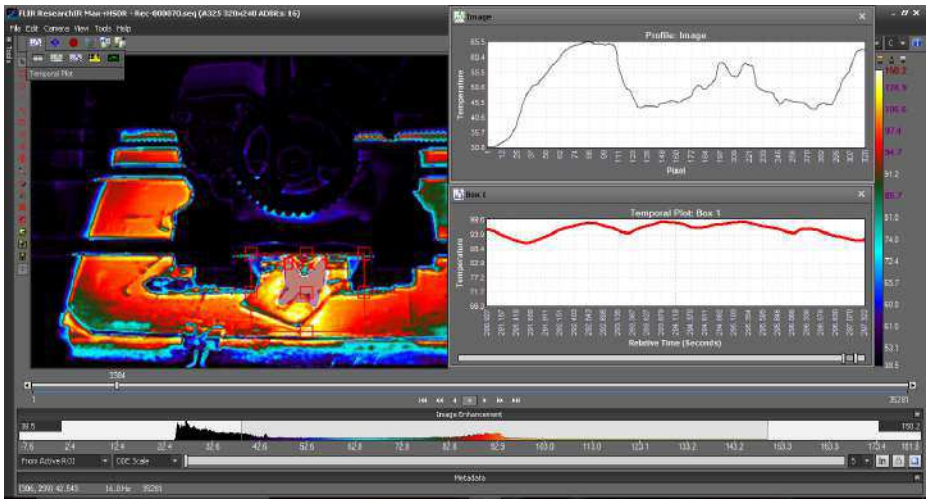

Figure 4.73. Thermal evolution and plot for specimen B6 layer 1.

The temperature profile plot shows that, average temperature retrieved from the ROI column of pixels is initially high and although gradually reducing in magnitude; begins again to gradually increase in magnitude. Material was deposited from the geometric

origin or endpoint of layer being printed. Then continued to a point along the length of the specimen layer being printed. The printer nozzle then skipped to the opposite end of that layer and began to deposit material while returning to the skip-point.The orientation of the specimen along the z-axis resulted in the significantly short layer lengths compared to the layer lengths in the x-axis and y-axis orientations.

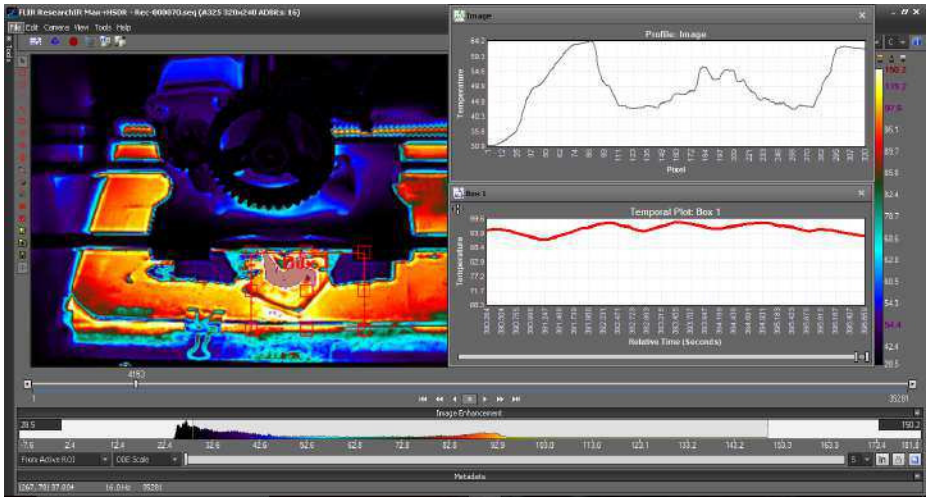

Figure 4.74. Thermal evolution and plot for specimen B6 layer 10.

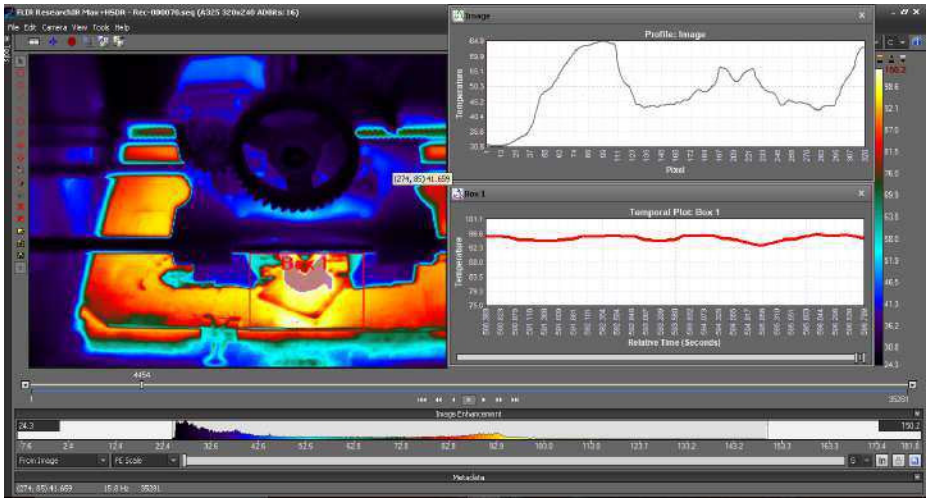

Figure 4.75. Thermal evolution and plot for specimen B6 layer 20.

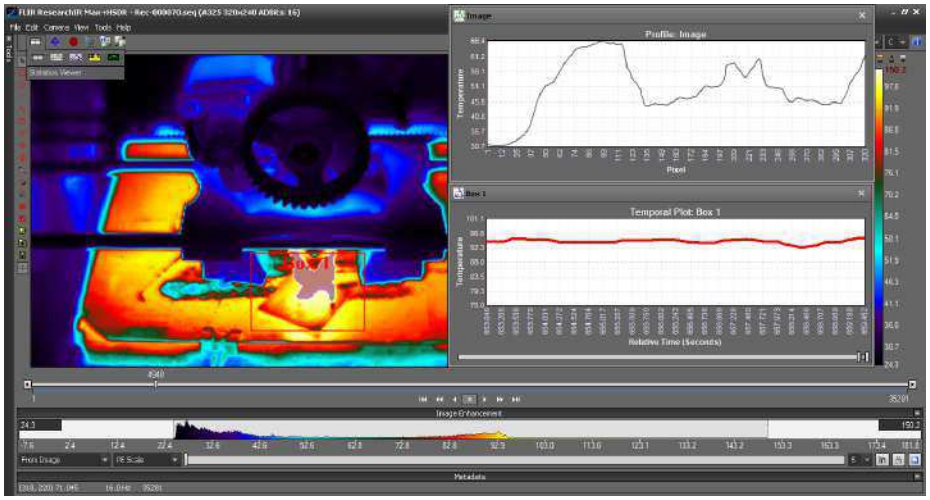

Figure 4.76. Thermal evolution and plot for specimen B6 layer 30.

The temperature profile plot shows that, average temperature retrieved from the ROI column of pixels is initially high and although gradually reducing in magnitude; begins again to gradually increase in magnitude. Material was deposited from the geometric origin or endpoint of layer being printed. Then continued to a point along the length of the specimen layer being printed. The printer nozzle then skipped to the opposite end of that layer and began to deposit material while returning to the skip-point. The orientation of the specimen along the z-axis resulted in the significantly short layer lengths compared to the layer lengths in the x-axis and y-axis orientations. The temporal plot indicate early uniform distribution of temperature between the interacting regions.

Fig. 4.77 and 4.78 show the Research IR Max software user interface for the in-situ monitoring of specimen B6 layers 40 and 50. As earlier stated, the infra-red image of the build process showing material deposition and the building of the part in successive layers is shown on the GUI left. The temperature profile on the GUI top right shows the trend referred to in Fig. 4.26a.

Here, average temperature retrieved from the temperature profile plot in the ROI column of pixels is low but rises steeply, then gradually reduces in magnitude. This implies that the material deposition pattern is from the geometric origin of layer being printed and

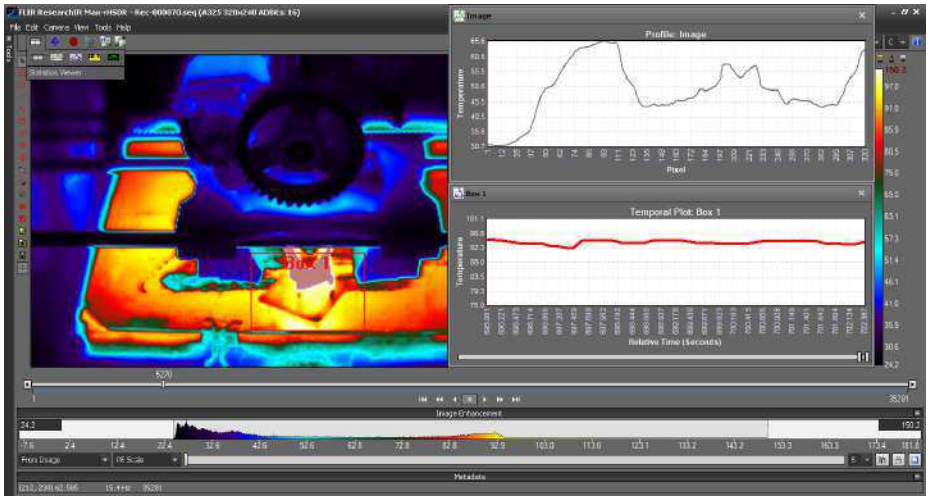

Figure 4.77. Thermal evolution and plot for specimen B6 layer 40.

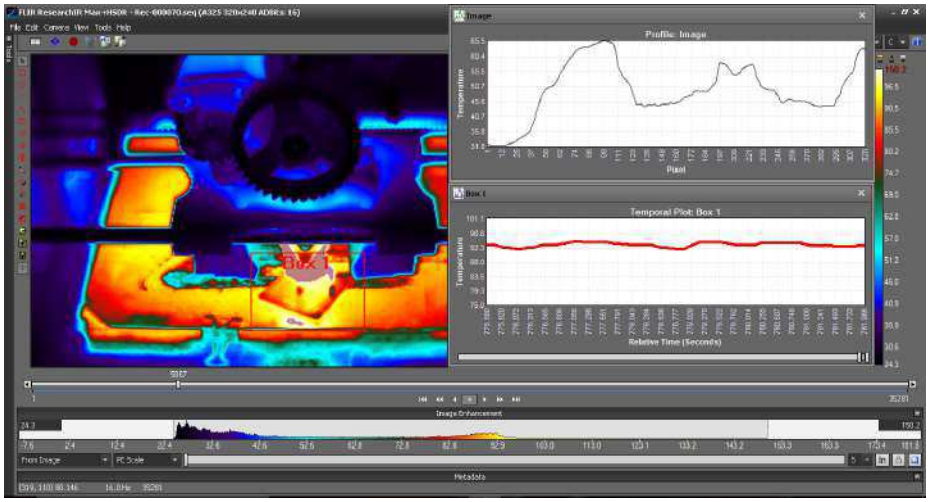

Figure 4.78. Thermal evolution and plot for specimen B6 layer 50.

flowing along entire length of the specimen to the layers geometric endpoint. The temporal plot indicates early uniform distribution of temperature between the interacting regions.

Fig. 4.79, 4.80 and 4.81 show the Research IR Max software user interface for the in-situ monitoring of specimen B6 layers 580, 600 and 620. As earlier stated, the infra-red image of the build process showing material deposition and the building of the part in successive layers is shown on the GUI left. The temperature profile on the GUI top right shows the trend referred to in Fig. 4.26a.

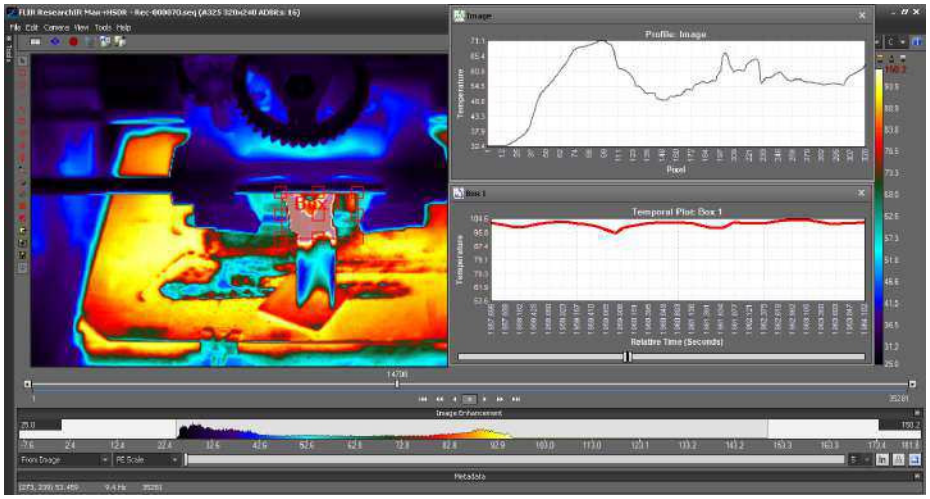

Figure 4.79. Thermal evolution and plot for specimen B6 layer 580.

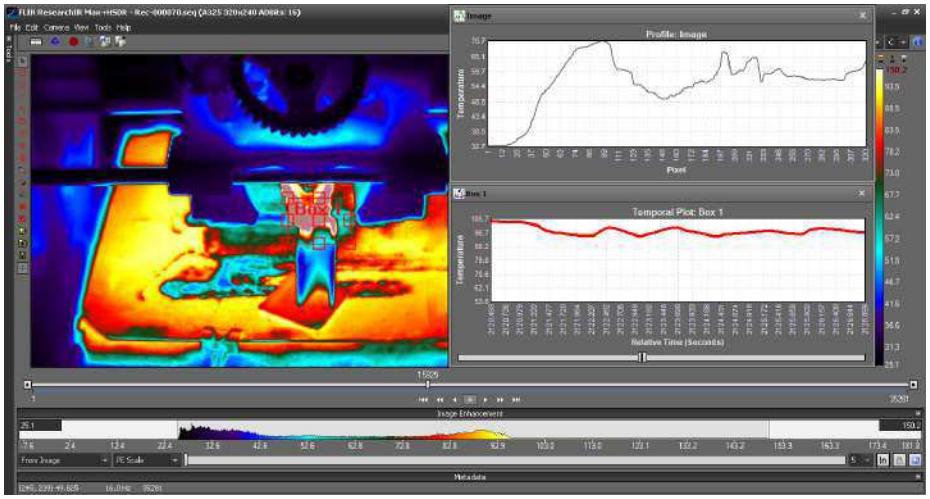

Figure 4.80. Thermal evolution and plot for specimen B6 layer 600.

Similar to the earlier layers, average temperature retrieved from the temperature profile plot in the ROI column of pixels is low but rises steeply. Then gradually reduces in magnitude. Implying that the material deposition pattern is from the geometric origin of layer being printed and flowing along entire length of the specimen to the layers geometric endpoint. The slight variation to this trend observed as the temperature gradually reduces to between 55 °C and 60 °C and remaining within this range. This variation is attributed to

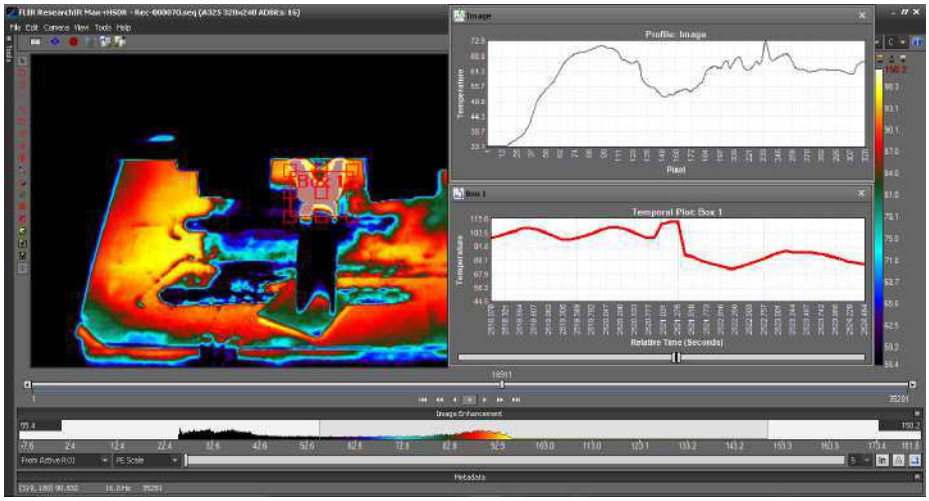

Figure 4.81. Thermal evolution and plot for specimen B6 layer 620.

the shorter layer lengths encountered in printing along the z-axis orientation. The temporal plot indicates early uniform distribution of temperature between the interacting regions.

Fig. 4.82, 4.83 and 4.84 show the Research IR Max software user interface for the in-situ monitoring of specimen B6 layers 640, 650 and 750. As earlier stated, the infra-red image of the build process showing material deposition and the building of the part in successive layers is shown on the GUI left. The temperature profile on the GUI top right shows the trend referred to in Fig. 4.26b

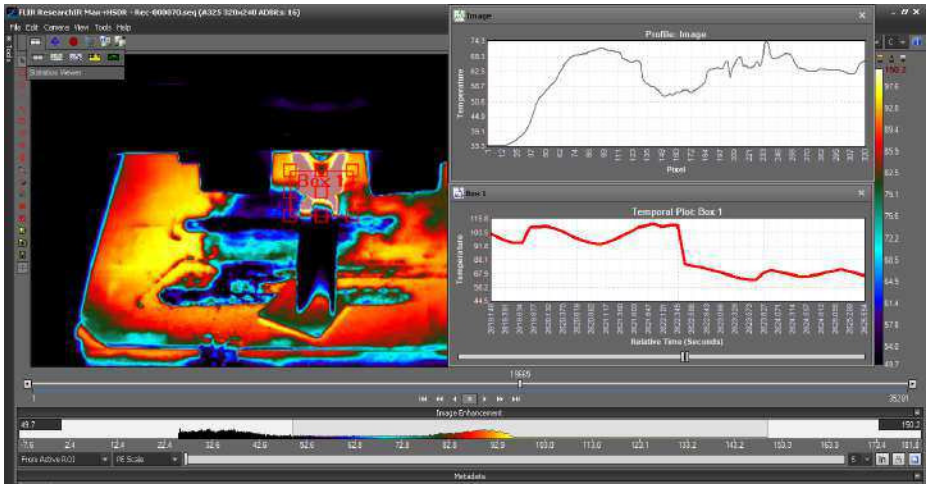

Figure 4.82. Thermal evolution and plot for specimen B6 layer 640.

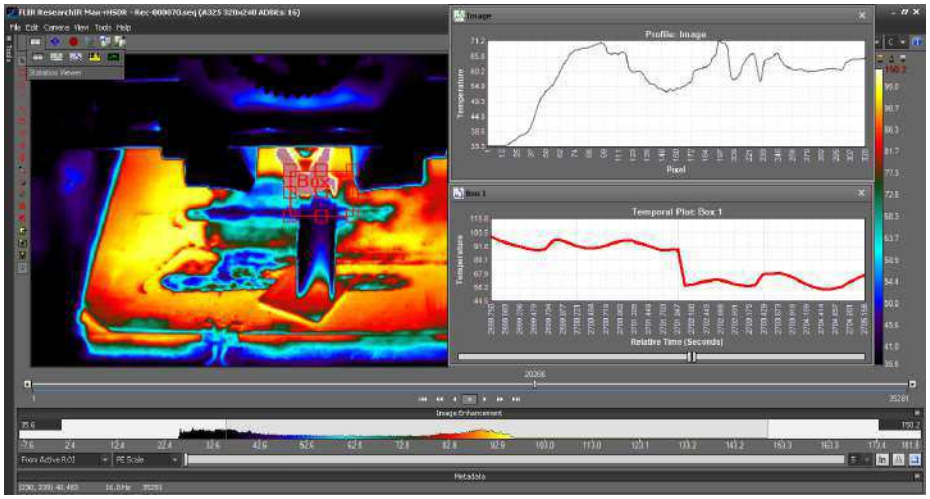

Figure 4.83. Thermal evolution and plot for specimen B6 layer 650.

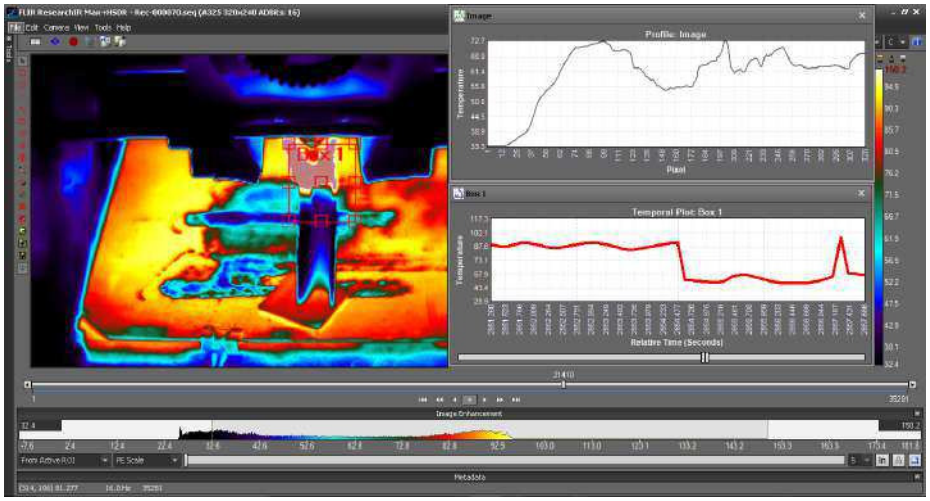

Figure 4.84. Thermal evolution and plot for specimen B6 layer 750.

These layers are also similar to the previously discussed layers. The earlier layers, average temperature retrieved from the temperature profile plot in the ROI column of pixels is low but rises steeply, then gradually reduces in magnitude. This implies that the material deposition pattern is from the geometric origin of layer being printed and flowing along entire length of the specimen to the layers geometric endpoint. The slight variation to this trend observed as the temperature gradually reduces to between 55 °and 60 °C

and remaining within this range. This variation is attributed to the shorter layer lengths encountered in printing along the z-axis orientation. The temporal plot indicates early uniform distribution of temperature between the interacting regions.

Fig. 4.85, 4.86 and 4.87 show the Research IR Max software user interface for the in-situ monitoring of specimen B6 layers 770, 790 and 810. As earlier stated, the infra-red image of the build process showing material deposition and the building of the part in successive layers is shown on the GUI left. The temperature profile on the GUI top right shows the trend referred to in Fig. 4.26a.

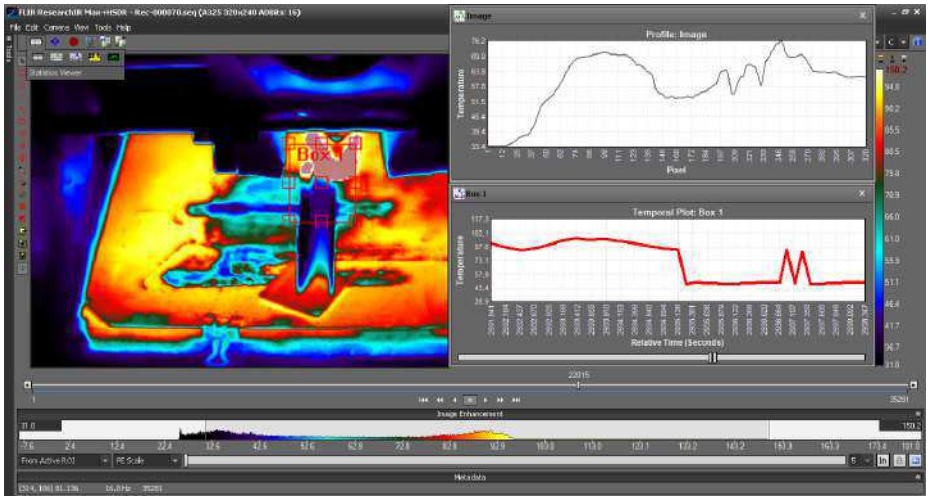

Figure 4.85. Thermal evolution and plot for specimen B6 layer 770.

These layers are also similar to the previously discussed layers. The average temperature retrieved from the temperature profile plot in the ROI column of pixels is low but rises steeply. Then gradually reduces in magnitude. Implying that the material deposition pattern is from the geometric origin of layer being printed and flowing along entire length of the specimen to the layers geometric endpoint. The slight variation to this trend observed as the temperature gradually reduces to between 56 °C and 68 °C and remaining within this range. This variation is attributed to the shorter layer lengths encountered in printing along the z-axis orientation. The temporal plot indicates early uniform distribution of temperature between the interacting regions.

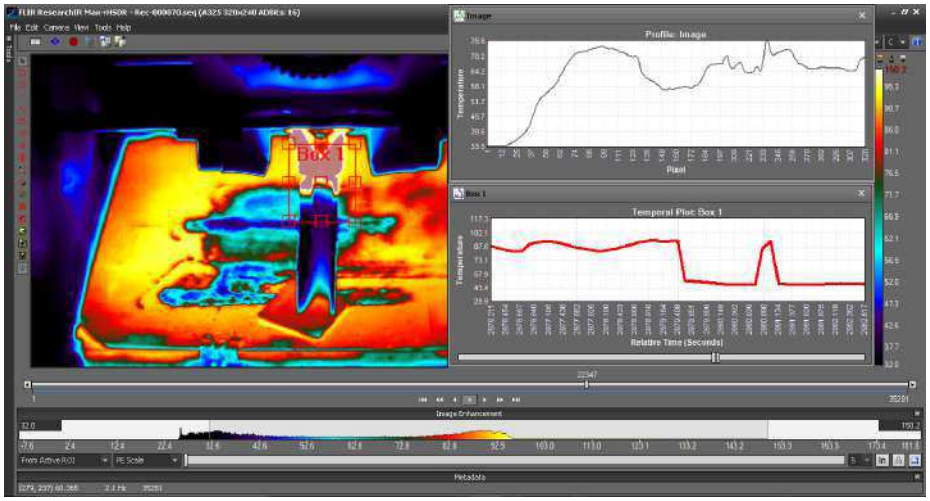

Figure 4.86. Thermal evolution and plot for specimen B6 layer 790.

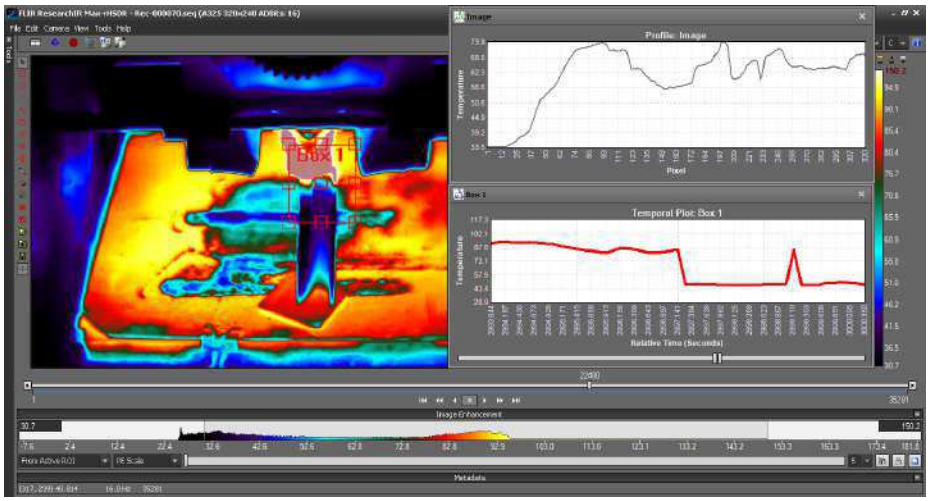

Figure 4.87. Thermal evolution and plot for specimen B6 layer 810.

Fig. 4.88, 4.89 and 4.90 show the Research IR Max software user interface for the in-situ monitoring of specimen B6 layers 850, 890 and 950. As earlier stated, the infra-red image of the build process showing material deposition and the building of the part in successive layers is shown on the GUI left. The temperature profile on the GUI top right shows the trend referred to in Fig. 4.26b.

Fig. 4.91, 4.92 and 4.93 show the Research IR Max software user interface for the in-situ monitoring of specimen B6 layers 990, 1050 and 1090. As earlier stated, the infra-red

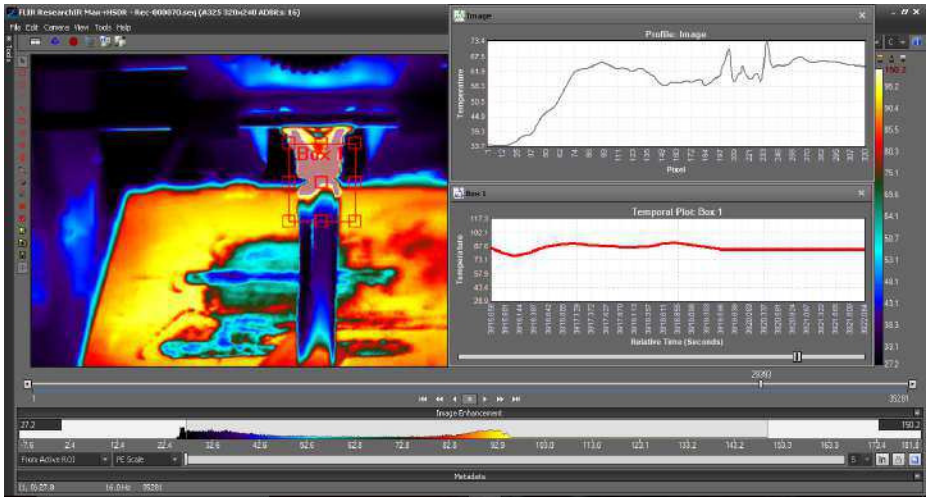

Figure 4.88. Thermal evolution and plot for specimen B6 layer 850.

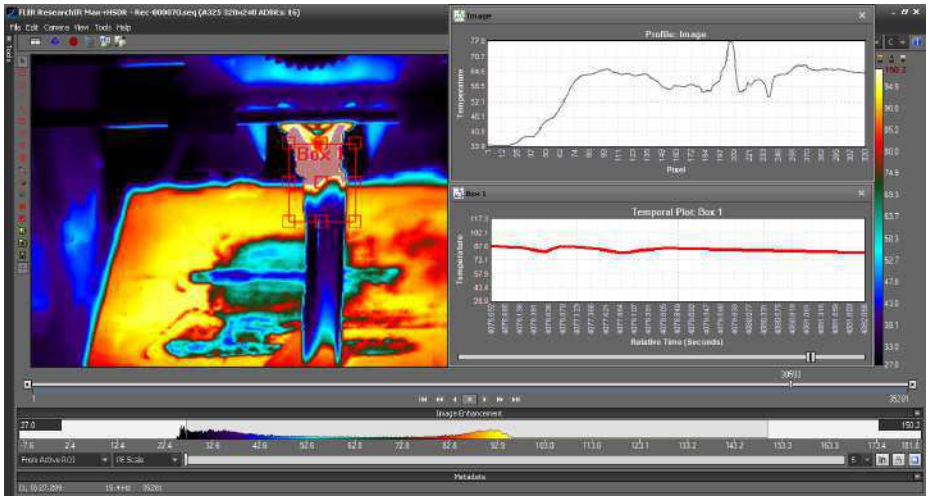

Figure 4.89. Thermal evolution and plot for specimen B6 layer 890.

image of the build process showing material deposition and the building of the part in successive layers is shown on the GUI left. The temperature profile on the GUI top right shows the trend referred to in Fig. 4.26b

These layers are also similar to the previously discussed layers. The earlier layers, average temperature retrieved from the temperature profile plot in the ROI column of pixels is low but rises steeply. Then gradually reduces in magnitude. Implying that the material deposition pattern is from the geometric origin of layer being printed and flowing

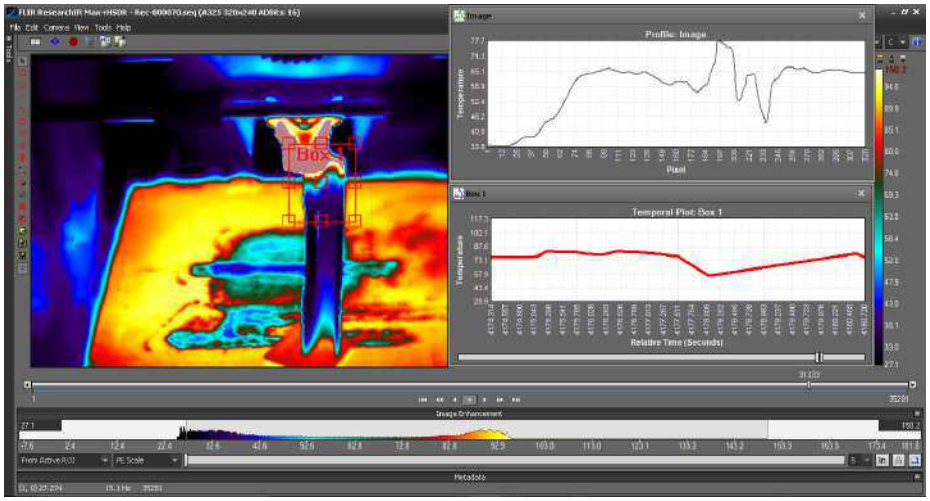

Figure 4.90. Thermal evolution and plot for specimen B6 layer 950.

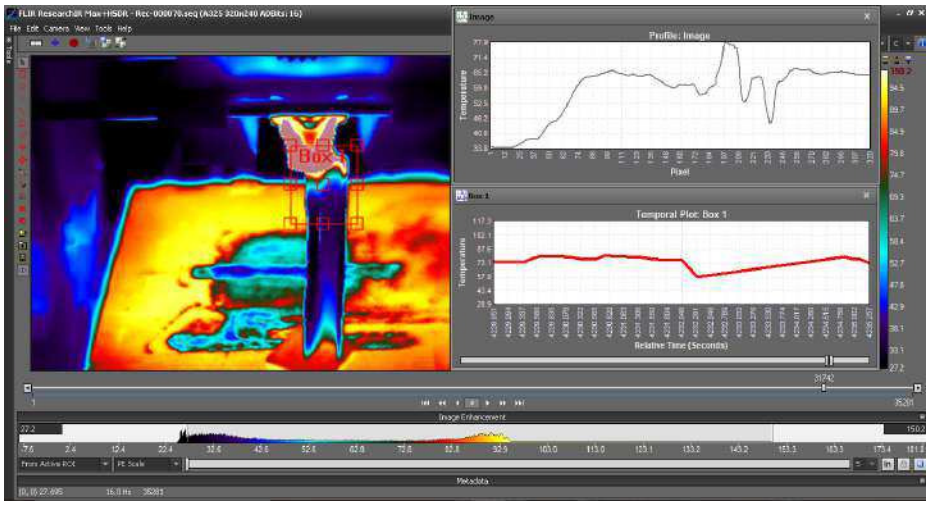

Figure 4.91. Thermal evolution and plot for specimen B6 layer 990.

along entire length of the specimen to the layers geometric endpoint. The slight variation to this trend observed as the temperature gradually reduces to between 60 °C and 65 °C and remaining within this range. This variation is attributed to the shorter layer lengths encountered in printing along the z-axis orientation. The temporal plot indicates early uniform distribution of temperature between the interacting regions.

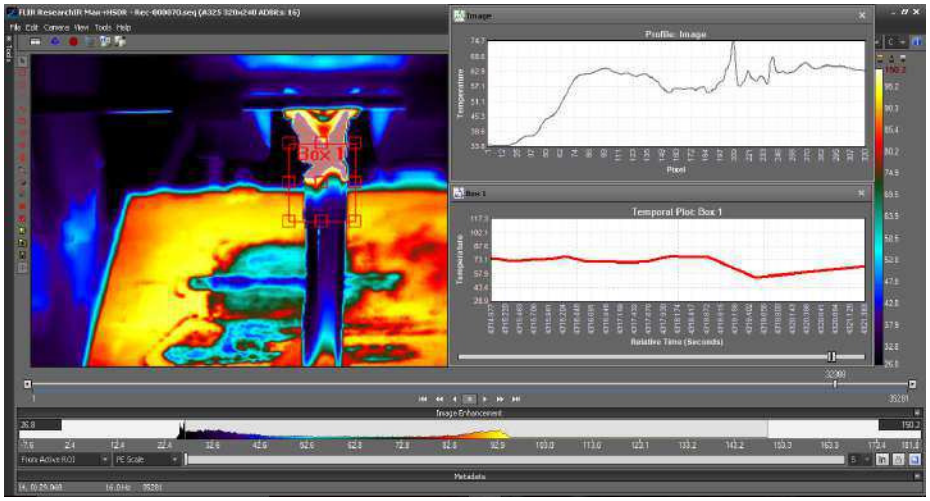

Figure 4.92. Thermal evolution and plot for specimen B6 layer 1050.

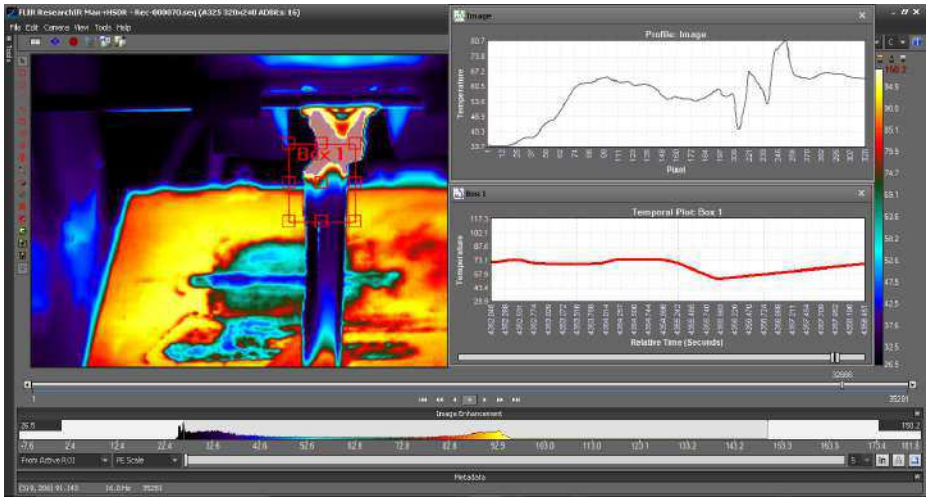

Figure 4.93. Thermal evolution and plot for specimen B6 layer 1090.

Fig. 4.94 and 4.95 show the Research IR Max software user interface for the in-situ monitoring of specimen B6 layers 1100 and the final layer 1256. As earlier stated, the infra-red image of the build process showing material deposition and the building of the part in successive layers is shown on the GUI left. The temperature profile on the GUI top right shows the trend referred to in Fig. 4.26b.

These layers are also similar to the previously discussed layers. The average temperature retrieved from the temperature profile plot in the ROI column of pixels is low but rises

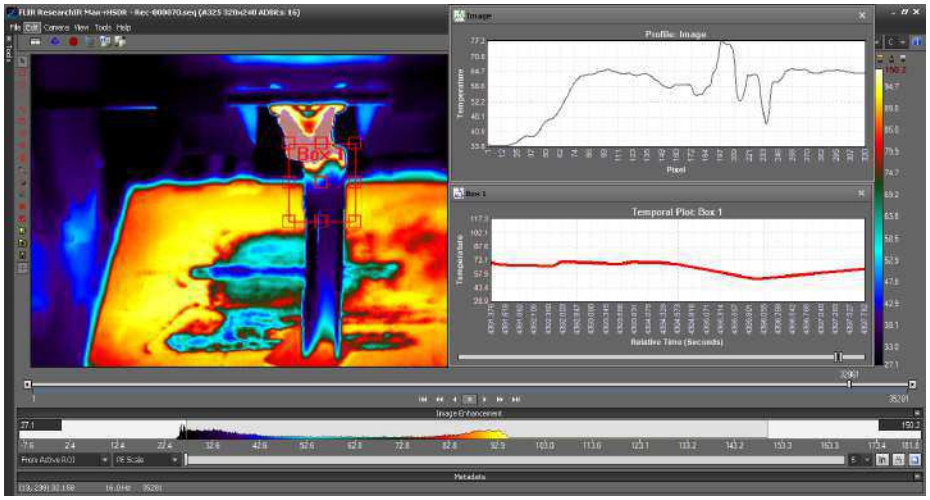

Figure 4.94. Thermal evolution and plot for specimen B6 layer 1100.

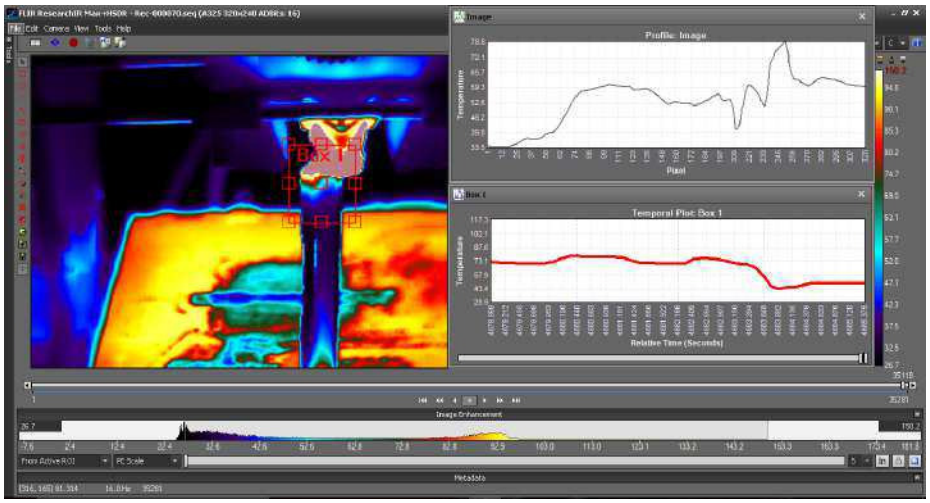

Figure 4.95. Thermal evolution and plot for specimen B6 layer 1256.

steeply, then gradually reduces in magnitude. This implies that the material deposition pattern is from the geometric origin of layer being printed and flowing along entire length of the specimen to the layers geometric endpoint. The slight variation to this trend observed as the temperature gradually reduces to between 59 °C and 64 °C and remaining within this range. This variation is attributed to the shorter layer lengths encountered in printing along the z-axis orientation. The temporal plot indicates early uniform distribution of temperature between the interacting regions.

The information from the part layers show intermittent wide and narrow temperature ranges as the part is built. Also while the thermal profile plot presents a wide range for the surface thermal distribution, the temporal plot presents a narrow temperature range. The combination of the layer wise thermal profile plot and temporal plot in Fig. 4.73 - 4.95 provide insights for specimens fabricated in z-axis orientation. The thermal trend through the evolution of the specimen seen in the thermal profile plot suggests uniformity in temperature en the layers. In layer 1, the thermal profile shows the temperature distributed across the surface with changes between the range of 30.8 °C 65.5 °C and in the temporal plot a range between of 94.0 °C 99.6 °C. At the mid layer (layer 640) these values are at temperature distributed across the surface with the range of 33.3 °C 74.3 °Cand in the temporal plot a range between 67.9 °C 103.5 °C. Finally at the final layer (layer 1256), the values are at temperature distributed across the surface with the range of 33.5 °C 78.8 °Cand in the temporal plot a range between 43.4 °C 73.1 °C.

4.2.5 Results from Mechanical Evaluation of Specimens Printed on the Air-Wolf 3-D Printer

The specimens printed in the x-axis orientation (B1, B4, B7, B10, B13, B16, B19, B22 and B25), tended to fracture at location close to the end at the neck region; as presented in Fig. 4.96.

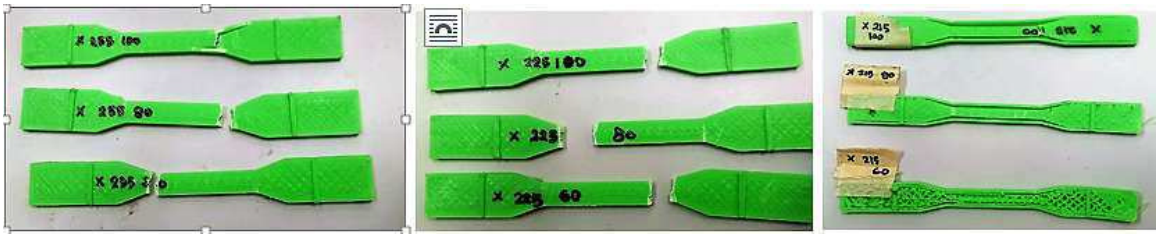

Figure 4.96. Specimen B1, B4, B7 (left), B10, B13, B16 (middle) and B19, B22, B25 (right) after evaluation on the Q test machine.

The specimens printed in the y-axis orientation (B2, B5, B8, B11, B14, B17, B20, B23 and B26) tended also to fracture at location close to the end at the neck region; as presented in Fig. 4.97.

Figure 4.97. Specimen B2, B5, B8 (left), B11, B14, B17 (middle) and B20, B23, B26 (right) after evaluation on the Q test machine.

However, the specimens printed in the z-axis orientation (B3, B6, B9, B12, B15, B18, B21, B24 and B27) tended to fracture at location closer to the mid region of the specimen as presented in Fig. 4.98.

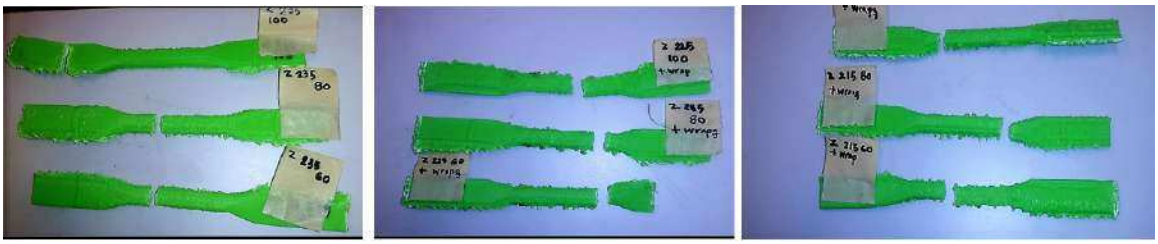

Figure 4.98. Specimen B3, B6, B9 (left), B12, B15, B18 (middle) and B21, B24, B27 (right) after evaluation on the Q test machine.

For specimens B1 to B27, printed on the AirWolf 3-D Printer along the x, y and z-axis orientation the stress-strain curves show the effect of the changing the printing parameters on the mechanical behavior of each specimen. Values of the modulus, yield strength and ultimate tensile strength of the specimens gotten from the tensile strength analysis are presented in Table 4.5 , 4.6 and 4.7 . While, Fig. 4.99 - 4.110 present the plots of the stress-strain curves for the specimens according to the print orientation.

Table 4.5.
Mechanical properties of specimens printed in the x-axis orientation on the AirWolf 3-D Printer

Specimen number	Modulus (ksi)	Yield strength (ksi)	Ultimate tensile strength (ksi)
B1	86.56865	0.1731	4.406
B4	70.38794	0.13329	3.062
B7	36.78899	0.07084	1.718
B10	88.24703	0.17853	4.045
B13	80.02544	0.1605	3.07
B16	151.4242	0.30314	5.351
B19	58.63878	0.11898	1.146
B22	100.5873	0.2017	3.462
B25	71.08216	0.1654	3.278

The plots for specimen B1, 4 and 7 shown in Fig. 4.99, suggest that holding the nozzle temperature constant at 235 °C and reducing the printing speed, from 100mm/s to 80mm/s to 60mm/s would decrease the specimen modulus. This would also decrease the specimen yield strength and consequently, the ultimate tensile strength.

The plots for specimen B10, 13 and 16 shown in Fig. 4.100, suggest that holding the nozzle temperature constant at 225 °C and reducing the printing speed, from 100mm/s to 80mm/s to 60mm/s would initially decrease, then subsequently increase the specimen modulus. This would also initially decrease, then subsequently increase the specimen yield strength. The ultimate tensile strength initially decreases, then subsequently increases.

The plots for specimen B19, 22 and 25 shown in Fig. 4.101 suggest that holding the nozzle temperature constant at 215 °C and reducing the printing speed, from 100mm/s to 80mm/s to 60mm/s would initially increase, then subsequently decrease the specimen modulus. This would also initially increase, then subsequently increase the specimen yield

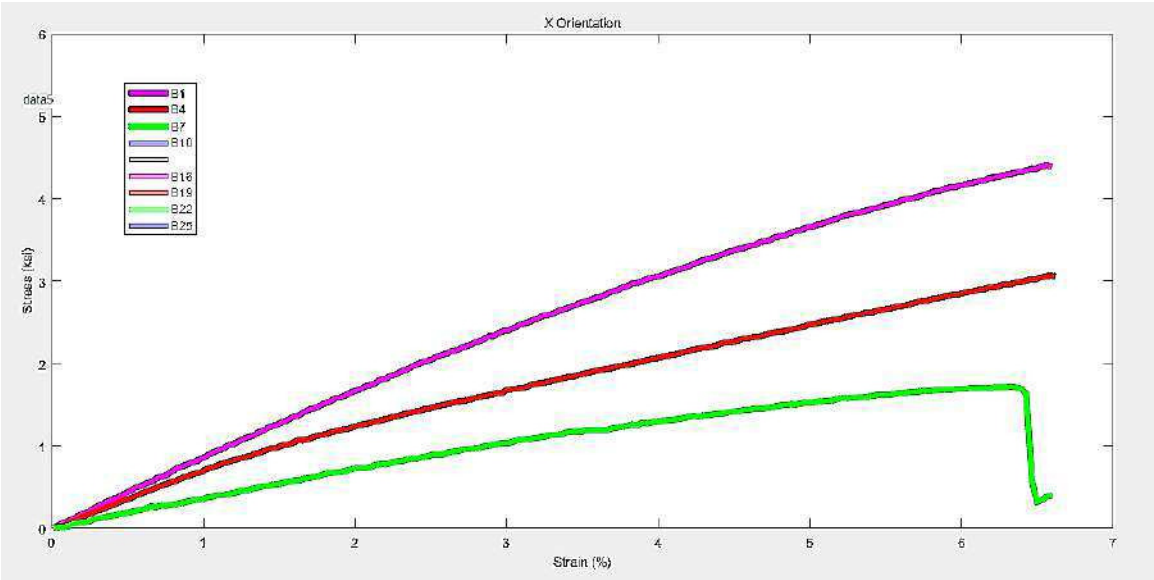

Figure 4.99. Plot of stress-strain curve for specimens B1, 4 and 7, printed in the x-axis orientation on the AirWolf 3-D Printer.

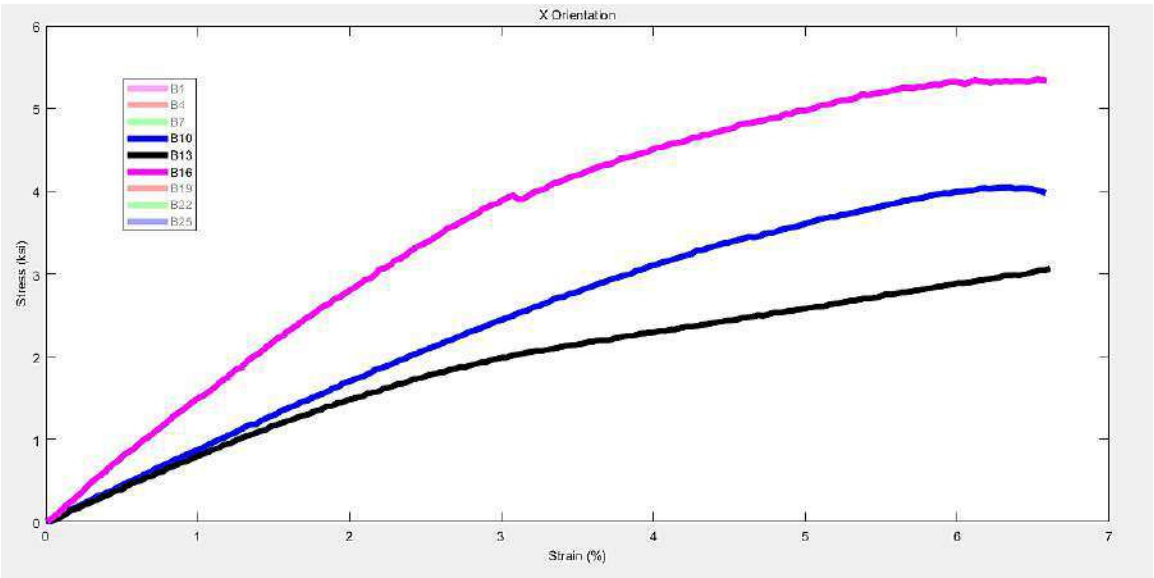

Figure 4.100. Plot of stress-strain curve for specimens B10, 13 and 16, printed in the x-axis orientation on the AirWolf 3-D Printer.

strength. Similarly, the ultimate tensile strength initially increases, then subsequently decreases.

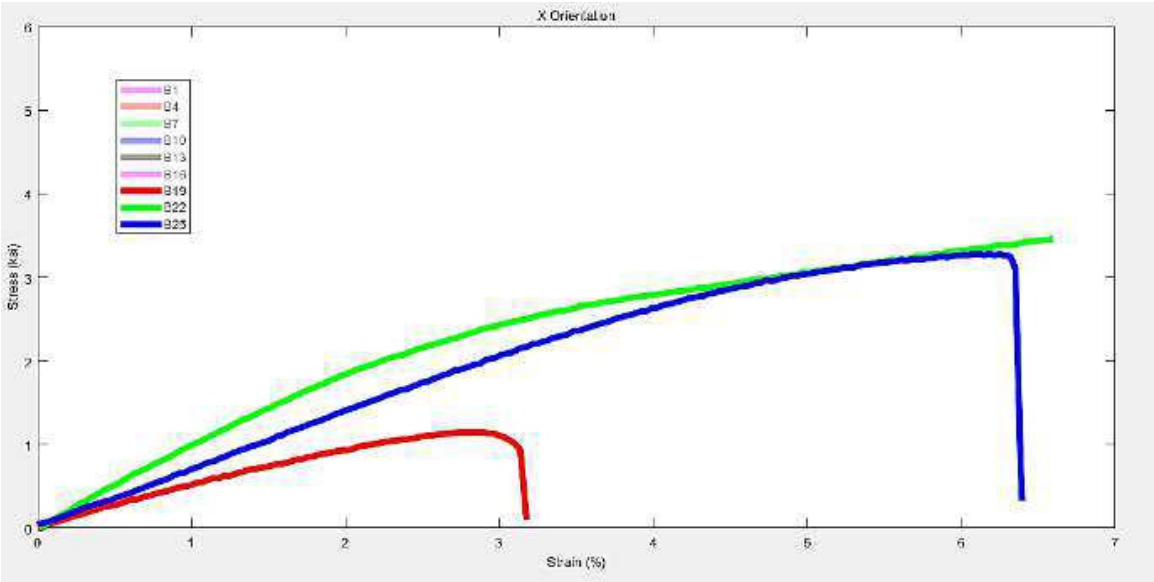

Figure 4.101. Plot of stress-strain curve for specimens B19, 22 and 25, printed in the x-axis orientation on the AirWolf 3-D Printer.

For the specimens printed in the x-axis orientation, specimen B16; printed with nozzle temperature of 225 °C and at printing speed of 60mm/s possesses the highest modulus, yield strength, and ultimate tensile strength. Specimen B7 (printed with nozzle temperature of 235 °C and at printing speed of 100 mm/s), was observed to possess the lowest modulus, yield strength, and ultimate tensile strength. Fig. 4.102 presents the plot for stress strain curve of all the specimens printed in the xaxis orientation.

The values of the modulus, yield strength and ultimate tensile strength of the specimens gotten from the tensile strength analysis of the specimens printed in the y-axis orientation are presented in Table 4.6

The plots for specimen B2, 5 and 8 shown in Fig. 4.103, suggest that holding the nozzle temperature constant at 235 °C and reducing the printing speed, from 100mm/s to 80mm/s to 60mm/s would decrease the specimen modulus. This would also decrease the specimen the yield strength and ultimate tensile strength.

The plots for specimen B11, 14 and 17 shown in Fig. 4.104, suggest that holding the nozzle temperature constant at 225 °C and reducing the printing speed, from 100mm/s

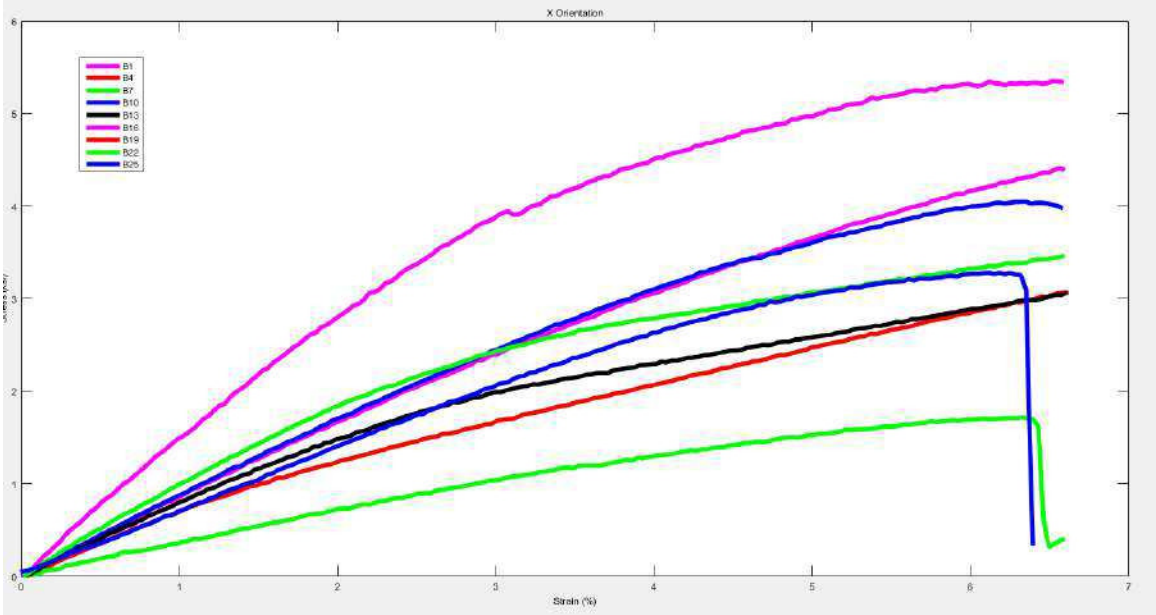

Figure 4.102. Plot of stress-strain curve for all specimens printed in the x-axis orientation on the AirWolf 3-D Printer.

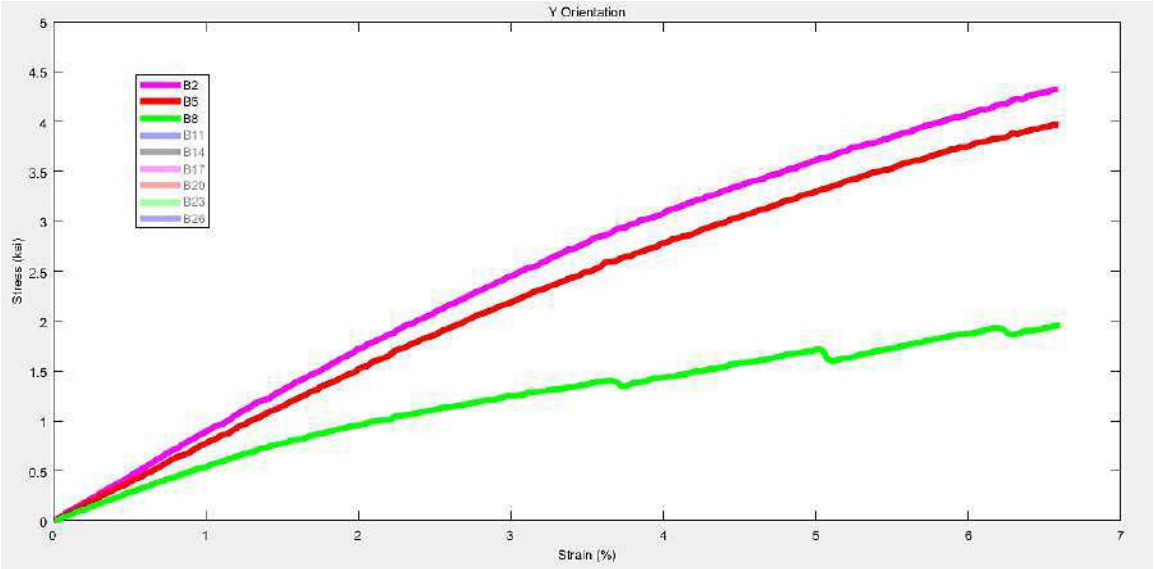

Figure 4.103. Plot of stress-strain curve for specimens B2, 5 and 8, printed in the y-axis orientation on the AirWolf. 3-D Printer.

Table 4.6.
Mechanical properties of specimens printed in the y-axis orientation on the AirWolf 3-D Printer.

Specimen number	Modulus (ksi)	Yield strength (ksi)	Ultimate tensile strength (ksi)
B2	89.43095	0.1803	4.326
B5	77.53631	0.16136	3.97
B8	55.1508	0.1134	1.956
B11	98.59816	0.19674	4.828
B14	91.77735	0.1846	4.859
B17	98.30687	0.19598	4.563
B20	69.5771	0.14696	2.192
B23	104.8892	0.21132	4.157
B26	81.17228	0.16452	2.563

to 80mm/s to 60mm/s would initially decrease, then subsequently increase the specimen modulus. This would also initially decrease, then subsequently increase the specimen yield strength. The ultimate tensile strength would however initially increase, then subsequently decrease.

The plots for specimen B20, 23 and 26 shown in Fig. 4.105, suggest that holding the nozzle temperature constant at 215 °C and reducing the printing speed, from 100mm/s to 80mm/s to 60mm/s would initially increase, then subsequently decrease the specimen modulus. This would also initially increase, then subsequently decrease the specimen yield strength. The ultimate tensile strength would also initially increase, then subsequently decrease.

For the specimens printed in the y-axis orientation, specimen B23, printed with nozzle temperature of 215 °C and at printing speed of 80 mm/s possesses the highest modulus and yield strength. Specimen B14, printed with nozzle temperature of 225 °C and at printing speed of 80mm/s possesses the highest ultimate tensile strength. Specimen B8

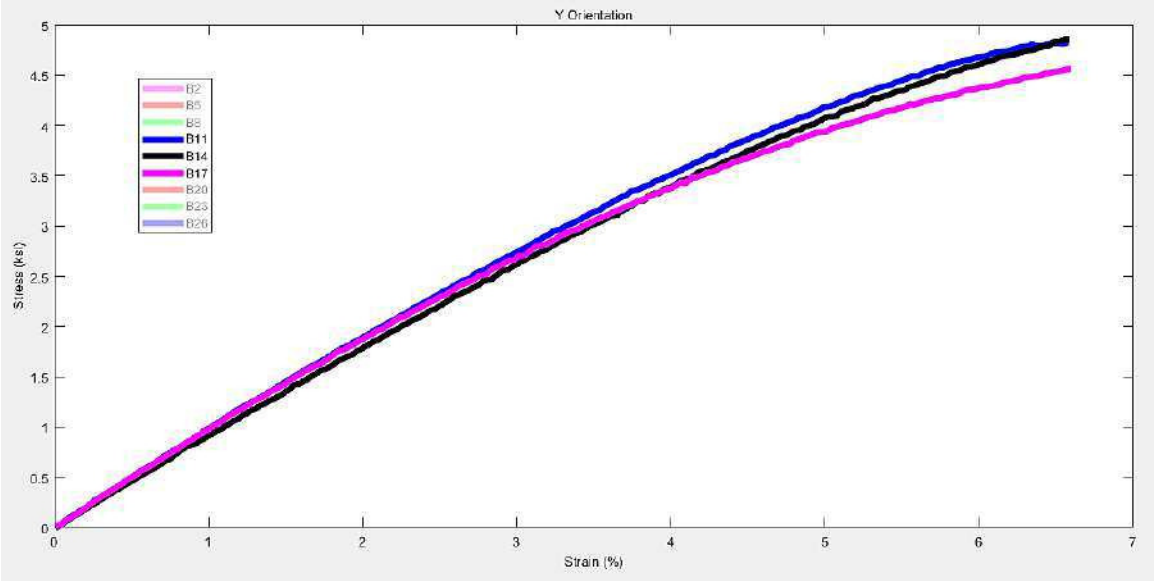

Figure 4.104. Plot of stress-strain curve for specimens B11, 14 and 17, printed in the y-axis orientation on the AirWolf. 3-D Printer.

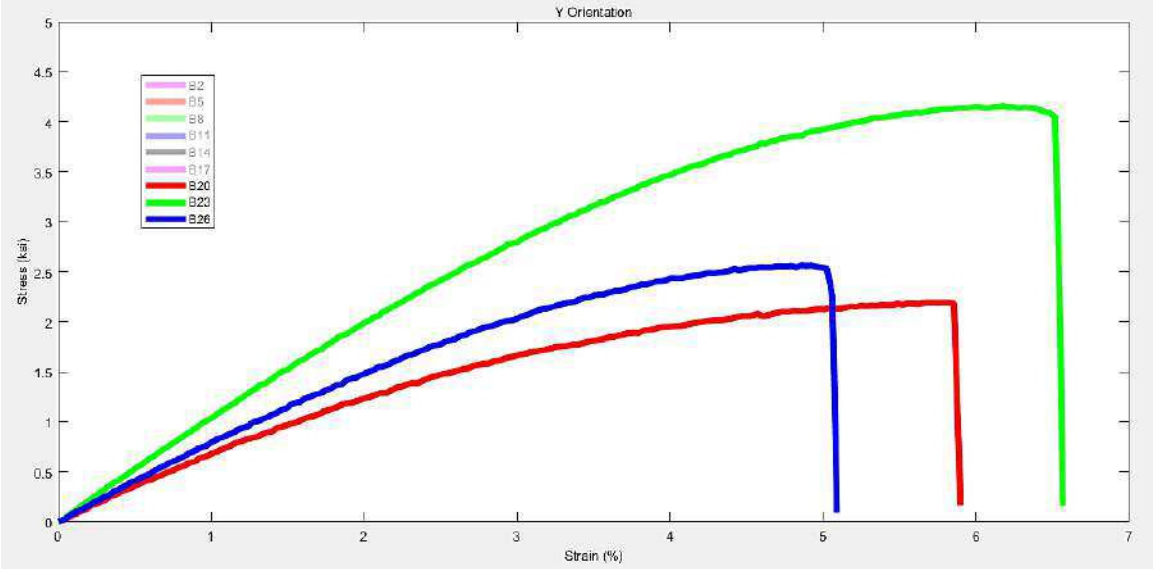

Figure 4.105. Plot of stress-strain curve for specimens B20, 23 and 26, printed in the y-axis orientation on the AirWolf. 3-D Printer.

(printed with nozzle temperature of 235 ℃ and at printing speed of 60mm/s), was observed to possess the lowest modulus, yield strength, and ultimate tensile strength.

Fig. 4.106 presents the plot for stress strain curve of the specimens printed in the y-axis orientation.

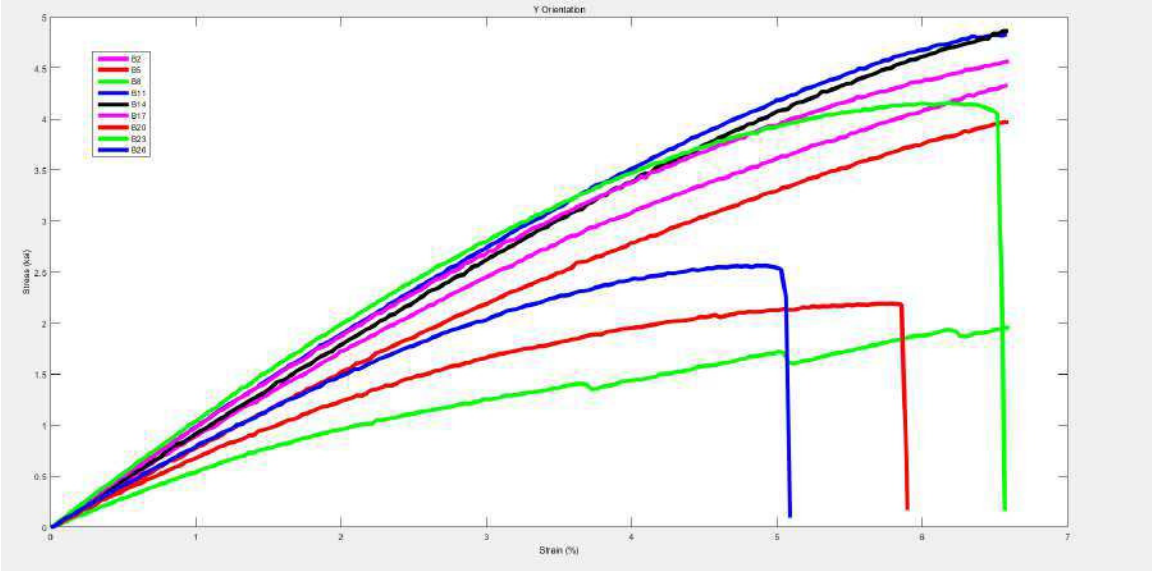

Figure 4.106. Plot of stress strain curve for all specimens printed in the yaxis orientation on the AirWolf 3-D Printer.

Values of the modulus, yield strength and ultimate tensile strength of the specimens gotten from the tensile strength analysis of the specimens printed in the z-axis orientation are presented in Table 4.7

The plots for specimen B3, 6 and 9 shown in Fig. 4.107, suggest that holding the nozzle temperature constant at 235 °C and reducing the printing speed, from 100mm/s to 80mm/s to 60mm/s would initially increase, then subsequently decrease the specimen modulus. This would also initially increase, then subsequently decrease the specimen yield strength. The ultimate tensile strength would also initially increase, then subsequently decrease.

The plots for specimen B12, 15 and 18 shown in Fig. 4.108, suggest that holding the nozzle temperature constant at 225 °C and reducing the printing speed, from 100mm/s to 80mm/s to 60mm/s would initially decrease, then subsequently increase the specimen modulus. However, this would cause the specimen yield strength to increase. The ultimate tensile would also increase.

Table 4.7.
Mechanical properties of specimens printed in the z-axis orientation on the AirWolf 3-D Printer.

Specimen number	Modulus (ksi)	Yield strength (ksi)	Ultimate tensile strength (ksi)
B3	74.14021	0.14756	3.352
B6	114.4914	0.2398	5.613
B9	26.72162	0.05335	0.822
B12	80.70902	0.13858	2.252
B15	78.71204	0.164	2.359
B18	88.03205	0.17678	2.983
B21	85.3469	0.173	2.442
B24	95.21841	0.3042	4.724
B27	91.42737	0.19012	2.312

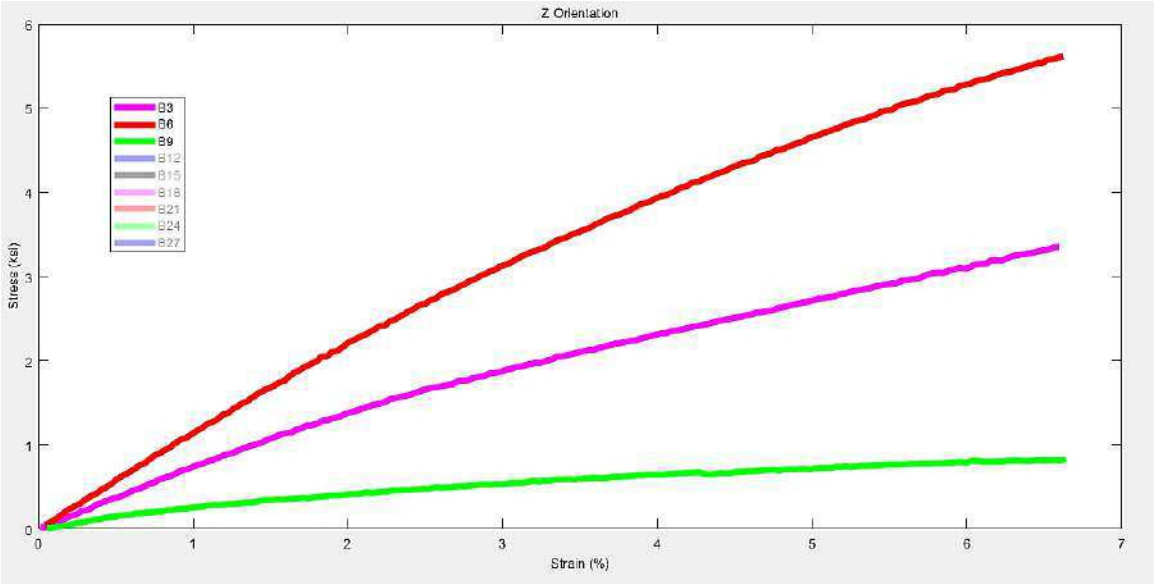

Figure 4.107. Plot of stress-strain curve for specimens B3, 6 and 9, printed in the z-axis orientation on the AirWolf 3-D Printer.

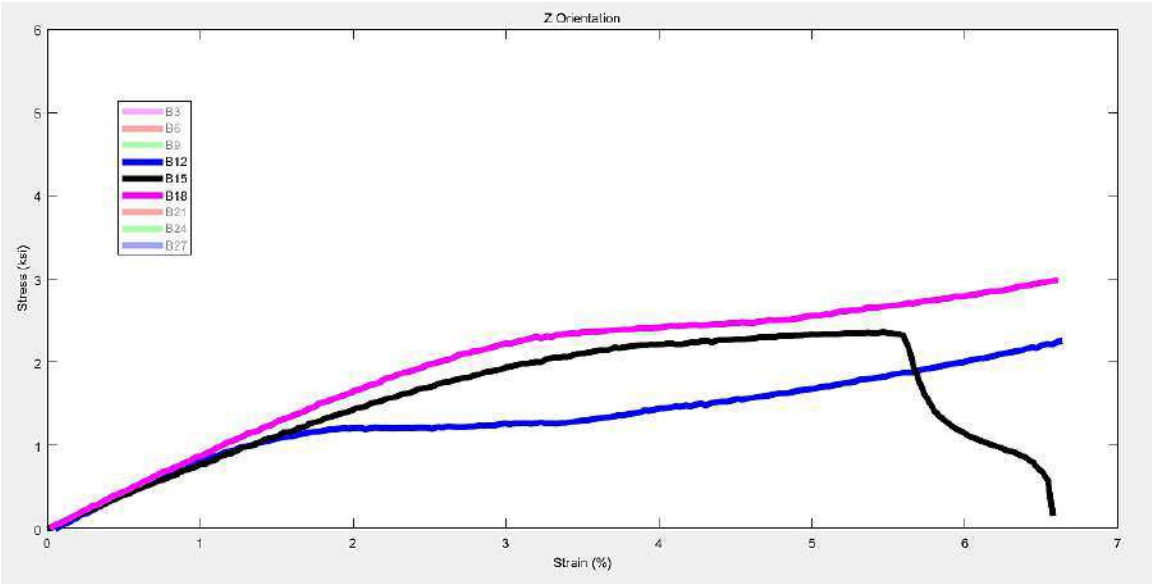

Figure 4.108. Plot of stress-strain curve for specimens B12, 15 and 18, printed in the z-axis orientation on the AirWolf 3-D Printer.

The plots for specimen B21, 24 and 27 shown in Fig. 4.109, suggest that holding the nozzle temperature constant at 215 °C and reducing the printing speed, from 100mm/s to 80mm/s to 60mm/s would initially increase then decrease the specimen modulus. This would also initially increase then decrease the specimen yield strength and ultimate tensile strength.

For the specimens printed in the z-axis orientation, specimen B6; printed with nozzle temperature of 235 °C and at printing speed of 80mm/s possesses the highest modulus and ultimate tensile strength. Specimen B24; printed with nozzle temperature of 235 °C and at printing speed of 80mm/s possesses the highest yield strength. Specimen B9; printed with nozzle temperature of 235 °C and at printing speed of 60mm/s was observed to possess the lowest modulus, yield strength and ultimate tensile strength. Fig. 4.110 presents the plot for stress strain curve of the specimens printed in the z-axis orientation.

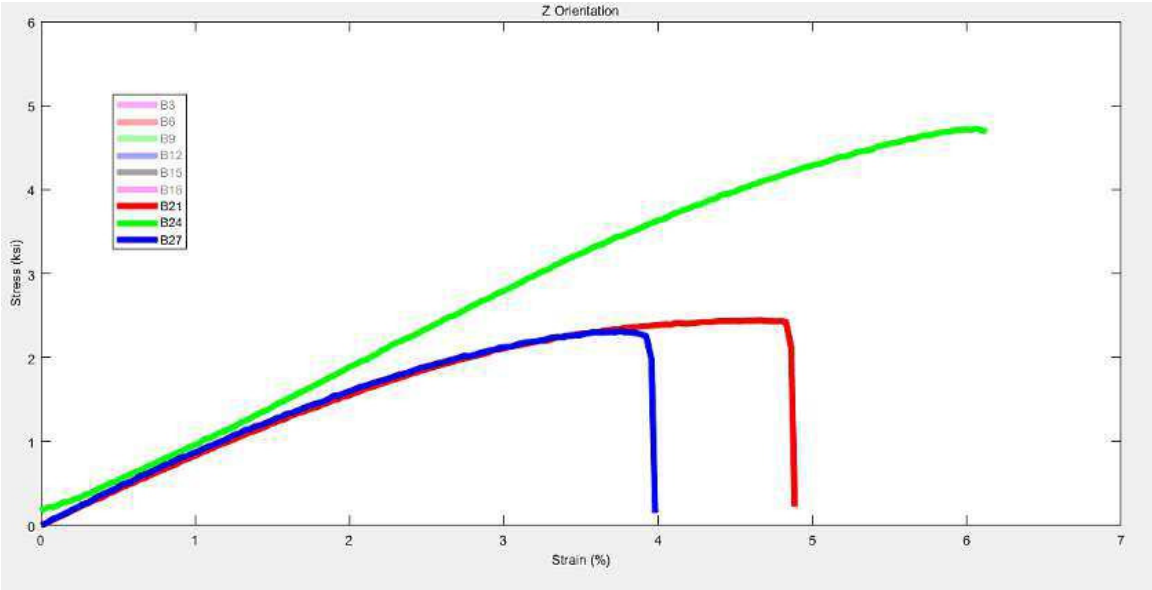

Figure 4.109. Plot of stress-strain curve for specimens B21, 24 and 27, printed in the z-axis orientation on the AirWolf 3-D Printer.

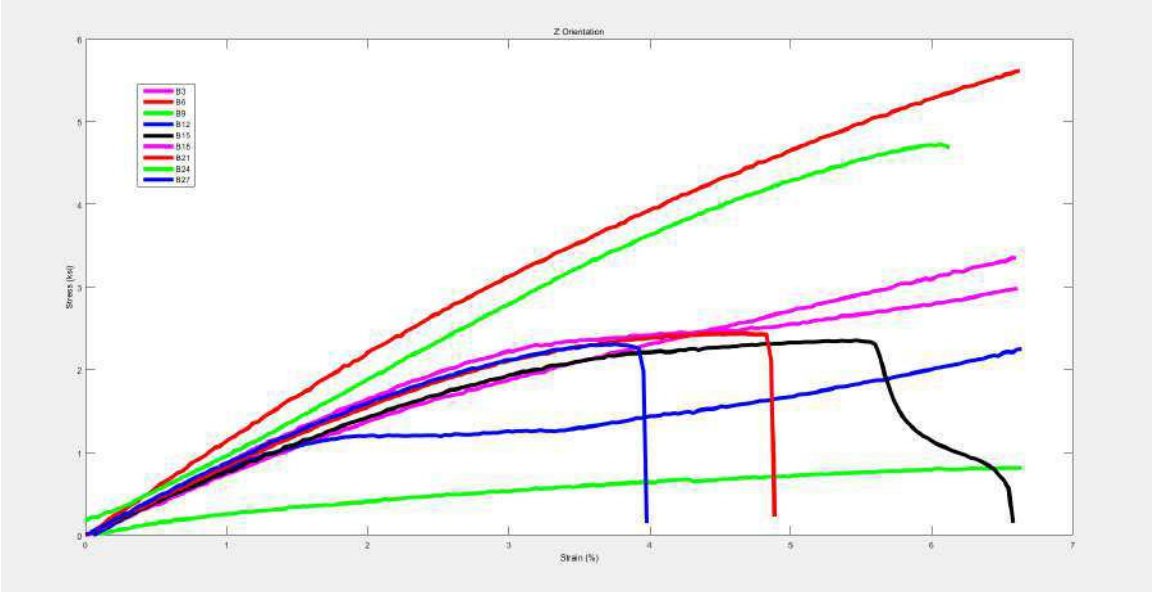

Figure 4.110. Plot of stress strain curve for all specimens printed in the z axis orientation on the AirWolf 3-D Printer.

5. CONCLUSION AND FUTURE WORK

5.1 Conclusion

This research work has presented the experimental analysis of thermal and parameter effect on a fused deposition modeling process. The study has also integrated an in-situ monitoring procedure into the fabrication process on the AirWolf 3-D printer. The results from mechanical analysis of specimens fabricated on the MakerBot 5th Gen 3-D printer were used as an initial run to gain some insight on the effect of adjusting the printing parameters. In-situ monitoring was then performed as specimens were fabricated on an AirWolf 3-D printer. The real-time thermal data acquired has served to provide some insight on the product and process evolution. The results in Table 5.1 and 5.2

The results suggest that the specimens printed in the y-axis orientation perform better than specimens printed in the x-axis and z-axis orientation. Also the information retrieved from observing the temperature profile and temporal plot, suggest that a fabrication process with more even temperature distribution across individual build layers and through the part layers would facilitate better mechanical properties.

Table 5.1.
Comparison of highest modulus values for specimens printed on the AirWolf 3-D Printer.

Specimen number	Modulus ksi	Nozzle temperature °C	Printing speed mm/s	Printing axis
B10	151.4242	225	60	x
B23	104.8892	215	80	y
B6	114.4914	235	80	z

Table 5.2.
Comparison of highest yield strength values for specimen printed on the AirWolf 3-D Printer.

Specimen number	Yield strength ksi	Nozzle temperature °C	Printing speed mm/s	Printing axis
B16	0.30314	225	60	x
B23	0.21132	215	80	y
B24	0.30420	215	80	z

5.2 Future Work

The AirWolf 3-D printer has an open structure. Thus surrounding temperature would have had a effect on the build layers. During the fabrication process the effect of ambient cooling was not controlled or measured. These could be controlled and studied in future research. It was also understood during in-situ monitoring process, that only information from the build layer surface were being retrieved by the Research IR camera. Further studies could also be carried out with equipment to determine the sub-surface thermal evolution of the build process. Correlating the microstructural characteristics of the specimens to the printing properties and thermal evolution would also provide more insights I this subject matter.

Additive manufacturing has capacities desired by the manufacturing industry. These capabilities provide impetus for the significant interest and growth of the various AM technologies. The merits of additive manufacturing include its potential in;

- improving the manufacturing processs energy efficiency [84] , [85]
- reducing material use and wastage [86]
- enhancing rapid product development [87]
- facilitating freeform and freedom in design [88] and
- facilitating product customization [89]

In addition to the aforementioned points, addictive manufacturing facilitates sustainability and environmental impact reduction. By optimizing feedstock and raw material utilization. Additive manufacturing techniques are similar in the mode of material processing i.e., change in physical state of the raw material through the application of heat and or mechanical forces. The image monitoring, processing techniques and results analysis derived from this work can be applied in real-time monitoring and control of metal additive manufacturing technologies Fig. 5.1

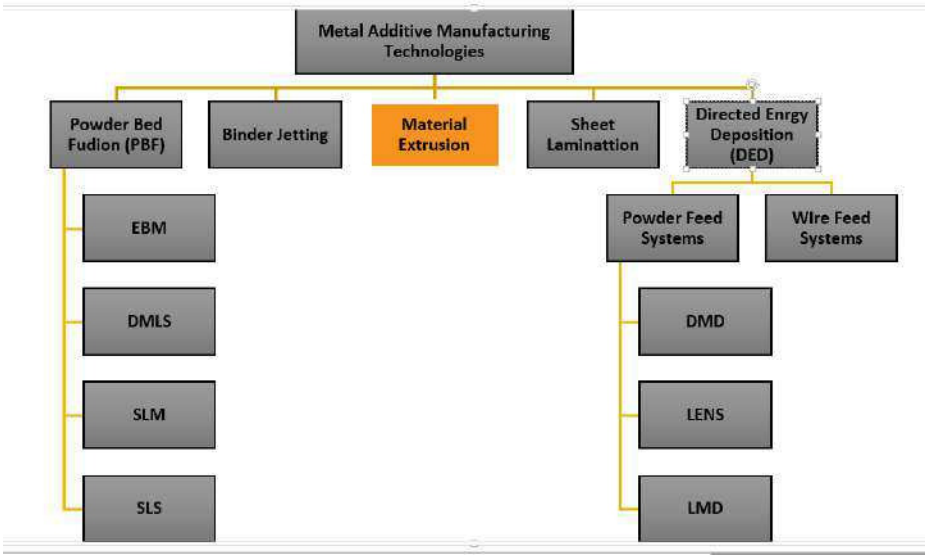

Figure 5.1. Additive manufacturing technologies; (Electron Beam Machining (EBM), Direct Metal Laser Sintering (DMLS), Selective Laser Melting (SLM), Selective Laser Sintering (SLS), Selective Laser Sintering, Direct Metal Deposition (DMD), Laser Engineered Net Shaping (LENS), Laser Metal Deposition (LMD) [1] .

REFERENCES

REFERENCES

[1] S. M. Yusuf and N. Gao, "Influence of energy density on metallurgy and properties in metal additive manufacturing," *Materials Science and Technology*, pp. 1–21, 2017.

[2] S. Moylan, J. Slotwinski, A. Cooke, K. Jurrens, and M. A. Donmez, "An additive manufacturing test artifact," *Journal of research of the National Institute of Standards and Technology*, vol. 119, p. 429, 2014.

[3] ASTM, "F2792. 2012. standard terminology for additive manufacturing technologies," *American Society for Testing and Materials ASTM F2792-10e1*, 2012.

[4] I. Gibson, D. Rosen, and B. Stucker, *Additive manufacturing technologies: 3D printing, rapid prototyping, and direct digital manufacturing*. Springer, 2014.

[5] C. Chu, G. Graf, and D. W. Rosen, "Design for additive manufacturing of cellular structures," *Computer-Aided Design and Applications*, vol. 5, no. 5, pp. 686–696, 2008.

[6] D. Manfredi, F. Calignano, M. Krishnan, R. Canali, E. P. Ambrosio, and E. Atzeni, "From powders to dense metal parts: Characterization of a commercial alsimg alloy processed through direct metal laser sintering," *Materials*, vol. 6, no. 3, pp. 856–869, 2013.

[7] B. Vayre, F. Vignat, and F. Villeneuve, "Designing for additive manufacturing," *Procedia CIrP*, vol. 3, pp. 632–637, 2012.

[8] R. V. Rao and D. P. Rai, "Optimization of fused deposition modeling process using teaching-learning-based optimization algorithm," *Engineering Science and Technology, an International Journal*, vol. 19, no. 1, pp. 587–603, 2016.

[9] M. R. Z. Farahani, *Integrated micro PEM fuel cell with self-regulated hydrogen generation from ammonia borane*. Purdue University, 2015.

[10] L. Novakova-Marcincinova and I. Kuric, "Basic and advanced materials for fused deposition modeling rapid prototyping technology," *Manuf. and Ind. Eng*, vol. 11, no. 1, pp. 24–27, 2012.

[11] S. K. Everton, M. Hirsch, P. Stravroulakis, R. K. Leach, and A. T. Clare, "Review of in-situ process monitoring and in-situ metrology for metal additive manufacturing," *Materials & Design*, vol. 95, pp. 431–445, 2016.

[12] X. Zhou and S.-J. Hsieh, "Thermal analysis of fused deposition modeling process using infrared thermography imaging and finite element modeling," in *SPIE Commercial+ Scientific Sensing and Imaging*. International Society for Optics and Photonics, 2017, pp. 1 021 409–1 021 409.

[13] E. Atzeni and A. Salmi, "Economics of additive manufacturing for end-usable metal parts," *The International Journal of Advanced Manufacturing Technology*, vol. 62, no. 9, pp. 1147–1155, 2012.

[14] D. Gu, Y. Shen, J. Yang, and Y. Wang, "Effects of processing parameters on direct laser sintering of multicomponent cu based metal powder," *Materials science and technology*, vol. 22, no. 12, pp. 1449–1455, 2006.

[15] A. Joshi, A. Patnaik, B. Gangil, and S. Kumar, "Laser assisted rapid manufacturing technique for the manufacturing of functionally graded materials," in *Engineering and Systems (SCES), 2012 Students Conference on*. IEEE, 2012, pp. 1–3.

[16] D. L. Bourell, J. J. Beaman, M. C. Leu, and D. W. Rosen, "A brief history of additive manufacturing and the 2009 roadmap for additive manufacturing: looking back and looking ahead," *Proceedings of RapidTech*, pp. 24–25, 2009.

[17] M. Colledani, T. Tolio, A. Fischer, B. Iung, G. Lanza, R. Schmitt, and J. Váncza, "Design and management of manufacturing systems for production quality," *CIRP Annals-Manufacturing Technology*, vol. 63, no. 2, pp. 773–796, 2014.

[18] S. Clijsters, T. Craeghs, S. Buls, K. Kempen, and J.-P. Kruth, "In situ quality control of the selective laser melting process using a high-speed, real-time melt pool monitoring system," *The International Journal of Advanced Manufacturing Technology*, vol. 75, no. 5-8, pp. 1089–1101, 2014.

[19] B. N. Turner, R. Strong, and S. A. Gold, "A review of melt extrusion additive manufacturing processes: I. process design and modeling," *Rapid Prototyping Journal*, vol. 20, no. 3, pp. 192–204, 2014.

[20] A. Dorigato, V. Moretti, S. Dul, S. Unterberger, and A. Pegoretti, "Electrically conductive nanocomposites for fused deposition modelling," *Synthetic Metals*, vol. 226, pp. 7–14, 2017.

[21] H. Brooks, A. Rennie, T. Abram, J. McGovern, and F. Caron, "Variable fused deposition modelling: analysis of benefits, concept design and tool path generation," in *5th International Conference on Advanced Research in Virtual and Rapid Prototyping, Leiria, Portugal*, 2011, pp. 511–517.

[22] C. Liu, H. Qin, and P. Mather, "Review of progress in shape-memory polymers," *Journal of Materials Chemistry*, vol. 17, no. 16, pp. 1543–1558, 2007.

[23] M. Chanda and S. K. Roy, *Plastics technology handbook*. CRC press, 2006.

[24] S. H. Ahn, C. Baek, S. Lee, and I. S. Ahn, "Anisotropic tensile failure model of rapid prototyping parts-fused deposition modeling (fdm)," *International Journal of Modern Physics B*, vol. 17, no. 08n09, pp. 1510–1516, 2003.

[25] C. Casavola, A. Cazzato, V. Moramarco, and C. Pappalettere, "Orthotropic mechanical properties of fused deposition modelling parts described by classical laminate theory," *Materials & Design*, vol. 90, pp. 453–458, 2016.

[26] K. Upadhyay, R. Dwivedi, and A. K. Singh, "Determination and comparison of the anisotropic strengths of fused deposition modeling p400 abs," in *Advances in 3D Printing & Additive Manufacturing Technologies*. Springer, 2017, pp. 9–28.

[27] B. Tymrak, M. Kreiger, and J. M. Pearce, "Mechanical properties of components fabricated with open-source 3-d printers under realistic environmental conditions," *Materials & Design*, vol. 58, pp. 242–246, 2014.

[28] J. C. Snyder, C. K. Stimpson, K. A. Thole, and D. J. Mongillo, "Build direction effects on microchannel tolerance and surface roughness," *Journal of Mechanical Design*, vol. 137, no. 11, p. 111411, 2015.

[29] J. C. Riddick, M. A. Haile, R. Von Wahlde, D. P. Cole, O. Bamiduro, and T. E. Johnson, "Fractographic analysis of tensile failure of acrylonitrile-butadiene-styrene fabricated by fused deposition modeling," *Additive Manufacturing*, vol. 11, pp. 49–59, 2016.

[30] J. Chacón, M. Caminero, E. García-Plaza, and P. Núñez, "Additive manufacturing of pla structures using fused deposition modelling: Effect of process parameters on mechanical properties and their optimal selection," *Materials & Design*, vol. 124, pp. 143–157, 2017.

[31] R. Van Weeren, M. Agarwala, V. Jamalabad, A. Bandyophadyay, R. Vaidyanathan, N. Langrana, A. Safari, P. Whalen, S. Danforth, and C. Ballard, "Quality of parts processed by fused deposition," in *Proceedings of the Solid Freeform Fabrication Symposium*, vol. 6, 1995, pp. 314–21.

[32] D. Liao and L. C. J. Z. R. Liu, "Modeling of thermal stress during casting solidification process," in *Engineering Plasticity and Its Applications: Proceedings of the 10th Asia-Pacific Conference, Wuhan, China, 15-17 November 2010*. World Scientific, 2011, p. 56.

[33] N. K. Spinnie, "Large scale fused deposition modeling: the effect of process parameters on bead geometry." Ph.D. dissertation, 2016.

[34] R. Orlando, V. Kunc, C. Duty, and L. Love, "Electromagnetic blunting of defects within fused deposition modeling (fdm) components," Apr. 29 2015, uS Patent App. 14/699,426.

[35] D. M. Roberson III, "Sensor-based online process monitoring in advanced manufacturing," Ph.D. dissertation, Virginia Tech, 2016.

[36] P. M. Pandey, N. V. Reddy, and S. G. Dhande, "Improvement of surface finish by staircase machining in fused deposition modeling," *Journal of materials processing technology*, vol. 132, no. 1, pp. 323–331, 2003.

[37] A. Garg, A. Bhattacharya, and A. Batish, "On surface finish and dimensional accuracy of fdm parts after cold vapor treatment," *Materials and Manufacturing Processes*, vol. 31, no. 4, pp. 522–529, 2016.

[38] R. Carlyle, "Thoughts on abs warp prevention," accessed on 1st July, 2017. [Online]. Available: https://groups.google.com/d/msg/makerbot/4evJNxIPY2E/RWBGOC0x0nAJ

[39] M. Nazan, F. Ramli, M. Alkahari, M. Abdullah, and M. Sudin, "An exploration of polymer adhesion on 3d printer bed," in *IOP Conference Series: Materials Science and Engineering*, vol. 210, no. 1. IOP Publishing, 2017, pp. 12–62.

[40] L. R. Sbriglia, A. M. Baker, J. M. Thompson, R. V. Morgan, A. J. Wachtor, and J. D. Bernardin, "Embedding sensors in fdm plastic parts during additive manufacturing," in *Topics in Modal Analysis & Testing, Volume 10*. Springer, 2016, pp. 205–214.

[41] B. Hudson, "How to design fdm parts," accessed on 26th October, 2017. [Online]. Available: https://3dhubs.com/knowledge base

[42] E. Macdonald, R. Salas, D. Espalin, M. Perez, E. Aguilera, D. Muse, and R. B. Wicker, "3d printing for the rapid prototyping of structural electronics," *IEEE Access*, vol. 2, pp. 234–242, 2014.

[43] T. Rayna and L. Striukova, "From rapid prototyping to home fabrication: How 3d printing is changing business model innovation," *Technological Forecasting and Social Change*, vol. 102, pp. 214–224, 2016.

[44] J. Zaragoza-Siqueiros and H. I. Medellín-Castillo, "Design for rapid prototyping, manufacturing and tooling: Guidelines," in *Proceedings of the ASME 2014 International Mechanical Engineering Congress and Exposition*, 2014, pp. 1–10.

[45] L. Bian, S. M. Thompson, and N. Shamsaei, "Mechanical properties and microstructural features of direct laser-deposited ti-6al-4v," *Jom*, vol. 67, no. 3, pp. 629–638, 2015.

[46] Y.-A. Jin, Y. He, and J. Z. Fu, "An adaptive tool path generation for fused deposition modeling," in *Advanced Materials Research*, vol. 819. Trans Tech Publ, 2013, pp. 7–12.

[47] Y.-A. Jin, Y. He, G.-h. Xue, and J.-z. Fu, "A parallel-based path generation method for fused deposition modeling." *International Journal of Advanced Manufacturing Technology*, vol. 77, pp. 1–11, 2015.

[48] I. Ishak, J. Fisher, and P. Larochelle, "Robot arm platform for rapid prototyping: Concept," in *Proceedings of Florida Conference on Recent Advances in Robotics*, 2015, pp. 1–4.

[49] C. Koch, L. Van Hulle, and N. Rudolph, "Investigation of mechanical anisotropy of the fused filament fabrication process via customized tool path generation," *Additive Manufacturing*, pp. 138–145, 2017.

[50] I. M. Olioul and H.-C. Kim, "An algorithm for the removing of offset loop twists during the tool path generation of fdm 3d printer," , vol. 16, no. 3, pp. 1–8, 2017.

[51] A. Kout and H. Müller, "Tool-adaptive offset paths on triangular mesh workpiece surfaces," *Computer-Aided Design*, vol. 50, pp. 61–73, 2014.

[52] Q. Zou, J. Zhang, B. Deng, and J. Zhao, "Iso-level tool path planning for free-form surfaces," *Computer-Aided Design*, vol. 53, pp. 117–125, 2014.

[53] R. dAveni, "The 3-d printing revolution," *Harvard Business Review*, vol. 93, no. 5, pp. 40–48, 2015.

[54] STRATASYS, "Fortus 380mc and 450mc," [Online;Accessed on 27th October, 2017]. [Online]. Available: https://stratasys.com/media/files/printerspecsheets/pssfdm380mc450mc

[55] R. Gurka, "3d printing the next five years," [Online; Accessed on 27th October, 2017]. [Online]. Available: https://bigrep.com/3dprinting

[56] A. Tseng and M. Tanaka, "Advanced deposition techniques for freeform fabrication of metal and ceramic parts," *Rapid Prototyping Journal*, vol. 7, no. 1, pp. 6–17, 2001.

[57] H. Brooks, M. E. Lupeanu, and B. Piorkowski, "Research towards high speed extrusion freeforming," *International Journal of Rapid Manufacturing*, vol. 3, no. 2-3, pp. 154–171, 2013.

[58] G. C. Onwubolu and F. Rayegani, "Characterization and optimization of mechanical properties of abs parts manufactured by the fused deposition modelling process," *International Journal of Manufacturing Engineering*, vol. 2014, 2014.

[59] N. Mohan, P. Senthil, S. Vinodh, and N. Jayanth, "A review on composite materials and process parameters optimisation for the fused deposition modelling process," *Virtual and Physical Prototyping*, vol. 12, no. 1, pp. 47–59, 2017.

[60] A. Qattawi, M. A. Ablat *et al.*, "Design consideration for additive manufacturing: Fused deposition modelling," *Open Journal of Applied Sciences*, vol. 7, no. 06, p. 291, 2017.

[61] M. Mani, B. M. Lane, M. A. Donmez, S. C. Feng, and S. P. Moylan, "A review on measurement science needs for real-time control of additive manufacturing metal powder bed fusion processes," *International Journal of Production Research*, vol. 55, no. 5, pp. 1400–1418, 2017.

[62] D. L. Russell, "Real-time monitoring and control of additive manufacturing processes," NIST U.S. Department of Commerce, Maryland, 2014.

[63] I. Cummings, E. Hillstrom, R. Newton, E. Flynn, and A. Wachtor, "In-process ultrasonic inspection of additive manufactured parts," in *Topics in Modal Analysis & Testing, Volume 10*. Springer, 2016, pp. 235–247.

[64] J. O. Kim and D. J. Kim, "Apparatus for preventing clogging of printer nozzle and printer ink cartridge," Apr. 26 2016, uS Patent 9,321,270.

[65] Y. Tlegenov, Y. Tlegenov, Y. S. Wong, Y. S. Wong, G. S. Hong, and G. S. Hong, "A dynamic model for nozzle clog monitoring in fused deposition modelling," *Rapid Prototyping Journal*, vol. 23, no. 2, pp. 391–400, 2017.

[66] H. Wu, Y. Wang, and Z. Yu, "In situ monitoring of fdm machine condition via acoustic emission," *The International Journal of Advanced Manufacturing Technology*, vol. 84, no. 5-8, pp. 1483–1495, 2016.

[67] F. Baumann, M. Schön, J. Eichhoff, and D. Roller, "Concept development of a sensor array for 3d printer," *Procedia CIRP*, vol. 51, pp. 24–31, 2016.

[68] X. Zhou, S.-J. Hsieh, and Y. Sun, "Experimental and numerical investigation of the thermal behaviour of polylactic acid during the fused deposition process," *Virtual and Physical Prototyping*, pp. 1–13, 2017.

[69] S. Nuchitprasitchai, M. C. Roggemann, and J. M. Pearce, "Three hundred and sixty degree real-time monitoring of 3-d printing using computer analysis of two camera views," *Journal of Manufacturing and Materials Processing*, vol. 1, no. 1, p. 2, 2017.

[70] C.-C. Kuo, W.-H. Chen, J.-F. Li, and Y.-J. Zhu, "Development of a flexible modeling base for additive manufacturing," *The International Journal of Advanced Manufacturing Technology*, pp. 1–9, 2017.

[71] M. F. Afrose, S. Masood, P. Iovenitti, M. Nikzad, and I. Sbarski, "Effects of part build orientations on fatigue behaviour of fdm-processed pla material," *Progress in Additive Manufacturing*, vol. 1, no. 1-2, pp. 21–28, 2016.

[72] E. Kim, E. Kim, Y.-J. Shin, Y.-J. Shin, S.-H. Ahn, and S.-H. Ahn, "The effects of moisture and temperature on the mechanical properties of additive manufacturing components: fused deposition modeling," *Rapid Prototyping Journal*, vol. 22, no. 6, pp. 887–894, 2016.

[73] R. H. Sanatgar, C. Campagne, and V. Nierstrasz, "Investigation of the adhesion properties of direct 3d printing of polymers and nanocomposites on textiles: Effect of fdm printing process parameters," *Applied Surface Science*, vol. 403, pp. 551–563, 2017.

[74] N. Aliheidari, R. Tripuraneni, C. Hohimer, J. Christ, A. Ameli, and S. Nadimpalli, "The impact of nozzle and bed temperatures on the fracture resistance of fdm printed materials," in *Behavior and Mechanics of Multifunctional Materials and Composites 2017*, vol. 10165. International Society for Optics and Photonics, 2017, p. 1016512.

[75] C. Kousiatza, N. Chatzidai, and D. Karalekas, "Temperature mapping of 3d printed polymer plates: Experimental and numerical study," *Sensors*, vol. 17, no. 3, p. 456, 2017.

[76] A. Einstein and O. Stern, "Some arguments for the assumption of molecular agitation at absolute zero," *Annalen Phys.*, vol. 14, pp. 489–499, 1912.

[77] J. D. Vincent, J. Vampola, S. Hodges, G. Pierce, and M. Stegall, *Fundamentals of Infrared and Visible Detector Operation and Testing*. John Wiley & Sons, 2015.

[78] R. Usamentiaga, P. Venegas, J. Guerediaga, L. Vega, J. Molleda, and F. G. Bulnes, "Infrared thermography for temperature measurement and non-destructive testing," *Sensors*, vol. 14, no. 7, pp. 12 305–12 348, 2014.

[79] NIPPONAVIONICS, "What is infra red thermography," online; accessed 30th October, 2017. [Online]. Available: www.infrared.avio.com

[80] H. Krauss, C. Eschey, and M. Zaeh, "Thermography for monitoring the selective laser melting process," in *Proceedings of the Solid Freeform Fabrication Symposium*, 2012.

[81] H. Krauss, T. Zeugner, and M. F. Zaeh, "Layerwise monitoring of the selective laser melting process by thermography," *Physics Procedia*, vol. 56, pp. 64–71, 2014.

[82] R. B. Dinwiddie, V. Kunc, J. M. Lindal, B. Post, R. J. Smith, L. Love, and C. E. Duty, "Infrared imaging of the polymer 3d-printing process," *SPIE Sensing Technology+ Applications*, pp. 910 502–910 502, 2014.

[83] J. Raplee, A. Plotkowski, M. M. Kirka, R. Dinwiddie, A. Okello, R. R. Dehoff, and S. S. Babu, "Thermographic microstructure monitoring in electron beam additive manufacturing," *Scientific Reports*, vol. 7, p. 43554, 2017.

[84] M. Baumers, C. Tuck, R. Wildman, I. Ashcroft, and R. Hague, "Energy inputs to additive manufacturing: does capacity utilization matter?" *EOS*, vol. 1000, no. 270, pp. 30–40, 2011.

[85] K. Salonitis, "Energy efficiency of metallic powder bed additive manufacturing processes," in *Handbook of Sustainability in Additive Manufacturing*. Springer, 2016, pp. 1–29.

[86] S. W. Williams, F. Martina, A. C. Addison, J. Ding, G. Pardal, and P. Colegrove, "Wire+ arc additive manufacturing," *Materials Science and Technology*, vol. 32, no. 7, pp. 641–647, 2016.

[87] C. E. Scheck, J. N. Wolk, W. E. Frazier, B. T. Mahoney, K. Morris, R. Kestler, and A. Bagchi, "Naval additive manufacturing: Improving rapid response to the warfighter," *Naval Engineers Journal*, vol. 128, no. 1, pp. 71–75, 2016.

[88] A. Panesar, I. Ashcroft, D. Brackett, R. Wildman, and R. Hague, "Design framework for multifunctional additive manufacturing: coupled optimization strategy for structures with embedded functional systems," *Additive Manufacturing*, pp. 98–105, 2017.

[89] S. Ford and M. Despeisse, "Additive manufacturing and sustainability: an exploratory study of the advantages and challenges," *Journal of Cleaner Production*, vol. 137, pp. 1573–1587, 2016.